

# ABSTRACT

PICKLES, AUSTIN JOSIAH. Electromagnetic Energy Localization and Characterization of Composites. (Under the direction of Dr. Michael Steer.)

This dissertation examines the electromagnetic (EM) properties of two component composites. These composites exhibit varying degrees of complexity, ranging from those containing single cube inclusions to those consisting of hundreds of irregularly shaped inclusions in a disordered arrangement. Specifically, time-domain EM modeling is used as a tool to calculate effective permittivity as well as EM localization behavior for these mixtures.

For single inclusion mixtures with high permittivity contrast between the inclusion and the surrounding matrix material, strong deviation from established mixing theories is found. It is also shown that the orientation of the inclusion impacts the effective electrical permittivity of the composite. Electric fields are found to localize on the edges and corners of an irregular inclusion independent of simulation boundary conditions.

Increasing the complexity of the studied mixtures, the EM properties are then analyzed for mixtures containing many irregularly- and regularly-shaped inclusion crystals. A strong correlation between effective permittivity and cross-sectional area is found for these mixtures. With hundreds of inclusion crystals (with either irregular or cube shapes), the change in inclusion shape causes negligible differences in effective permittivity.

Electric energy density localizes on edges and corners of inclusions regardless of inclusion shape. A result not highlighted by single inclusion mixtures, for composites containing numerous inclusions significant increases in energy localization are observed as the EM signal travels through more inclusions. This increase in hotspot magnitude is observed for complex mixtures with hundreds of disordered irregularly shaped inclusion

| Report Documentation Page  |                                | Form Approved<br>OMB No. 0704-0188                    |
|--|--------------------------------|---|
| Public reporting burden for the collection of information is estimated to average 1 hour per response, including the time for reviewing instructions, searching existing data sources, gathering and maintaining the data needed, and completing and reviewing the collection of information. Send comments regarding this burden estimate or any other aspect of this collection of information, including suggestions for reducing this burden, to Washington Headquarters Services, Directorate for Information Operations and Reports, 1215 Jefferson Davis Highway, Suite 1204, Arlington VA 22202-4302. Respondents should be aware that notwithstanding any other provision of law, no person shall be subject to a penalty for failing to comply with a collection of information if it does not display a currently valid OMB control number. |                                |   |
| 1. REPORT DATE<br><b>01 NOV 2013</b>   | 2. REPORT TYPE<br><b>Final</b> | 3. DATES COVERED<br><b>1 Aug 2010 - 31 Dec 2016</b>   |
| 4. TITLE AND SUBTITLE<br><b>Electromagnetic Energy Localization and Characterization of Composites / PhD Dissertation</b>  |                                | 5a. CONTRACT NUMBER<br><b>N/A</b>                     |
|  |                                | 5b. GRANT NUMBER<br><b>N00014-10-1-0958</b>           |
|  |                                | 5c. PROGRAM ELEMENT NUMBER<br><b>N/A</b>              |
| 6. AUTHOR(S)<br><b>Austin J. Pickles Electrical &amp; Computer Engineering North Carolina State University</b>   |                                | 5d. PROJECT NUMBER<br><b>N/A</b>                      |
|  |                                | 5e. TASK NUMBER<br><b>N/A</b>                         |
|  |                                | 5f. WORK UNIT NUMBER<br><b>N/A</b>                    |
| 7. PERFORMING ORGANIZATION NAME(S) AND ADDRESS(ES)<br><b>North Carolina State University Electrical &amp; Computer Engineering 890 Oval Dr., 3114 Engineering Building II Raleigh, NC 27695</b>  |                                | 8. PERFORMING ORGANIZATION REPORT NUMBER<br><b>60</b> |
| 9. SPONSORING/MONITORING AGENCY NAME(S) AND ADDRESS(ES)<br><b>Office of Naval Research (ONR) 875 North Randolph Street - Suite 1425 Code 03R Arlington, VA 22203-1995</b>  |                                | 10. SPONSOR/MONITOR'S ACRONYM(S)<br><b>ONR</b>        |
|  |                                | 11. SPONSOR/MONITOR'S REPORT NUMBER(S)<br><b>N/A</b>  |
| 12. DISTRIBUTION/AVAILABILITY STATEMENT<br><b>Approved for public release, distribution unlimited</b>  |                                |   |
| 13. SUPPLEMENTARY NOTES<br><b>N/A, The original document contains color images.</b>  |                                |   |

## 14. ABSTRACT

This dissertation examines the electromagnetic (EM) properties of two component composites. These composites exhibit varying degrees of complexity, ranging from those containing single cube inclusions to those consisting of hundreds of irregularly shaped inclusions in a disordered arrangement. Specifically, time-domain EM modeling is used as a tool to calculate effective permittivity as well as EM localization behavior for these mixtures. For single inclusion mixtures with high permittivity contrast between the inclusion and the surrounding matrix material, strong deviation from established mixing theories is found. It is also shown that the orientation of the inclusion impacts the effective electrical permittivity of the composite. Electric fields are found to localize on the edges and corners of an irregular inclusion independent of simulation boundary conditions. Increasing the complexity of the studied mixtures, the EM properties are then analyzed for mixtures containing many irregularly- and regularly-shaped inclusion crystals. A strong correlation between effective permittivity and cross-sectional area is found for these mixtures. With hundreds of inclusion crystals (with either irregular or cube shapes), the change in inclusion shape causes negligible differences in effective permittivity. Electric energy density localizes on edges and corners of inclusions regardless of inclusion shape. A result not highlighted by single inclusion mixtures, for composites containing numerous inclusions significant increases in energy localization are observed as the EM signal travels through more inclusions. This increase in hotspot magnitude is observed for complex mixtures with hundreds of disordered irregularly shaped inclusion crystals. The same behavior is also observed for the much simpler scenario of a few dozen cube inclusions distributed within discrete parallel planes. As a result, a key conclusion from this work is that the study of hotspots does not require the use of geometrically complex structures with hundreds of irregular inclusions. Rather, much simpler arrangements of fewer and regularly shaped inclusions can be analyzed since they exhibit similar energy localization behavior.

## 15. SUBJECT TERMS

## 16. SECURITY CLASSIFICATION OF:

a. REPORT

**unclassified**

b. ABSTRACT

**unclassified**

c. THIS PAGE

**unclassified**17. LIMITATION  
OF ABSTRACT**SAR**18. NUMBER  
OF PAGES**147**19a. NAME OF  
RESPONSIBLE PERSON

crystals. The same behavior is also observed for the much simpler scenario of a few dozen cube inclusions distributed within discrete parallel planes. As a result, a key conclusion from this work is that the study of hotspots does not require the use of geometrically complex structures with hundreds of irregular inclusions. Rather, much simpler arrangements of fewer and regularly shaped inclusions can be analyzed since they exhibit similar energy localization behavior.

© Copyright 2013 by Austin Josiah Pickles

All Rights Reserved

Electromagnetic Energy Localization and Characterization of Composites

by  
Austin Josiah Pickles

A dissertation submitted to the Graduate Faculty of  
North Carolina State University  
in partial fulfillment of the  
requirements for the Degree of  
Doctor of Philosophy

Electrical Engineering

Raleigh, North Carolina

2013

APPROVED BY:

---

Dr. Mohammed Zikry

---

Dr. John Muth

---

Dr. Dror Baron

---

Dr. Michael Steer  
Chair of Advisory Committee

## DEDICATION

To my parents, Mark and Bernadette, and my brother, Joshua.

## **BIOGRAPHY**

Austin Josiah Pickles grew up in North Carolina and received his B.S. in Electrical Engineering in 2008 and his M.S. in Electrical Engineering in 2009, both from North Carolina State University. Since 2010 he has been working towards the Ph.D. degree in Electrical Engineering. While in graduate school he has worked as a Teaching Assistant and since 2011 as a Research Assistant under the direction of Dr. Michael Steer.



## ACKNOWLEDGEMENTS

I would first like to thank my advisor, Dr. Michael Steer, for all of your advice and ideas that guided me through my dissertation. Thank you to Dr. Mohammed Zikry, Dr. John Muth, and Dr. Dror Baron for your inputs as members of my committee and to Elaine Hardin, Siobhan Strange, Katy Wilson, and Tim Atkinson for all of your help. Thanks to the U.S. Office of Naval Research for providing the funding for my research. To Dr. Vrinda Haridasan, Dr. Josh Wetherington, Spencer Johnson, Matt Purvis, Nehal Parikh, Michael Chen, Drew LaBarbera, and Judith Brown, thank you for your advice and our discussions. And to Ian Kilgore, thank you for assisting me with my research.

Thank you to all of the teachers I have had throughout the years. It is through a culmination of your efforts that I have completed this dissertation, and for that I am very grateful.

Thank you to my parents, Mark and Bernadette, my brother, Joshua, and all of my family and friends for all of your support and encouragement throughout the years. It means so much to me. Thank you for believing in me.

# TABLE OF CONTENTS

|  |             |
|--|-------------|
| <b>LIST OF FIGURES</b>   | <b>viii</b> |
| <b>Chapter 1 Introduction</b>  | <b>1</b>    |
| 1.1 Overview   | 1           |
| 1.2 Motivations  | 2           |
| 1.2.1 Explosive Materials  | 2           |
| 1.2.2 Broader Impact   | 4           |
| 1.2.3 Technical Approach   | 4           |
| 1.3 Original Contributions   | 5           |
| 1.4 Outline of Dissertation  | 6           |
| 1.5 Published Works  | 7           |
| 1.5.1 Journal Papers   | 7           |
| <b>Chapter 2 Literature Review</b>   | <b>8</b>    |
| 2.1 Introduction   | 8           |
| 2.2 Permittivity   | 8           |
| 2.2.1 Introduction   | 8           |
| 2.2.2 Electric Field, Dielectrics, and Permittivity  | 9           |
| 2.3 Effective Permittivity   | 10          |
| 2.3.1 Introduction   | 10          |
| 2.3.2 Early Work   | 11          |
| 2.3.3 Effective Medium Theories  | 12          |
| 2.3.4 Bounds on Permittivity   | 13          |
| 2.3.5 Electromagnetics Aided by Computers  | 13          |
| 2.3.6 Summary  | 13          |
| 2.4 Research on Composite Mixtures   | 14          |
| 2.4.1 Introduction   | 14          |
| 2.4.2 Effective Permittivity Research  | 14          |
| 2.4.3 Energy Localization Research   | 16          |
| 2.4.4 Summary  | 17          |
| 2.5 Summary  | 18          |
| <b>Chapter 3 Electromagnetic Properties of Mixtures with Single and Regularly Ordered Inclusions</b> | <b>19</b>   |
| 3.1 Introduction   | 19          |
| 3.2 Three-Dimensional Mixing Rules   | 22          |
| 3.3 Simulation Method and Technique  | 23          |
| 3.4 Modeling of Irregular Crystals   | 25          |

|   |  |            |
|---|--|------------|
| 3.4.1   | Modeling of Irregular Crystals in CST . . . . .                    | 26         |
| 3.4.2   | Energy Localization . . . . .                                      | 29         |
| 3.4.3   | Effective Permittivity with HMX Inclusions . . . . .               | 36         |
| 3.4.4   | Effective Permittivity with High Permittivity Inclusions . . . . . | 39         |
| 3.4.5   | Summary . . . . .  | 39         |
| 3.5   | Modeling of Multiple Crystals . . . . .                            | 41         |
| 3.6   | Rotated Crystals . . . . .   | 43         |
| 3.6.1   | Cube-shaped Rotated High Permittivity Inclusions . . . . .         | 44         |
| 3.6.2   | Irregular Rotated High Permittivity Inclusions . . . . .           | 49         |
| 3.6.3   | Impact of Operating Frequency . . . . .                            | 57         |
| 3.7   | Summary . . . . .  | 59         |
| <b>Chapter 4 Electromagnetic Properties of Mixtures with Many Disordered Inclusions . . . . .</b> |  | <b>62</b>  |
| 4.1   | Introduction . . . . .   | 62         |
| 4.2   | Classical Mixing Rules . . . . .                                   | 65         |
| 4.3   | Method of Simulation . . . . .                                     | 66         |
| 4.4   | Automated Creation of Complex Composites . . . . .                 | 68         |
| 4.4.1   | Creating Multiple Irregular Crystal Structures . . . . .           | 69         |
| 4.4.2   | Localization of Electromagnetic Energy . . . . .                   | 75         |
| 4.5   | Multiple Crystal Mixtures . . . . .                                | 78         |
| 4.5.1   | Crystal Structures in CST Microwave Studio . . . . .               | 78         |
| 4.5.2   | Low Permittivity Inclusions . . . . .                              | 81         |
| 4.5.3   | High Permittivity Inclusions . . . . .                             | 83         |
| 4.6   | Overall Inclusion Structure and Permittivity . . . . .             | 84         |
| 4.6.1   | High Permittivity Inclusions . . . . .                             | 84         |
| 4.6.2   | Relationship to Cross-Sectional Area . . . . .                     | 86         |
| 4.7   | Energy Localization . . . . .                                      | 92         |
| 4.7.1   | High Permittivity Inclusions . . . . .                             | 92         |
| 4.7.2   | Electric Fields for Irregular Inclusions . . . . .                 | 96         |
| 4.7.3   | Behavior for Cube-shaped Inclusions . . . . .                      | 100        |
| 4.8   | Summary . . . . .  | 106        |
| <b>Chapter 5 Summary and Future Work . . . . .</b>  |  | <b>108</b> |
| 5.1   | Summary of Research . . . . .                                      | 108        |
| 5.2   | Future Work . . . . .  | 114        |
| <b>REFERENCES . . . . .</b>   |  | <b>116</b> |
| <b>APPENDIX . . . . .</b>   |  | <b>121</b> |
| Appendix A MATLAB Code . . . . .  |  | 122        |

|     |   |     |
|-----|---|-----|
| A.1 | Code to Calculate Effective Permittivity . . . . .                | 122 |
| A.2 | Code to Plot Effective Permittivity and Mixing Theories . . . . . | 131 |

## LIST OF FIGURES

|            |  |    |
|------------|--|----|
| Figure 2.1 | Axis definitions for a TEM wave. . . . .   | 15 |
| Figure 3.1 | An irregularly-shaped inclusion inside an outer box. The inclusion volume fraction here is 20%. The crystal is within a cube with a side length of 0.26 mm. For comparison, with $\epsilon_r = 28$ , the wavelength at 50 GHz is 1.13 mm. . . . .  | 27 |
| Figure 3.2 | The irregular crystal of Figure 3.1 shown with waveguide ports (Port 1 and Port 2) set along the propagation axis, the $z$ axis. In turn the $x$ and $y$ propagation directions were also considered with the crystal structure fixed in position and boundary conditions changed appropriately. . . . .   | 28 |
| Figure 3.3 | Cross section of the larger emulated structure based on a unit cell shown in Figure 3.1. The electric and magnetic boundary conditions of the TEM environment create electric and magnetic mirror boundaries, extended here for the 25 inner most cells. . . . .   | 30 |
| Figure 3.4 | Gaussian pulse excitation signal used in simulation. . . . .   | 31 |
| Figure 3.5 | Peak electric energy density at $t = 40$ ps for the HMX-based composite (calculated as J/m <sup>3</sup> and here normalized to a maximum of 1) with highest density at the edges and corners indicated by the black oval. Calculated using the TEM environment with the applied electric field polarized in the $x$ direction and propagating in the positive $z$ direction. . . . . | 32 |
| Figure 3.6 | Peak electric energy density for the zirconia-like high permittivity inclusion normalized to the energy density in Figure 3.5. Conditions correspond to those in Figure 3.5. . . . .   | 33 |
| Figure 3.7 | Normalized peak electric energy density for the HMX (low permittivity) inclusion with highest density at the edges and corners indicated by the black oval. Plane wave excitation and periodic boundaries are utilized. The electric field is polarized in the $x$ direction with propagation in the positive $z$ direction. . . . .   | 34 |
| Figure 3.8 | Electric energy density for the high permittivity inclusion normalized to the energy density in Figure 3.7 with the same simulation conditions as in Figure 3.7. . . . .   | 35 |

|             |  |    |
|-------------|--|----|
| Figure 3.9  | Plots of the real component of the effective relative permittivity versus volume fraction, i.e. filling factor $q$ , for a compound with irregular HMX crystal inclusions. The squares identify the effective permittivities calculated (using EM simulated results) as the equally weighted average of the effective permittivities extracted for each of the three positive orthogonal propagation directions. The plus signs identify the effective permittivities calculated similarly but now considering both positive and negative propagation directions. Also shown are the effective permittivities calculated using the Maxwell Garnett and Bruggeman mixing theories. . . . .        | 37 |
| Figure 3.10 | Plots of the real component of the effective relative permittivity (derived from EM simulation results) versus filling factor for an irregular high permittivity inclusion crystal. The squares indicate the equally weighted average of the effective permittivities calculated for each of the three positive orthogonal propagation directions. The plus signs indicate the equally weighted average effective permittivities of the positive and negative propagation directions (6 total). The circles indicate the results from using the Frequency Domain Solver. Also shown are the effective permittivities calculated using the Maxwell Garnett and Bruggeman mixing theories. . . . . | 40 |
| Figure 3.11 | A total of 729 cube crystals (inclusions) arranged on a grid within a free space outer block. The volume fraction of inclusions here is 5%. . . . .  | 42 |
| Figure 3.12 | Plots of real effective relative permittivity, $\Re(\epsilon_{\text{eff}})$ , versus various filling factors for high permittivity cube inclusion crystals on a grid along with various bounds. . . . .  | 43 |
| Figure 3.13 | Cube-shaped high permittivity inclusion crystal at 10% volume fraction in the TEM simulation environment. . . . .  | 45 |
| Figure 3.14 | The real effective relative permittivity, $\Re(\epsilon_{\text{eff}})$ , of a high permittivity cube-shaped inclusion at a filling factor of 0.10 versus rotation angle around the $x$ , $y$ , and $z$ axes. Here, the electric field is polarized in the $x$ direction. . . . .   | 46 |
| Figure 3.15 | Cross-sectional area fraction from the perspective of the $x$ axis for a 10% filling factor. For other filling factors the curves are directly scaled. . . . .   | 47 |
| Figure 3.16 | The real effective relative permittivity, $\Re(\epsilon_{\text{eff}})$ , of a high permittivity cube-shaped inclusion at 20% volume fraction versus rotation angles around the $x$ , $y$ , and $z$ axes. The electric field is polarized in the $x$ direction. . . . .   | 48 |

|             |   |    |
|-------------|---|----|
| Figure 3.17 | The real effective relative permittivity, $\Re(\epsilon_{\text{eff}})$ , of a high permittivity irregular-shaped inclusion at 20% filling factor versus rotation angle around the $x$ , $y$ , and $z$ axes. The electric field is polarized in the $x$ direction. . . . . | 50 |
| Figure 3.18 | Cross-sectional area fraction of the rotated irregular crystal from the perspective of the $x$ axis (electric field polarization axis) as the crystal is rotated around a given axis. . . . .   | 51 |
| Figure 3.19 | The real effective relative permittivity, $\Re(\epsilon_{\text{eff}})$ , of a high permittivity irregular-shaped inclusion at 20% filling factor versus rotation angle around the $x$ , $y$ , and $z$ axes. The electric field is polarized in the $y$ direction. . . . . | 52 |
| Figure 3.20 | Cross-sectional area fraction of the rotated irregular crystal from the perspective of the $y$ axis (electric field polarization axis) as the crystal is rotated around a given axis. . . . .   | 53 |
| Figure 3.21 | The real effective relative permittivity, $\Re(\epsilon_{\text{eff}})$ , of a high permittivity irregular-shaped inclusion at 20% filling factor versus rotation angle around the $x$ , $y$ , and $z$ axes. The electric field is polarized in the $z$ direction. . . . . | 55 |
| Figure 3.22 | Cross-sectional area fraction of the rotated irregular crystal from the perspective of the $z$ axis (electric field polarization axis) as the crystal is rotated around a given axis. . . . .   | 56 |
| Figure 3.23 | The real effective relative permittivity, $\Re(\epsilon_{\text{eff}})$ , of the high permittivity irregular-shaped inclusion at 20% volume fraction (results for all rotation angles given in Figure 3.21) for $0^\circ$ rotation as a function of frequency. . . . .     | 58 |
| Figure 4.1  | An example of two different irregularly shaped inclusion crystals, one with 8 sides (left) and one with 7 sides (right) as created using the Bullet physics library. . . . .  | 70 |
| Figure 4.2  | Unique structure created with 550 irregular crystals inside an outer box (with 19.5% of the outer box volume containing crystals) as created using the Bullet physics library. . . . .  | 71 |
| Figure 4.3  | Unique structure created with 500 irregular crystals inside an outer box (with 21.4% of the outer box volume containing crystals) as created using the Bullet physics library. . . . .  | 72 |
| Figure 4.4  | The same mixture shown in Figure 4.2 along with waveguide excitation ports after it has been imported into CST Microwave Studio for EM simulation. . . . .  | 73 |
| Figure 4.5  | The same mixture from Figure 4.3 with waveguide excitation ports after it has been imported into CST Microwave Studio for EM simulation. . . . .  | 74 |

|             |   |    |
|-------------|---|----|
| Figure 4.6  | Mixture from Figure 4.4 showing high energy density on crystal corners and edges. . . . .   | 76 |
| Figure 4.7  | Mixture from Figure 4.5 showing high energy density on corners and edges for a different irregular mixture. . . . .   | 77 |
| Figure 4.8  | A total of 978 irregularly shaped inclusion crystals inside of a block (with side length of 1.37 mm) in a TEM simulation environment. The volume fraction of the inclusions is 27.5%. . . . .   | 79 |
| Figure 4.9  | A total of 1,144 disordered cube inclusion crystals (each with side length of 0.085 mm) inside of a vacuum outer block (with side length of 1.37 mm). The volume fraction of inclusions is 27.5%. . . . .   | 80 |
| Figure 4.10 | Plots of real effective relative permittivity, $\Re(\epsilon_{\text{eff}})$ , versus various filling factors for low permittivity irregular and cube inclusion crystals along with various mixing theories. . . . .   | 82 |
| Figure 4.11 | Plots of real effective relative permittivity, $\Re(\epsilon_{\text{eff}})$ , as a function of filling factor for high permittivity irregular and cube inclusion crystals along with various mixing theories. . . . .   | 83 |
| Figure 4.12 | Structure showing a high permittivity inclusion arranged as a plate in vacuum with 11.0% volume fraction. . . . .   | 85 |
| Figure 4.13 | Structure showing 894 high permittivity irregular inclusions inside a vacuum outer block (with side length 1.46 mm). The volume fraction of inclusions is 15%. . . . .  | 88 |
| Figure 4.14 | Structure showing 624 high permittivity cube inclusions (each with side length 0.085 mm) inside a vacuum outer block (with side length 1.37 mm). The volume fraction of inclusions is 15%. . . . .  | 89 |
| Figure 4.15 | Real effective permittivity, $\Re(\epsilon_{\text{eff}})$ , plotted as a function of cross-sectional area fraction, $A_w$ . The volume fraction of inclusions is 15%. The letters near the data points indicate the electric field polarization axis for each type of crystal as well as the cross-sectional area fraction direction. . . . . | 90 |
| Figure 4.16 | Near-maximum electric energy density showing localization at inclusion corners and edges, with highest localization in the bottom two circles. The electric field is polarized along the $x$ axis and the propagation direction is positive $z$ (down). The volume fraction is 32.5%. . . . .   | 93 |
| Figure 4.17 | Electric energy density with the same conditions as in Figure 4.16, but with propagation in the reverse direction (up). The strong localization from Figure 4.16 is not seen in the bottom two circles. Instead, there is higher localization in the top circle. . . . .  | 94 |



|             |   |     |
|-------------|---|-----|
| Figure 4.18 | Comparison of the electric field at the crystal corner indicated by the bottom right circle in Figure 4.16 and Figure 4.17 with propagation direction. At 48.1 ps there is a significant difference in the electric field and electric energy density depending on propagation direction. Higher peak localization is seen with the positive propagation direction (down) when the EM signal has traveled through more of the irregular surrounding material. . . . . | 97  |
| Figure 4.19 | Comparison of the electric field at the crystal corner indicated by the bottom left circle in Figure 4.16 and Figure 4.17 with propagation direction. Higher peak localization is seen at 48.1 ps with the positive propagation direction (down) when the EM signal has traveled through more of the irregular surrounding material. . . .  | 98  |
| Figure 4.20 | Comparison of electric field for the top circle in Figure 4.16 and Figure 4.17 with propagation direction. At 48.1 ps there is a significant difference in the electric field and electric energy density depending on propagation direction. Higher peak localization is seen with the negative propagation direction (up) when the EM signal has traveled through more of the irregular surrounding material. . . .   | 99  |
| Figure 4.21 | Cube-shaped inclusions arranged in two planes. On the right are the isolated cubes and on the left are the back cubes. . . . .  | 100 |
| Figure 4.22 | Layers of cube-shaped inclusions are added between the layers in Figure 4.21 with an increasing number of inclusions in each layer.   | 101 |
| Figure 4.23 | The structure in Figure 4.22 (surrounded by vacuum) along with waveguide ports for simulation. . . . .  | 102 |
| Figure 4.24 | Near-peak electric energy density for the back layer of cubes at 44 ps (time of near-maximum energy density) with highest magnitude at the edges and corners of the back cubes as indicated by the black circle. This occurs for Port 1 excitation. . . . .   | 103 |
| Figure 4.25 | Electric field magnitudes for four different locations in the structure in Figure 4.23 as a function of time. Peak localization magnitude is reached for the back cubes with Port 1 excitation after the signal has traveled through other scatterers. . . . .  | 104 |

# Chapter 1

## Introduction

### 1.1 Overview

Studies of the analysis and detection of energetic materials [1]–[5] are of substantial importance. To aid in this research, it is important to be able to model and analyze component mixtures. To understand the EM characteristics of such materials, it is necessary to understand the coupling of EM energy into random mediums with specific structures including energetic or explosive materials and organic compounds. Analysis of the concentration of EM energy is significant because such a concentration could result in increased vapor pressure from organic composites, making it easier to detect these materials.

Specifically, it takes relatively little energy to release energy in metastable bonds in a material. If a hotspot is introduced into an energetic material it can heat up. The following research seeks to further understand the behavior of such localization, as well as general EM properties of component mixtures.

## 1.2 Motivations

An important goal of this research is to further explore the coupling of EM energy into disordered and random mediums. To aid in this understanding the objectives of this research are to understand if these hotspots occur at certain locations and what conditions lead to increased hotspot magnitudes. Realistic crystalline composites can contain crystals with various sizes, and these crystals can be both regular and irregular in shape. So, another objective of this research is to determine how the shape and distribution of crystals affects how energy is stored within a mixture. The next section discusses an important type of mixture that is especially relevant today, namely explosive or energetic materials.

### 1.2.1 Explosive Materials

In general terms, a chemical explosive can be defined as “a compound or a mixture of compounds which, when subjected to heat, impact, friction, or shock, undergoes very rapid, self-propagating, heat-producing decomposition” [6]. EM radiation incident on an explosive or energetic material can cause a release of energy that has the potential to be damaging to a target [6]. Energy can be defined as either potential, which measures the ability of doing work, or kinetic, which is the energy of motion [6]. Explosives such as trinitrotoluene (TNT) have chemical bonds that are relatively unstable [6]. So, chemical potential energy exists that can be turned into kinetic energy under the right conditions [6]. The detonation of the explosive brings stability to the chemical bonds, leading to kinetic energy achieved through blast and thermal energy release [6]. Since overall there is a production of energy, the process of changing the bonds of a chemical system to a greater amount of stability is an exothermal process [6].

High explosives (HEs) will detonate, which occurs when the reaction is moving through the explosive faster than the speed of sound in the explosive that has not reacted [6]. Low-order explosives (LEs) will deflagrate or rapidly burn with a reaction that is slower than the speed of sound in the explosive that is unreacted [6]. Almost all commercially available explosives, not including black powder, are HEs [6].

Research Department Explosive (RDX) is a combination of a crystalline explosive and a binder, which is often a plastic material [6]. High Melt Explosive (HMX) is chemically similar to RDX [6]. RDX and HMX are part of a group of organic nitrate explosives called nitramines [7]. The study of energetic materials is an important motivation of this research. HMX is of widespread importance, being the “highest-energy solid explosive produced on a large scale in the United States” [7]. In addition, the Navy uses HMX as a plastic-bonded explosive ingredient [7].

Improvised Explosive Devices (IEDs) are of significant concern in places such as Iraq [8]. IEDs in Iraq can be initiated with a device such as a cell phone that triggers the IED to go off [8]. In practice there are several methods for disarming an IED including using EM pulses [8]. As a method for either disabling or destroying an IED, a high energy EM pulse can cause the trigger of an IED to “fail open” and not induce an explosion or “fail closed” and detonate the IED [8]. However, very cheap countermeasures can be used to counter attempts at destroying or disabling IEDs [8]. Clearly, additional methods are required. Since EM energy can be used to destroy or disable explosive devices, it is important to gain further understanding of how this energy behaves within random mixtures. To that end, an important motivation of this research is the need to study how energy is stored in three-dimensional random mixtures, including those mixtures containing the energetic material HMX. HMX is a type of polymer bonded explosive (PBX), which is a combination of a polymeric binder with explosive crystals [9]. The EM

properties of HMX crystals, as well as their sizes based on [9], will be used here to study realistic crystalline mixtures.

A motivation in studying combinations of variously-sized crystals is that if hotspots can be introduced into a material using EM signals, the crystal phase state in the material can be altered. This has various implications including IED destruction or disablement. The energy storage capabilities of mixtures will also be investigated with studies of effective permittivity of composites.

### **1.2.2 Broader Impact**

The research described in this dissertation also has various other applications that extend beyond energetic materials. One such application, which can be related to composites with randomly oriented and distributed inclusions, is the next generation of aerospace-qualified Carbon Fiber Reinforced Composites (CFRCs). While still at least a decade away, these composites will utilize random fibers and will not delaminate (or separate into layers), coming with a greatly reduced cost and increased reliability. This research can also be related to several other applications including the characterization of solid rocket fuel, the demolition of either visible or buried structures, remote interrogation, and demining.

### **1.2.3 Technical Approach**

In this research CST Microwave Studio [10] will provide the basis for studying three-dimensional mixtures. CST Microwave Studio is a software tool for high frequency applications that provides 3D EM simulations. It will also serve as a useful tool for studying the permittivity of composites. Specifically, the time-domain solver in CST Microwave

Studio, utilizing the finite integration technique (FIT), will be utilized. The time-domain solver allows energy distributions to be studied as a function of time.

Utilizing CST Microwave Studio, materials will be modeled with various permittivities, shapes, sizes, and orientations to show how these characteristics impact the permittivities and energy storage behavior of composite mixtures. The crystals that are part of these mixtures will be given material properties of realistic materials including HMX.

## 1.3 Original Contributions

The original contributions of this dissertation are summarized here.

1. Two-component composites are studied involving both regularly- and irregularly-shaped inclusions. The orientation of inclusions is shown to affect the effective electrical permittivity of mixtures. This is presented in Chapter 3.
2. Structures are analyzed involving many scaled and rotated inclusion crystals with both regular and irregular shapes. These complex structures are simulated in CST Microwave Studio with EM analysis of energy localization behavior and effective permittivity. This is presented in Chapter 4.
3. The effective permittivity of composite mixtures is found to be highly correlated to the cross-sectional area of the inclusion crystals within the mixture. This is presented in Sections 3.6 and 4.6.
4. Effective permittivity is compared between mixtures involving many regularly- and irregularly-shaped inclusions. With hundreds of inclusions the effective permittivity is found to be independent of inclusion shape. This is presented in Section 4.5.

5. Both disordered and more organized arrangements of inclusions show EM localization on inclusion edges and corners. This is presented in Section 4.7.
6. Increased hotspot magnitude is found in composites containing many inclusions as the EM signal travels through more inclusions (a result not highlighted by single inclusion mixtures). This is presented in Section 4.7.

## 1.4 Outline of Dissertation

Chapter 2 of this dissertation provides a literature review of topics related to effective permittivity and localization of EM energy.

Chapter 3 studies two-component composites with regularly- and irregularly-shaped inclusion crystals. This chapter focuses on the relatively simpler scenarios of a single irregular inclusion and cube-shaped inclusions placed on an ordered grid. With high permittivity contrast between inclusion and matrix material, it is shown that the orientation of the inclusion affects the effective relative permittivity of the mixture. Fields are found to localize at edges and corners of the irregular inclusion independent of the simulation boundary conditions.

Chapter 4 investigates the EM properties of complex mixtures involving many crystals of regular and irregular shapes. The Bullet physics library [11], a physics engine commonly used for computer games, is used to create randomized combinations of many crystals. This automated procedure leads to a higher packing of crystals than can be obtained reasonably with manual creation. With high permittivity contrast between inclusions and matrix material, effective permittivity is found to deviate from established mixing theories. With hundreds of irregular or cube inclusion crystals within a mixture, the impact of individual inclusion shape averages out. Surrounding inclusions are found to

impact the electric energy localization within the mixtures, with higher localization seen after the EM signal has traveled through more inclusion crystals.

Chapter 5 provides a summary of the research presented and suggests areas for future study.

## 1.5 Published Works

The work outlined in this dissertation led to the following journal papers.

### 1.5.1 Journal Papers

1. © 2013 IEEE. Reprinted, with permission, from A. J. Pickles and M. B. Steer, “Effective permittivity of 3-D periodic composites with regular and irregular inclusions,” *IEEE Access*, vol. 1, pp. 523–536, 2013.
2. © 2013 IEEE. Reprinted, with permission, from A. J. Pickles, I. M. Kilgore, and M. B. Steer, “Automated creation of complex three-dimensional composite mixtures for use in electromagnetic simulation,” *IEEE Access*, vol. 1, pp. 248–251, 2013.
3. © 2013 IEEE. Reprinted, with permission, from A. J. Pickles, I. M. Kilgore, and M. B. Steer, “Electromagnetic properties of disordered three-dimensional mixtures,” *IEEE Access*, submitted for publication, September 2013.



# Chapter 2

## Literature Review

### 2.1 Introduction

The main topics explored in the following chapters are effective permittivity and EM energy localization. This chapter begins by introducing the concepts of permittivity and effective permittivity. An overview is provided of the study of effective permittivity over the past few centuries, culminating with the sophisticated computer software used today for studying effective permittivity. Finally, this chapter presents an overview of research related to studies of effective permittivity and energy localization.

### 2.2 Permittivity

#### 2.2.1 Introduction

First, this section defines the concept of permittivity as referenced in this dissertation, beginning with an overview of the related topics of electric fields and dielectrics.

### 2.2.2 Electric Field, Dielectrics, and Permittivity

If a point charge,  $Q$ , exists and experiences a force,  $F$ , due to additional charges, the electric field,  $E$ , is defined as [12]

$$E = \frac{F}{Q}. \quad (2.1)$$

From Equation 2.1, the electric field direction and the direction of the force exerted by the field on a positively charged particle are the same [12]. The attraction of opposite charges and the repulsion of like charges means the electric field points from positive charges and to negative charges [12].

When an electric field is applied to a group of materials known as dielectrics [13], which are insulators, the dielectric can be polarized. Dielectric polarization occurs when charges shift from their original positions due to the applied electric field [13]. There is not a flow of charges like in a conductor, but rather the dielectric polarization causes positive charges to move towards the field and negative charges to move away from the field [13]. This newly formed separation of charges in the dielectric creates an internal electric field that points in the opposite direction to the applied electric field, thus reducing the overall field in the dielectric [13]. A dielectric material has energy storing capacity through polarization, such as the material between a capacitor's metallic plates [13]. The surface charge of the capacitor is increased when an electric field is applied because the dielectric becomes polarized [13].

The term “insulator” generally is implied to have a low amount of electrical conduction, while “dielectrics” have a high amount of polarizability, measured by the dielectric constant [13]. The dielectric constant, or static relative permittivity, is the relative permittivity exhibited by a material when at zero frequency [14]. However, dielectric constant could refer to the static or frequency-dependent relative permittivity based on context

[14].

Permittivity,  $\epsilon$ , is a measure of a material's ability to "permit" an electric field [15]. The permittivity in vacuum is  $\epsilon_0$  [14]. The relative permittivity,  $\epsilon_r$ , as a function of angular frequency,  $\omega$ , is defined as [14]

$$\epsilon_r(\omega) = \frac{\epsilon(\omega)}{\epsilon_0}. \quad (2.2)$$

From Equation 2.2, the relative permittivity of a material is a ratio of how much electric energy is stored in the material when a voltage is applied,  $\epsilon(\omega)$ , relative to how much is stored in a vacuum,  $\epsilon_0$  [14]. Relative permittivity is generally complex, and the imaginary part of the permittivity causes EM attenuation inside the medium [14]. Relative permittivity for materials with loss is defined as [14]

$$\epsilon_r = \epsilon_{\text{real}} + \frac{\sigma}{j\omega\epsilon_0}. \quad (2.3)$$

In Equation 2.3,  $\epsilon_{\text{real}}$  is the real part of the relative permittivity and  $\sigma$  is the conductivity [14]. The loss tangent is defined as the ratio of the imaginary over the real part of the permittivity [16]. Having defined the concept of permittivity, the next section provides an overview of how the study of permittivity has evolved.

## 2.3 Effective Permittivity

### 2.3.1 Introduction

While permittivity is a useful parameter to describe the electric energy storage ability of individual materials, as summarized in the previous section, an additional concept is

necessary to describe the overall permittivity of a mixture that contains more than one material. This concept is described by effective permittivity. Exploration of the effective permittivity of a composite medium is a major focus of the research presented in the following chapters of this dissertation.

This section provides an overview of how the study of effective permittivity has evolved over the past few centuries, as discussed in detail in [17] and summarized here. These stages include [17] the work of James Clerk Maxwell, the Maxwell Garnett mixing law, Bruggeman’s work on the effective medium, bounding methods, and finally computation of electromagnetics with the use of computers. The use of sophisticated computer software is especially relevant here since it is used for the research presented in the following chapters.

### **2.3.2 Early Work**

In the late 19<sup>th</sup> century, James Clerk Maxwell was among the first to develop formulas for the effective permittivity of heterostructures [17]. Maxwell [18] studied the variation in potential for the simple scenario of a spherical inclusion of one material inside another material [17]. Soon after, formulae were developed to describe approximately the properties of the effective medium with knowledge of the materials that made up the medium [17]. Gladstone and Dale [19] utilized an approximation formula where the permittivity of the mixture was linearly proportional to the volume taken up by and permittivity of the components [17].

Analytic approaches, called mixing laws, to determining effective permittivity rely on a volume average of individual permittivities [17]. While the volume fractions are important parameters of mixing laws, internal sizes of the inclusions are not considered

[17]. The accuracy and applicability of these laws has been questioned as they have been limited to relatively simple scenarios that are dilute and geometrically simple [17], [20]. This dissertation further studies the applicability of mixing laws by comparing the simulated results to those predicted by the famous Maxwell Garnett mixing law [21].

### 2.3.3 Effective Medium Theories

Additional understanding of the properties of mixtures came with the development of the effective medium approximation (EMA), significantly discussed by Bruggeman [22] in 1935 [17]. Overall, “EMA approaches assume that each constituent is surrounded by the same effective medium. It assumes that the local electric and magnetic fields are the same in the volume occupied by each component in the composite. The basic understanding appears to be that the fictitious replacement (effective) medium is macroscopically equivalent to the real medium in its dielectric effects. The analysis is done in the approximation of noninteracting inclusions (each inclusion is subject to the same mean field, unperturbed by the presense of other inclusions)” [17]. EMA methods are applicable at low volume fractions of inclusions with the assumptions that groupings or overlapping of inclusions do not occur [17]. Since in the effective medium the energy density is seen to be uniform throughout the entire volume, EMA methods break down at higher volume fractions of inclusions since they do not take into account the interactions among the various components of a mixture [17]. So, EMA approaches do not provide an all-encompassing complete solution for the effective permittivity of two-component mixtures [17].

In regards to frequency, effective medium theories (EMTs) are valid in the quasistatic limit, meaning that the wavelength is much larger than the linear dimensions of the individual inclusions that make up the mixture [17]. So, although the wave cannot ‘see’

the inclusions, the effective permittivity is still impacted by the inclusions [17].

### **2.3.4 Bounds on Permittivity**

Another important advance in the theory of effective permittivity came with the establishment of rigorous bounds on the effective permittivity of two-component mixtures [17]. Absolute bounds for effective permittivity were developed by Wiener [23], occurring for situations of inclusion layers perpendicular or parallel to the applied field [17].

### **2.3.5 Electromagnetics Aided by Computers**

The development of computers has advanced EM study. Known as computational electromagnetics (CE), this area connects electromagnetism with materials science and computer science [17]. Results taken from computer simulations can be used to confirm or disprove EMTs, and suggest new areas that deserve further research [17]. Numerous CE methods [17] have been used in effective permittivity investigations. These include Fourier expansion [24], [25], Finite Difference Time Domain (FDTD) [26], [27], [28], finite element (FE) [29], [30], [31], the transfer matrix method [32], and boundary-integral equations (BIE) [33], [34], [35]. In a basic sense, these methods involve a combination of Maxwell's equations with a set of boundary conditions [17]. Sophisticated computer software, such as CST Microwave Studio, can be used to gain greater understanding of the EM behavior of complex component mixtures.

### **2.3.6 Summary**

As outlined in this section, the development of mixing laws and EMAs were important milestones in the study of effective permittivity. The results of the simulated effective

permittivities in the following chapters will be compared to the Maxwell Garnett and Bruggeman theories to further explore their applicability.

## **2.4 Research on Composite Mixtures**

### **2.4.1 Introduction**

The previous section covered previous research related to mixing laws and EMAs. This section explores past and current research as it relates to the subject of effective permittivity and EM energy localization in composite mixtures.

### **2.4.2 Effective Permittivity Research**

Studies of effective permittivity have included mixtures organized in both two- and three-dimensions. Research has been performed looking at component mixtures where the inclusions have regular and symmetric shapes. Kärkkäinen, Sihvola, and Nikoskinen [36] studied two-dimensional mixtures with inclusions in the shape of discs. The authors utilized mixtures contained within a TEM (Transverse ElectroMagnetic) waveguide and the inclusions were allowed to overlap with each other [36]. They considered only one permittivity contrast between matrix and inclusion material and did not find a model that predicted the simulated results over all volume fractions [36].

For a TEM wave, the electric field, magnetic field, and direction of propagation are all orthogonal to each other. An example of the axis definitions for a TEM environment is given in Figure 2.1. In Figure 2.1, the electric field is polarized in the  $y$  direction, the magnetic field is polarized in the  $z$  direction, and propagation is in the  $x$  direction.

In another paper, Kärkkäinen, Sihvola, and Nikoskinen [37] studied three-dimensional

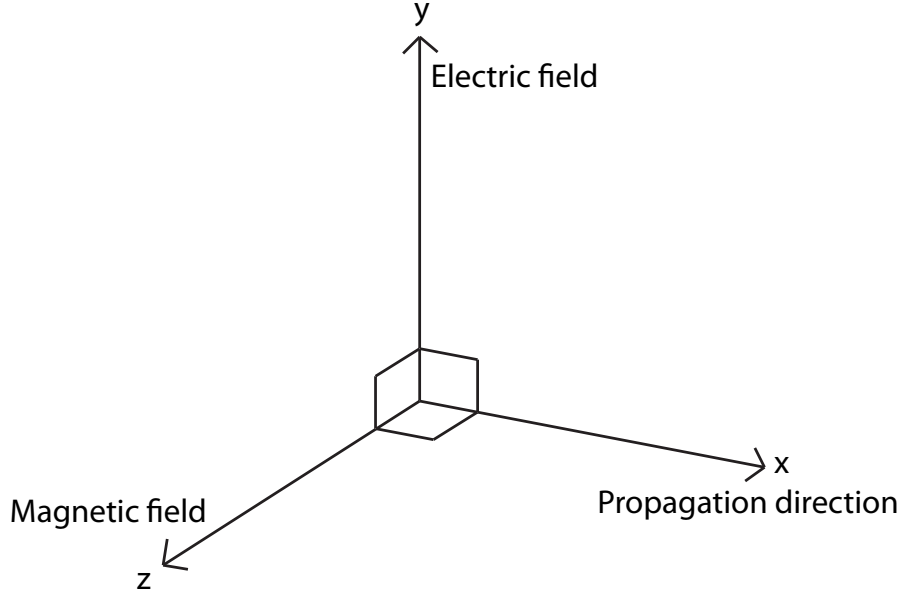


Figure 2.1: Axis definitions for a TEM wave.

mixtures of spheres and found different results for effective permittivity based on whether or not the spheres were allowed to form clusters. A mixing model was developed to fit the simulated results based on least squares fitting [37].

Wu, Chen, and Liu [38] observed differences in effective permittivity with spherical inclusions compared to inclusions shaped like a cube. Wu *et al.* [39] also studied spherical inclusions in three dimensions. The authors found good agreement with conventional mixing theories when there was low contrast between the sphere and surrounding material.

Luo, Liu, and Pan [40] analyzed three-dimensional mixtures with spherical inclusions as well as spherical inclusions with an outer membrane. The authors studied how features such as the membrane thickness had a strong impact on effective permittivity and found differences with different inclusion shapes including cubes and cylinders [40]. Wu *et al.*



[41] studied differences in effective permittivity with different spacial arrangements of spherical inclusions as well as a cylindrical inclusion.

Cheng *et al.* [42] analyzed three-dimensional mixtures where cubes of two different permittivities were organized in a random arrangement to create a larger cube-shaped mixture. Since the larger created structure was anisotropic in three dimensions, its effective permittivity was dependent on orientation [42]. Chen *et al.* [43] created a structure of cube cells, each cell with a sphere inside. The sphere was then given a randomly varying radius to represent different sized inclusions within the entire mixture [43]. Finally, Jylhä and Sihvola [44] studied three-dimensional mixtures of equal-sized spheres. The spheres were allowed to exist in random positions within the mixture [44]. The authors used a scalar fitting parameter to match their simulated results and compared the simulated effective permittivity to conventional mixing theories [44]. In [42], [43], and [44], the authors used an averaging of the effective permittivity determined in each of three orthogonal directions to obtain a single effective permittivity value.

### 2.4.3 Energy Localization Research

In addition to effective permittivity, prior research has also investigated EM field localization behavior. Mejdoubi and Brosseau analyzed regular polygon [45] and fractal shaped [45], [46] inclusions in two dimensions using FDTD modeling. Specifically studying an inclusion with a fractal shape, the authors found electric field hotspots at the inclusion corners [45]. The authors noted that these hotspots showed a lack of uniformity in field distributions that would impact effective permittivity [45]. In addition, EMA methods based on uniform field distributions (as discussed in Section 2.3.3) do not consider these hotspots and so are limited in their ability to describe the EM properties of composites

[46].

Using the FE method, Mejdoubi and Brosseau [47] analyzed electric field localization on fractal shaped inclusions. These hotspots were found on the inclusion corners and edges, showing that the fields were not uniform throughout the composite [47]. Also using the FE method, Cheng *et al.* [42] studied three-dimensional arrangements of cube inclusions. Each cube inclusion within a  $10 \times 10 \times 10$  arrangement was randomly allowed to have one of two permittivity values, creating a nonuniform structure [42]. The authors found electric field hotspots at various locations within the structure [42].

Electric field localization can be studied in either the time- or frequency-domains. In this dissertation the time-domain FIT is specifically chosen because it allows field localization behavior to be studied as a function of time. Probes can be placed within the structure at the specific locations of hotspots and the electric fields at those points can be measured throughout the simulation. The result is a record of varying field behavior in time that cannot be seen with steady-state frequency domain analyses. In this dissertation, field probes will allow localization behavior to be studied for increasingly complicated arrangements of inclusions to show how energy localizes in complex mixtures.

#### **2.4.4 Summary**

Previous researchers have analyzed effective permittivity and energy localization in composite mixtures. This research used symmetric and regularly shaped inclusions, and expanding this research to inclusions of an irregular shape is an important component of the following chapters. Realistic composites such as those containing energetic materials are often not made up of inclusions that are symmetric and uniform in shape. The differences in effective permittivity with irregularly shaped inclusions presents a scenario with more

realistic structures than those created only with spheres. In addition, the limitations of the classical mixing theories can be further understood by increasing the irregularity in inclusion shape.

## 2.5 Summary

This chapter reviewed research efforts related to effective permittivity and energy localization, which are continued with the following chapters. Effective permittivity and energy localization describe the behavior of EM energy within a medium. With an increase in the complexity of the component mixtures analyzed, the study of effective permittivity and EM localization behavior will bring a greater understanding of EM energy propagating within more complex component mixtures. The next chapter, Chapter 3, describes studies of mixtures with single irregular inclusions, and for comparison purposes, ordered cube inclusions on a grid. The complexity of the analyzed mixtures is increased in Chapter 4 with the introduction of composites containing many disordered irregular and cube inclusions.

# Chapter 3

## Electromagnetic Properties of Mixtures with Single and Regularly Ordered Inclusions

### 3.1 Introduction

This chapter explores the effective temporal surface-illuminated properties of two-component composites consisting of inclusions of regularly- and irregularly-shaped crystals in a matrix. Time-domain EM modeling using the FIT is used to calculate scattering ( $S$ -) parameters, and from these the effective relative permittivities are calculated. It is shown that the orientation of inclusions with high permittivity contrast affects the effective electrical permittivity of a composite mixture. For both low and high contrast inclusions, fields localize at edges and corners of the irregular inclusion in a manner not dependent on boundary conditions used in simulation.

The detection and neutralization of energetic materials using stand-off techniques is

of significant and growing importance [1]–[5]. Most solid energetic materials are random mixtures comprising irregularly-shaped explosive crystals embedded in a passive composite or binder. In part, the energetic material can be characterized by its steady-state bulk electrical permittivity. However, with standoff EM probing, the probe will interact with the surface and near-surface structure of the energetic material rather than the material bulk. Also the probe will be transient with the EM waveform appearing as a radio frequency (RF) pulse as the probe scans the energetic material. This chapter explores the electrical properties and energy localization of irregular materials excited by a temporal EM pulse. The electrical properties determined are compared with the standard mixing theories based on extreme mixing situations and using steady-state considerations alone. Time-domain monitors are also used to analyze the near-maximum temporal energy distributions for these irregular crystals.

Synthetic composites comprising irregularly-shaped crystals in a matrix are examined here with a view to characterizing their effective EM properties and so establish a baseline for remote detection and material characterization. In the past, studies of effective medium properties have used time- and frequency-domain EM simulation methods with various abstractions and simplifications made to render the simulation computationally tractable. The most common simplification is to consider regularly-shaped inclusions and sometimes a 2-D projected structure is analyzed. In the time domain, the effective permittivity has been calculated in 2-D for random mixtures using FDTD simulation [36] (where inclusions are disks), [45] (disks, regular polygons and fractals), and 3-D random mixtures using FDTD [38] (spheres, crosses and regular polyhedrons), and [39] (spheres and a complex yet symmetric structure). With time-domain EM analysis, regular shapes, such as cubes, spheres, and regular polygons have been studied because these enabled simplified gridding using rectangular meshing (and analytic projections onto a rectangu-

lar mesh in the case of spheres).

Frequency-domain EM analysis of 2-D random mixtures of regularly-shaped inclusions has been studied using the finite element method [47] (polygons and fractals); 3-D random mixtures of regularly-shaped inclusions using a frequency-domain finite difference method [37] (spheres), [40] (spheres, crosses, cylinders, and polyhedrons), and [41] (spheres and cylinders); and 3-D random mixtures using a frequency-domain finite element method [42] (polyhedrons), and [43], [44] (spheres). Such steady-state analyses are limited as they, for example, do not capture temporal localization of energy.

In remote probing, a region is scanned and a steady-state is not necessarily obtained as the applied signal is effectively a radio frequency (RF) pulse. The significant internal reflections of a crystal-based composite illuminated by an RF pulse result in what is referred to as a long-tail response. This characteristic is similar to that observed with RF bandpass filters where multiple internal reflections in response to an RF pulse cannot be predicted from steady-state observations [48].

A composite of two materials will typically be anisotropic due to the formation, fabrication, or manufacturing process favoring particular crystal orientations. When the crystals are much smaller than a wavelength, in which case anisotropy results from the combination of shapes, the standard characterization procedure is to determine an effective permittivity of the mixture by averaging the extracted effective permittivities of each of three orthogonal directions [42], [43], [44].

This chapter studies two materials comprising crystals in a lossless matrix. The first is an explosive material consisting of HMX crystals [9] and the other is a material with crystals having a higher relative permittivity. For the high permittivity material, both regular and irregular shapes are studied. For both materials, realistic crystal shapes (as opposed to spheres, cubes, etc.) are considered. As such, the inclusions do not necessar-

ily have symmetric shapes. Effective properties are extracted for the composites using forward and reverse propagation, and for various crystal orientations. The overall goals of this research are to determine under what situations irregularly shaped inclusions behave similarly to spheres (through comparison with the classical mixing rules based on spheres) and cubes in calculations of effective permittivity, and to analyze how rotation of the inclusion influences the effective permittivity of composites. EM modeling of mixtures with irregularly shaped inclusions is computationally intensive and knowing when simpler geometries can be used is advantageous.

## 3.2 Three-Dimensional Mixing Rules

Several conventional mixing theories exist that predict the effective properties of two-component mixtures. One of these is the Maxwell Garnett mixing theory, which provides the effective permittivity of a composite as [21]

$$\epsilon_{\text{eff}} = \epsilon_2 + 3q\epsilon_2 \frac{\epsilon_1 - \epsilon_2}{\epsilon_1 + 2\epsilon_2 - q(\epsilon_1 - \epsilon_2)}. \quad (3.1)$$

Here  $\epsilon_1$  is the permittivity of spherical inclusions,  $\epsilon_2$  is the permittivity of the surrounding material, and  $q$  is the volume fraction, i.e. filling factor, of the inclusions. The inclusion size here is much smaller than the EM wavelength. A few assumptions of the Maxwell Garnett mixing theory are that the inclusions are spherical in shape, the spheres do not touch each other, and the radius of an individual spherical inclusion is much smaller than the distances between the spheres [42]. That is, the mixing rule can only be properly used with composites that have a low proportion of inclusions whereas the crystals in energetic materials can have a volume fraction of up to 95%.

The second classical mixing theory is known as the Bruggeman rule [22]

$$(1 - q) \frac{\epsilon_2 - \epsilon_{\text{eff}}}{\epsilon_2 + 2\epsilon_{\text{eff}}} + q \frac{\epsilon_1 - \epsilon_{\text{eff}}}{\epsilon_1 + 2\epsilon_{\text{eff}}} = 0. \quad (3.2)$$

As with the Maxwell Garnett mixing theory, the Bruggeman mixing rule is derived with the assumption of widely separated spherical inclusions. More complicated structures, such as irregularly-shaped crystals, are expected to provide different results [42].

As described in [57], an important assumption of the Bruggeman rule is that there is no separation between the matrix material and the inclusions. Rather, the mixture is treated as a homogenized medium over which polarizations are evaluated. Thus the Bruggeman rule treats the inclusions and surrounding material as being symmetric. The Bruggeman rule, Equation 3.2, balances the components in relation to the effective medium, weighting each component by  $q$  for inclusions and  $1 - q$  for the surroundings. Conversely, the Maxwell Garnett theory does not utilize such symmetry.

Mixing rules developed for composites are based on the two classical mixing rules (Maxwell Garnett and Bruggeman) but none cover all types of inclusions [42]. In this chapter the applicability and limitations of the classic Maxwell Garnett and Bruggeman rules are further developed.

### 3.3 Simulation Method and Technique

The effective permittivity of a sample of finite thickness can be determined using measured or simulated scattering ( $S$ -) parameters as described in [49], [50], [51], [52]. The time-domain FIT solver with hexahedral meshing implemented in the commercial EM package CST Microwave Studio is utilized for these simulations. This package allows



complex 3D shapes to be modeled and simulated. FIT is equivalent computationally to FDTD except that the time-domain Maxwell's Equations are discretized in integral form rather than differential form [52] and gridding is generalized.

The adaptive meshing algorithm used refines the mesh until convergence of electrical characterization is obtained. Refinement of the time-domain mesh by an additional step led to an effective permittivity change of less than 0.5% (indicating that acceptable accuracy had been reached). The number of mesh cells for each time-domain simulation run was at least 250,000. Computation was performed using an 80 core cluster with 160 GB of RAM and clocking at 2.66 GHz. Where required, time results were Fourier transformed to yield a frequency-domain characterization from an applied wideband EM pulse.

With the RF component having angular frequency  $\omega$ , the free space wavenumber  $k = \omega/c$  where  $c$  is the speed of light. With excitation at Port 1 (the incidence port), the wavenumber, the thickness  $d$  of the structure in the direction of propagation, and the calculated  $S$ -parameters were used to derive the refractive index  $n$  of a sample surrounded by vacuum using [51], [52]

$$n = \pm \left\{ \frac{1}{kd} \arccos \left[ \frac{1}{2S_{21}} (1 - S_{11}^2 + S_{21}^2) \right] + \frac{2\pi m}{kd} \right\}, \quad (3.3)$$

where  $m$  is an integer indicating multiple possible solutions. In Equation 3.3,  $n$  is negative if the permittivity and permeability are both negative. The relative wave impedance  $z$  of the sample is [51], [52]

$$z = \pm \sqrt{\frac{(1 + S_{11})^2 - S_{21}^2}{(1 - S_{11})^2 - S_{21}^2}}. \quad (3.4)$$

The  $S$ -parameters in Equation 3.3 and Equation 3.4 are referenced to the impedance of

free space,  $\eta$ . Information about the material can be used to remove the ambiguities in Equation 3.3 and Equation 3.4. When  $d$  is large compared to the wavelength  $\lambda$  in the medium, the branches of the arccosine function determined by  $m$  in Equation 3.3 can be close together. This can make finding a unique solution for  $n$  difficult. However, in the following simulations  $d$  is less than  $\lambda/4$  so that there is a unique result for  $n$ . As a result, the default branch of  $m = 0$  and positive  $n$  is chosen in Equation 3.3. A passive material means that  $\Re(z)$  is positive, so that the positive branch is chosen for Equation 3.4. Now, with unique solutions for  $n$  and  $z$ , the effective permittivity is [51], [52]

$$\epsilon_{\text{eff}} = \frac{n}{z}. \quad (3.5)$$

Here  $n$  can be well defined by a material that supports one propagating mode at a certain frequency [51], which is true here. For the frequency range studied of up to 50 GHz, there is only one propagating mode, TEM, all other modes are evanescent, and Equations 3.3 and 3.4 use the transmission and reflection coefficients for the mode that is propagating. Thus, the bulk effective permittivity relies on an abstraction to utilize the single propagating mode rather than on evanescent modes in its derivation. The results that follow for the effective permittivities of mixtures use the procedure above to determine  $\epsilon_{\text{eff}}$  unambiguously.

### 3.4 Modeling of Irregular Crystals

Several different types of irregular inclusions are analyzed here in the following subsections.

### 3.4.1 Modeling of Irregular Crystals in CST

An important goal of this research is modeling inclusions of a size and shape representative of materials comprising irregularly-shaped crystal inclusions. For reference, the crystal size of the irregular energetic material HMX is typically 0.15 mm [9]. This was modeled in CST as the irregularly-shaped crystal shown in Figure 3.1. This becomes an inclusion in a matrix modeled here as having a relative permittivity of 1. In Figure 3.1, the irregular crystal spans 0.15 mm in the  $z$  direction with a maximum dimension of 0.178 mm and 0.192 mm in the  $x$  and  $y$  directions, respectively. The total volume of the irregular crystal is 0.00351 mm<sup>3</sup>. The outer box shown is a cube with a side length of 0.26 mm, giving an inclusion volume fraction of  $q = 0.20$  for Figure 3.1. For propagation in free space, a unit cell side length of 0.26 mm corresponds to approximately  $0.00087\lambda$  ( $\lambda$  is the wavelength measured in mm) at the studied frequency of 1 GHz. The size of the irregular crystal is kept constant and the outer box side length is changed to obtain the various volume fractions.

EM propagation through the material is modeled using CST Microwave Studio with the crystal placed in a parallel plate transverse EM (TEM) environment [45]. With the electric field polarized in the  $x$  direction, the TEM environment is established by setting the opposite pair of normal faces in the  $x$  direction as electric walls, the opposite pair of normal faces in the  $y$  direction as magnetic walls, and the final opposite pair of normal faces in the  $z$  direction using open boundary conditions. In simulation the open faces are modeled as perfectly matched layers (PMLs) that eliminate reflections back into the TEM environment. Measurement ports are set up at the open faces (Port 1 and Port 2), defining the axis of EM propagation in the  $z$  direction, see Figure 3.2.

In Figure 3.2, the ports are separated from the mixture, providing an averaging effect

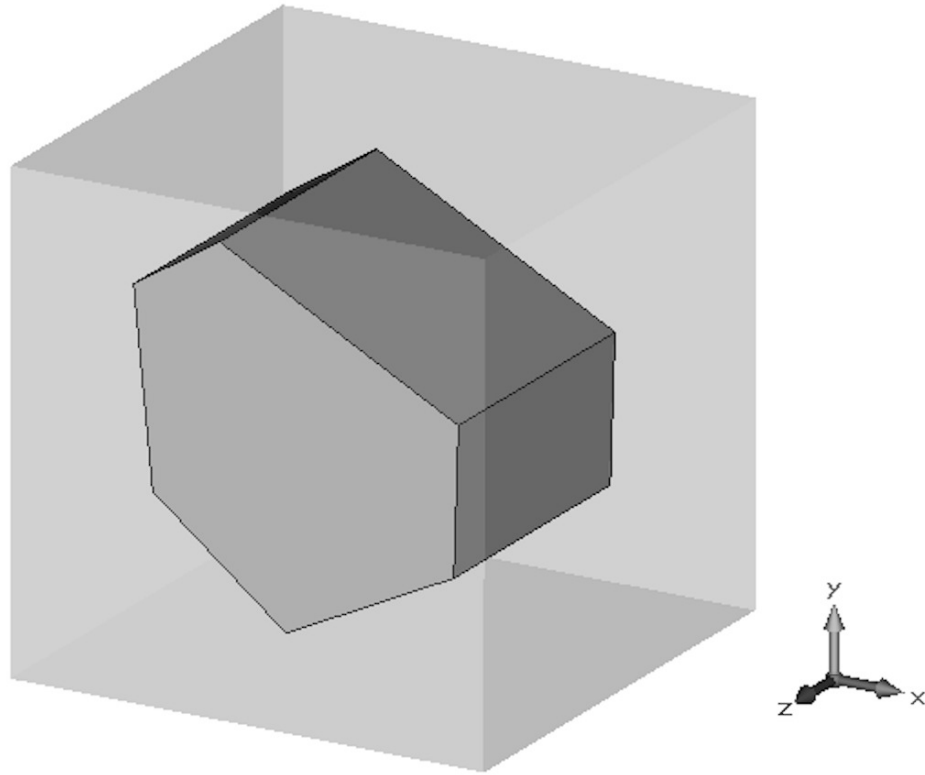


Figure 3.1: An irregularly-shaped inclusion inside an outer box. The inclusion volume fraction here is 20%. The crystal is within a cube with a side length of 0.26 mm. For comparison, with  $\epsilon_r = 28$ , the wavelength at 50 GHz is 1.13 mm.

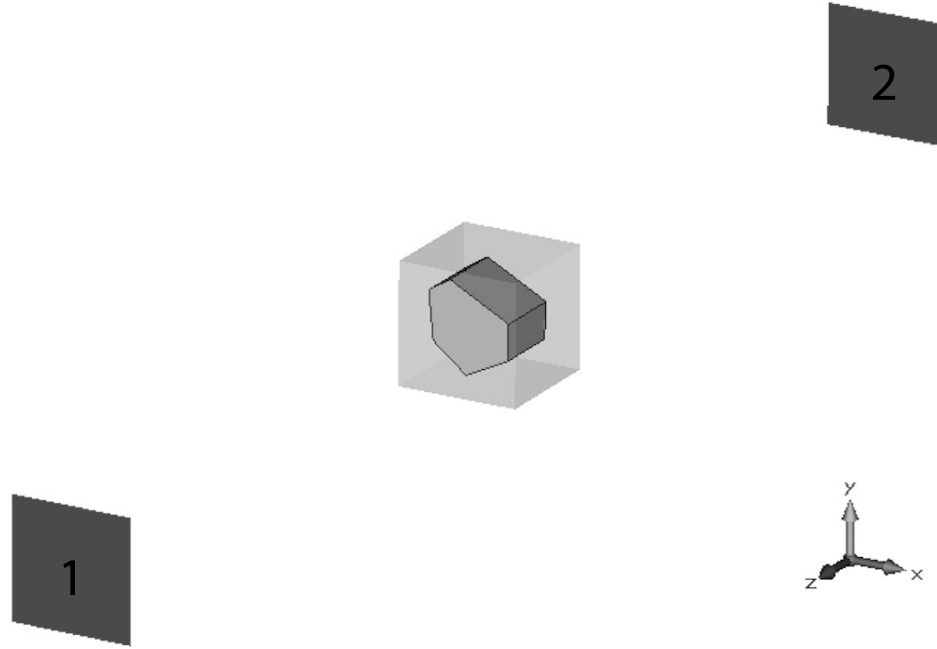


Figure 3.2: The irregular crystal of Figure 3.1 shown with waveguide ports (Port 1 and Port 2) set along the propagation axis, the  $z$  axis. In turn the  $x$  and  $y$  propagation directions were also considered with the crystal structure fixed in position and boundary conditions changed appropriately.

similar to what happens with stand-off remote sensing. Specifically, the spacing from the waveguide ports to the structure is  $\lambda/4$  of the maximum frequency component (50 GHz) of the applied RF pulse. Propagation in free space results in a separation distance of 1.5 mm for both ports in Figure 3.2. Measurements at the ports shown in Figure 3.2 were referred to reference planes on the surface of the cube also shown in Figure 3.2. This yielded the  $S$ -parameters used with Equation 3.3 and Equation 3.4 to determine the effective permittivity of the mixture calculated using a Gaussian pulse excitation signal, Fourier analyzed temporal response, and Equation 3.5.

One of the issues in EM modeling is that the size of the structure that can be simulated is limited and it is necessary to establish simulation boundaries close to the structure being investigated. Thus the possible impact that the boundary conditions have on the extracted results is a concern. The TEM waveguide environment is necessary to extract the effective permittivity and the environment (i.e., the TEM set of boundary conditions) emulates a large structure that mirrors cells [44] as shown in two dimensions in Figure 3.3. Other periodic boundary conditions emulate structures with other arrangements of repeating cells. In the following it is shown that the boundary conditions chosen have negligible effect on energy localization and, by extrapolation, on effective permittivity.

### 3.4.2 Energy Localization

EM remote probing of compounds presents the material with an RF pulse resulting in time-localized energy concentrations rather than steady-state energy concentrations. Temporal localization of energy is explored in this section using the Gaussian pulse shown in Figure 3.4 (with an appreciable frequency content from 0 to 50 GHz) and the irregularly-shaped crystal shown in Figure 3.1. An irregularly-shaped crystal of HMX

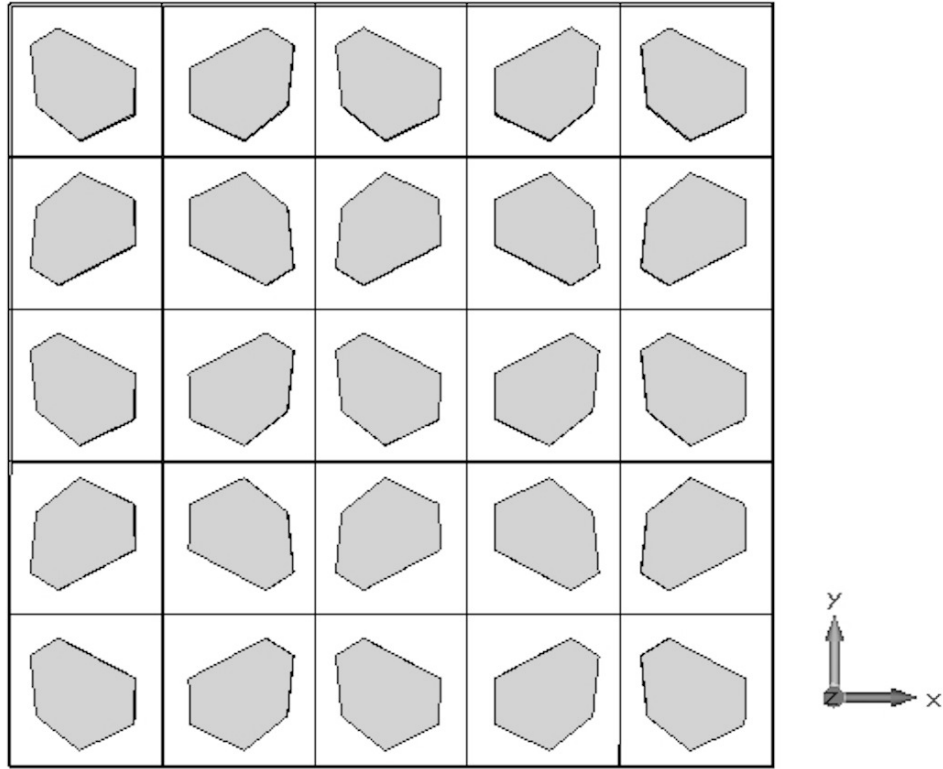


Figure 3.3: Cross section of the larger emulated structure based on a unit cell shown in Figure 3.1. The electric and magnetic boundary conditions of the TEM environment create electric and magnetic mirror boundaries, extended here for the 25 inner most cells.

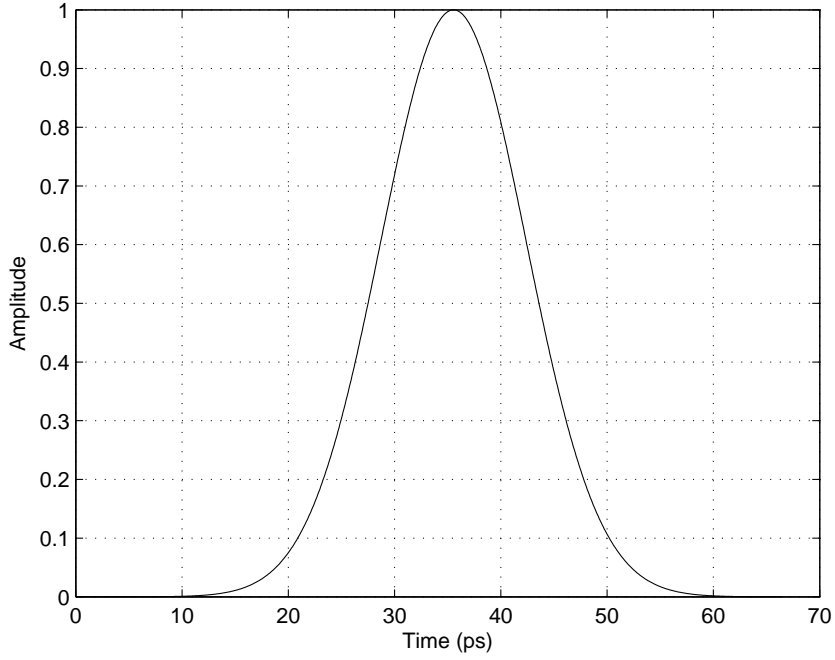


Figure 3.4: Gaussian pulse excitation signal used in simulation.

(having low real relative permittivity of 2.03 [53], [54]) in a binder having a relative permittivity of 1, and in the TEM environment has the (near-maximum) temporal energy distribution shown in Figure 3.5. That is, this is the EM energy distribution close to the point in the mixture that has the highest electrical energy concentration at any position and time.

It is seen that the electric energy density localizes around the edges and corners of the crystal as expected [45]. These corners and edges are specifically the ones closest to the outer box, i.e. the adjacent crystal for the emulated structure, in the polarization axis of the applied electric field (the  $x$  axis here). Before considering alternative boundary conditions, consider energy localization for a high permittivity material. For a zirconia-like high permittivity inclusion (with real relative permittivity of 28 [55]) the resulting



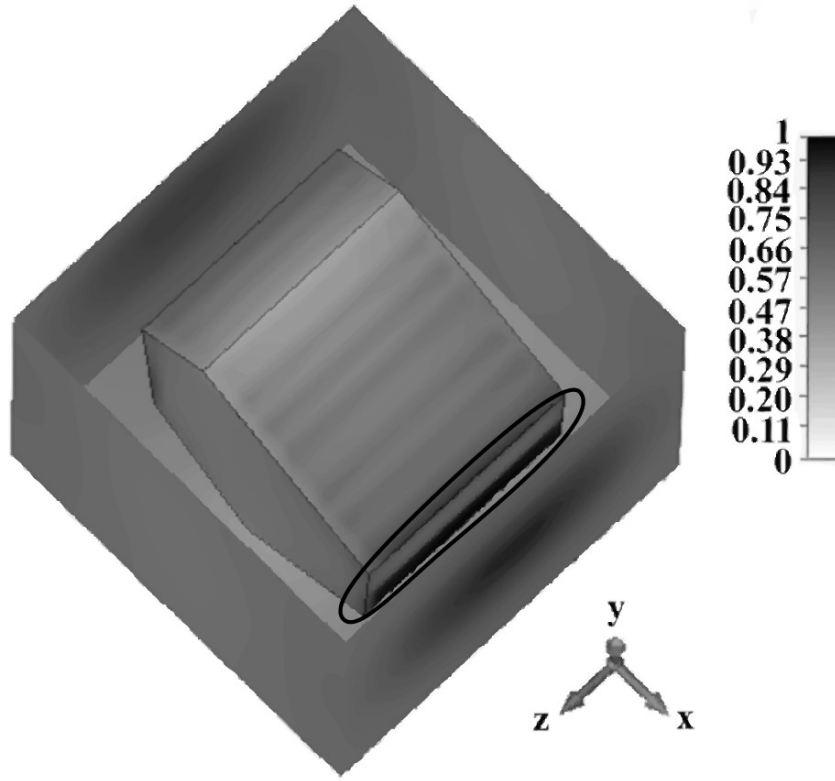


Figure 3.5: Peak electric energy density at  $t = 40$  ps for the HMX-based composite (calculated as  $\text{J/m}^3$  and here normalized to a maximum of 1) with highest density at the edges and corners indicated by the black oval. Calculated using the TEM environment with the applied electric field polarized in the  $x$  direction and propagating in the positive  $z$  direction.

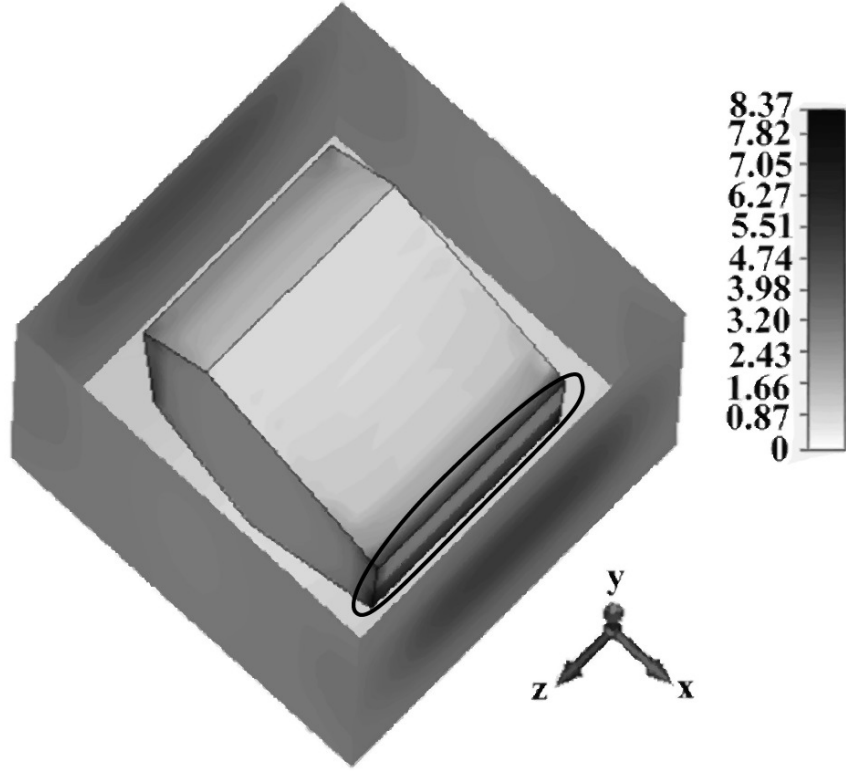


Figure 3.6: Peak electric energy density for the zirconia-like high permittivity inclusion normalized to the energy density in Figure 3.5. Conditions correspond to those in Figure 3.5.

electric energy density in the composite is given in Figure 3.6. The simulation conditions are the same as for Figure 3.5. Again the electric energy density localizes at the same corners and edges of the inclusion. Now, the peak electric energy density is approximately 8 times greater than with the composite with the HMX (low permittivity) inclusion.

To investigate the effect of the specific boundary conditions on energy localization, simulations were repeated with periodic boundary conditions at the  $y$ - $z$  and  $x$ - $z$  planes on the boundaries. This creates a repeating non-mirrored periodic structure in the  $x$  and  $y$  directions. With these boundary conditions it is also necessary to change the

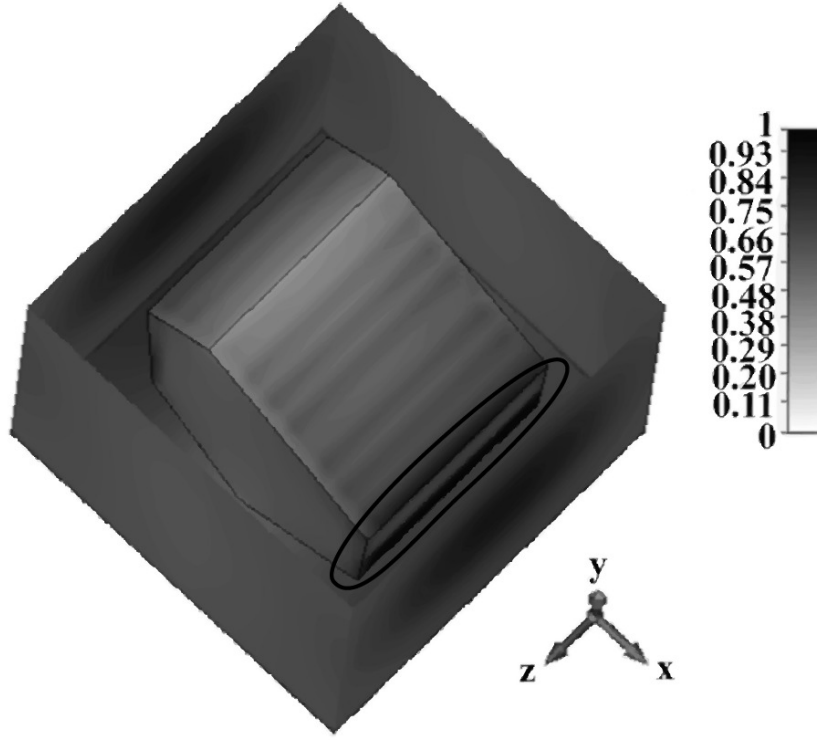


Figure 3.7: Normalized peak electric energy density for the HMX (low permittivity) inclusion with highest density at the edges and corners indicated by the black oval. Plane wave excitation and periodic boundaries are utilized. The electric field is polarized in the  $x$  direction with propagation in the positive  $z$  direction.

source excitation from a waveguide port to a plane wave. The plane wave is linearly polarized, propagating along the  $z$  axis with electric field polarized in the  $x$  direction. The peak electric energy densities for the low- and high-permittivity inclusions are shown in Figure 3.7 and Figure 3.8 respectively. In Figure 3.7 and Figure 3.8, the periodic boundary conditions result in localization of electric energy density at the corners and edges of the inclusion and the relative energy distribution is approximately identical to that obtained when the mirrored boundaries were used in simulation as in Figure 3.5 and Figure 3.6.

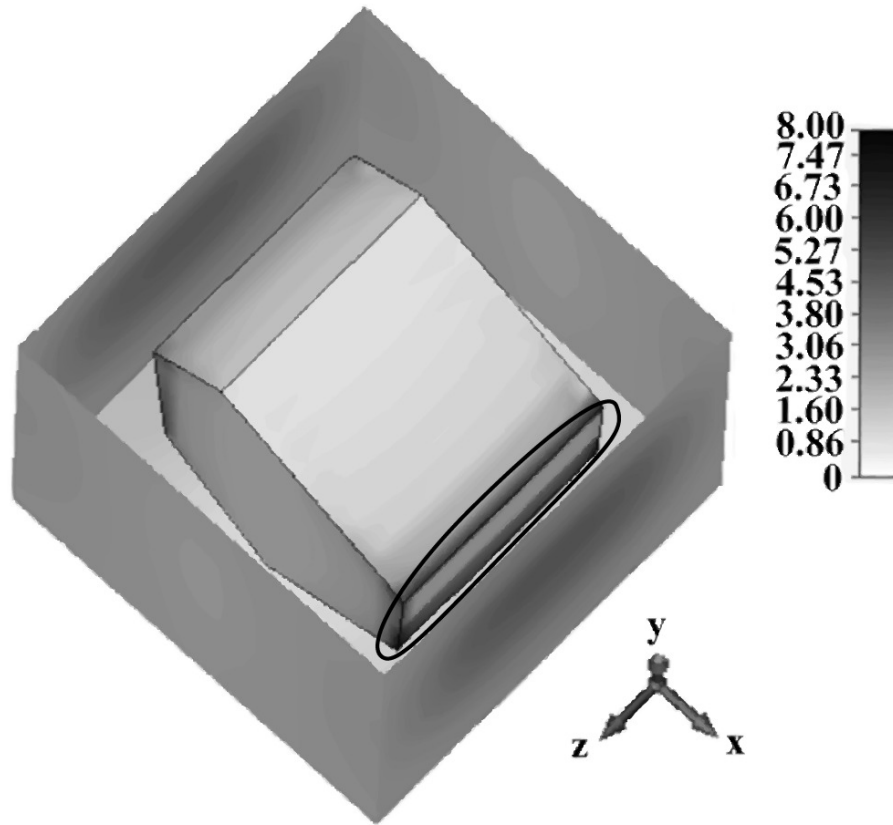


Figure 3.8: Electric energy density for the high permittivity inclusion normalized to the energy density in Figure 3.7 with the same simulation conditions as in Figure 3.7.

Comparing the energy densities in Figure 3.5 and Figure 3.7, and in Figure 3.6 and Figure 3.8, and comparing the scales in Figure 3.6 and Figure 3.8 enables the important conclusion to be reached that the simulation conditions have little effect on energy density. Figure 3.6 and Figure 3.8 show the energy density when the high permittivity inclusion is used with the simulation reported in Figure 3.6 using mirror boundaries and Figure 3.8 using periodic boundaries. The peak energy density differs by less than 5%. Thus the results in Figure 3.5 to Figure 3.8 show that there is no significant dependence of electric energy localization on simulation boundary conditions. This conclusion was reinforced by simulations with the crystal rotated and energy density again found to have little dependence on boundary conditions. With these results, the effective permittivity of the compounds can be explored without being concerned with the impact of boundary condition choice. Specifically TEM conditions are used, which enables the effective permittivity to be extracted using scattering parameters that can be conveniently extracted using the TEM environment.

### 3.4.3 Effective Permittivity with HMX Inclusions

HMX has been measured to have a relative electrical permittivity from 1 to 6 GHz of  $\epsilon_r = 2.03 - j0.0035$  and this is expected to be constant up to 20 GHz [53], [54]. The flat permittivity indicates that the loss mechanism is due to dielectric relaxation and that, at least between 1 and 6 GHz, there is negligible loss due to material conductivity. The real component of the effective relative permittivity,  $\Re(\epsilon_{\text{eff}})$ , at 1 GHz derived from EM simulations for the HMX-based compound versus filling factor is compared to that calculated using the conventional mixing theories in Figure 3.9.

For the results in Figure 3.9 derived from EM simulations, a total of 6 propagation

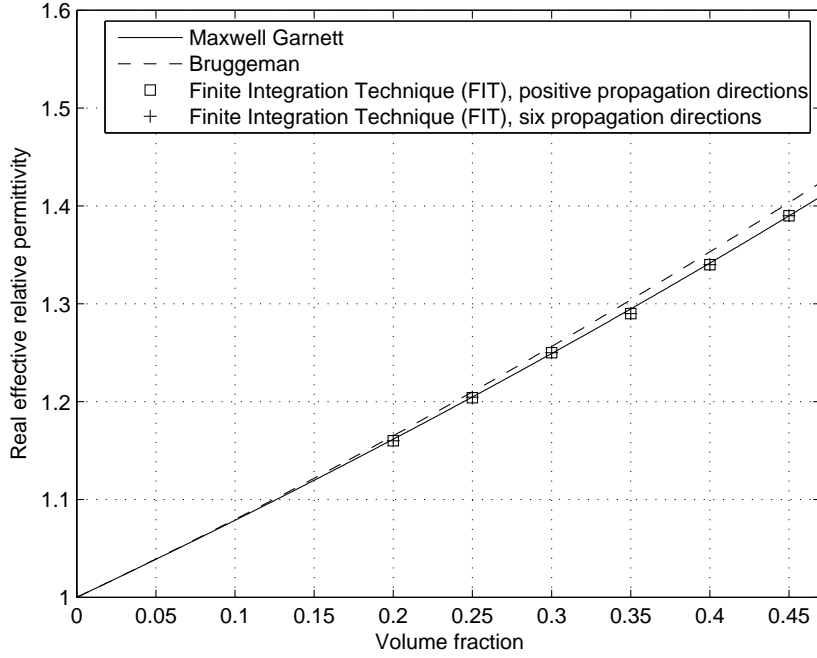


Figure 3.9: Plots of the real component of the effective relative permittivity versus volume fraction, i.e. filling factor  $q$ , for a compound with irregular HMX crystal inclusions. The squares identify the effective permittivities calculated (using EM simulated results) as the equally weighted average of the effective permittivities extracted for each of the three positive orthogonal propagation directions. The plus signs identify the effective permittivities calculated similarly but now considering both positive and negative propagation directions. Also shown are the effective permittivities calculated using the Maxwell Garnett and Bruggeman mixing theories.

directions were considered in turn. Both the forward and reverse propagation directions along each of the 3 coordinate axes ( $x$ ,  $y$ , and  $z$ ), each corresponding to a unique polarization of electric field,  $E$ , are used to gather six independent results for effective permittivity according to Equation 3.3 through Equation 3.5. Figure 3.9 compares  $\Re(\epsilon_{\text{eff}})$  taken as the arithmetic average of either just the positive propagation directions, or of all six directions. In Figure 3.9, the forward and reverse propagation directions for a given polarization yield the same effective permittivity within 1% and the two averaging schemes yield results within 1%. Thus, while individual permittivity values differ among  $x$ ,  $y$ , and  $z$  polarizations, effective permittivity is independent of propagation direction for the same electric field polarization. As an additional test, the unit cell was doubled in the direction of propagation, and the calculated effective permittivity was found to differ from the situation of a single unit cell in the propagation direction by less than 0.05%.

At least for the low permittivity contrast material (as with the HMX compound here), the results shown in Figure 3.9 for the simulated effective permittivity closely follow the predictions of the Maxwell Garnett and Bruggeman mixing theories even for high filling factors. At a 45% volume fraction,  $q = 0.45$ , the discrepancy of the four results is less than 0.94%. The Maxwell Garnett and Bruggeman mixing theory results were based on an assumption that the inclusions are spheres and that the spheres are not close to each other (corresponding to low filling factors typically under 10%) [42]. That is, for a low permittivity contrast granular material, the Maxwell Garnett and Bruggeman mixing theories can be used with irregular inclusions and with filling factors up to 45% within 1% error.

### 3.4.4 Effective Permittivity with High Permittivity Inclusions

In this section the previous results for granular materials having low permittivity inclusions are compared to those for a granular material having a high permittivity contrast between the inclusions and the matrix. The material examined has zirconia-like crystal inclusions. The zirconia-like crystals have a relative permittivity of 28, a  $\tan \delta$  (ratio of imaginary over real permittivity) of 0.0009 (measured at 1 GHz [55]), have negligible conductivity, and have the same shapes as the HMX crystals to remove crystal shape as a variable. Using the same simulation environment as used previously, the calculated effective electrical permittivities at 1 GHz are compared to those derived using the Maxwell Garnett and Bruggeman mixing theories in Figure 3.10. As before the simulated effective permittivity is independent of propagation direction. Now, however, there is a significant difference between the effective permittivities calculated and the classic mixing theories. The discrepancy is near 1% up to a volume fraction of 0.05 growing to 22% and 61% differences from the Maxwell Garnett and Bruggeman mixing theories, respectively, at a volume fraction of 0.45. This compares to less than 1% discrepancy at this volume fraction for the lower permittivity HMX compound.

### 3.4.5 Summary

The Maxwell Garnett and Bruggeman mixing theories are based on spherical and regularly ordered inclusions and are generally accepted as being applicable for volume fractions of 0.1. The investigations here have shown that with a small permittivity contrast between the matrix material and the inclusion (here 2.03), the Maxwell Garnett and Bruggeman mixing theories are accurate at high filling factors and for irregular structures. However, with a high permittivity contrast between the inclusion and the matrix



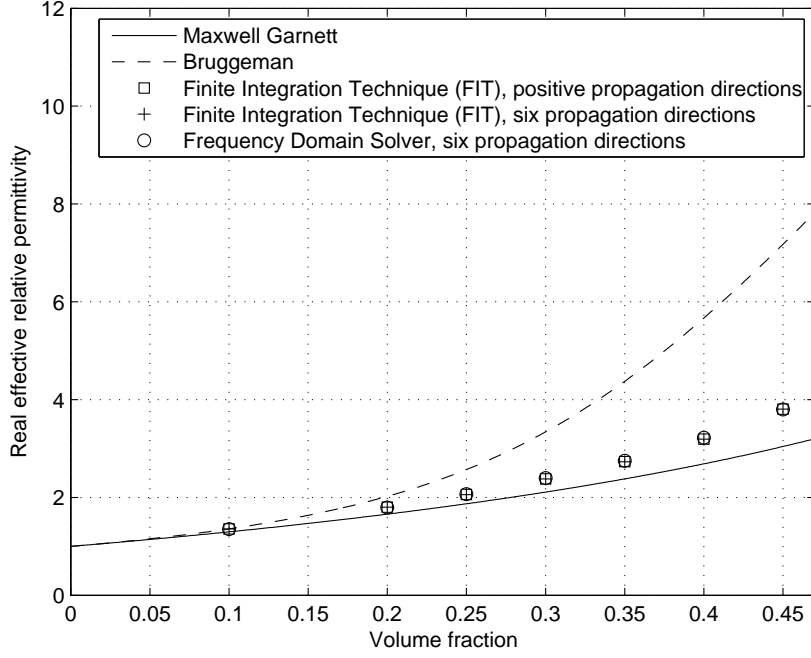


Figure 3.10: Plots of the real component of the effective relative permittivity (derived from EM simulation results) versus filling factor for an irregular high permittivity inclusion crystal. The squares indicate the equally weighted average of the effective permittivities calculated for each of the three positive orthogonal propagation directions. The plus signs indicate the equally weighted average effective permittivities of the positive and negative propagation directions (6 total). The circles indicate the results from using the Frequency Domain Solver. Also shown are the effective permittivities calculated using the Maxwell Garnett and Bruggeman mixing theories.

there is a significant departure between the predictions of the conventional mixing theories and the simulated effective electrical permittivity of granular compounds. From Figure 3.10 it is also evident that for irregularly-shaped inclusions, high permittivity contrast between inclusion and matrix material produces significantly different results from conventional mixing theories at filling factors above 0.05. Thus for high filling factors as seen in Figure 3.10, the traditional mixing theories do not accurately predict the effective properties of irregularly shaped mixtures when the permittivity contrast of the inclusion and of the matrix is high. This observation is compatible with previously reported research results for high permittivity contrast when the inclusions have a regular shape [42], [44].

### 3.5 Modeling of Multiple Crystals

This section continues the investigation of compounds with a high permittivity contrast scenario but now using multiple cube crystal inclusions in an ordered arrangement in order to study the properties of a large volume with multiple inclusions but now with a regular shape. The use of a regular shape simplified the gridding used in simulation and resulted in a simulation model that fit in the available 160 GB of RAM. An example of such a structure is shown in Figure 3.11. In Figure 3.11, each cube is 0.056 mm on a side and the side length of the outer box is 1.37 mm so that the volume fraction is 5%. For propagation in free space at 1 GHz, a unit cell size of 1.37 mm corresponds to approximately  $0.0046\lambda$  ( $\lambda$  is the wavelength measured in mm). Also shown in Figure 3.11 are Ports 1 and 2, the waveguide simulation ports. The side length of each cube inclusion varies with volume fraction and increases to approximately 0.15 mm for a 0.95 volume fraction. The inclusions are the high permittivity material and the matrix has a relative

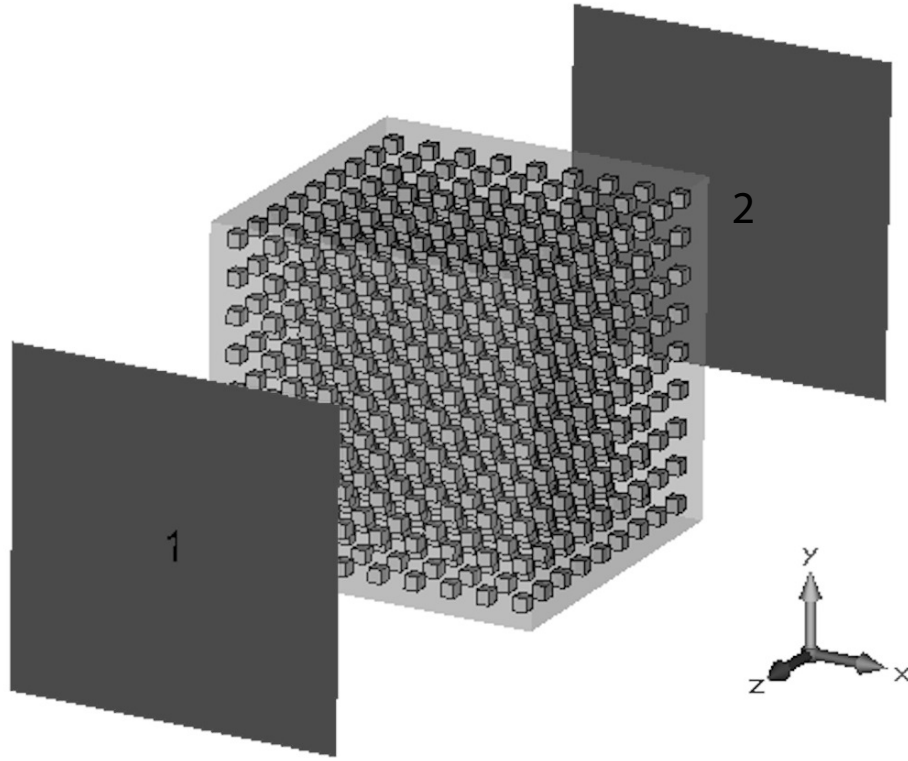


Figure 3.11: A total of 729 cube crystals (inclusions) arranged on a grid within a free space outer block. The volume fraction of inclusions here is 5%.

permittivity of 1. Results of the simulated effective permittivity versus volume fraction are given at 1 GHz in Figure 3.12.

In Figure 3.12, the effective permittivity derived from simulations closely matches the predictions of the Maxwell Garnett mixing theory for all volume fractions. Comparing Figure 3.12 with Figure 3.10, with the same high permittivity contrast, irregular inclusion shapes exhibit greater effective permittivity differences from established theory (see Figure 3.10) than when symmetric and ordered inclusion crystals on a grid are considered (see Figure 3.12). It is also possible that the larger structure, as with the Figure 3.12 results, provides a greater averaging effect than the thin layer of crystals considered with

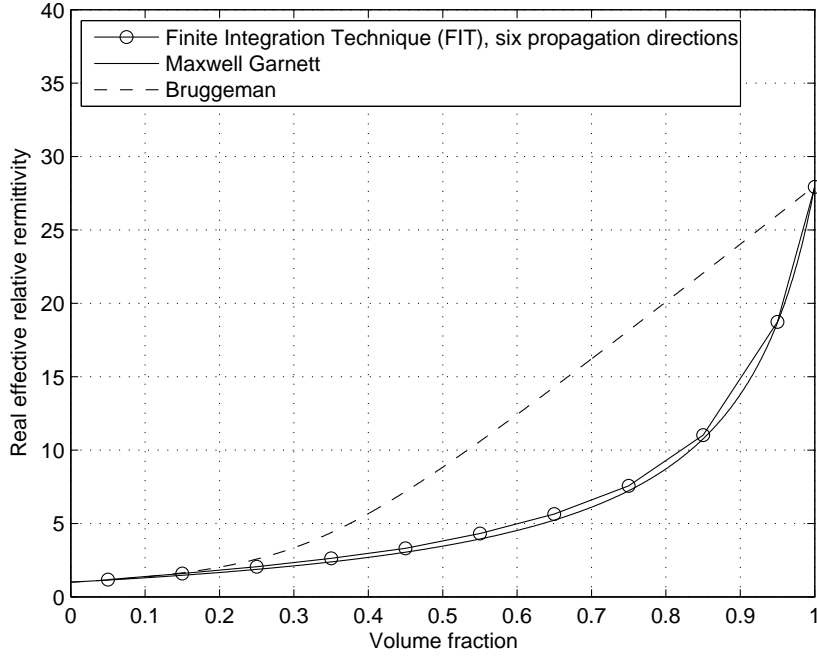


Figure 3.12: Plots of real effective relative permittivity,  $\Re(\epsilon_{\text{eff}})$ , versus various filling factors for high permittivity cube inclusion crystals on a grid along with various bounds.

Figure 3.10. This is examined further by considering properties of a crystal while it is rotated.

### 3.6 Rotated Crystals

This section considers the electrical characteristics of crystals that are both regularly-shaped and irregularly-shaped when the crystals are rotated, with permittivity results taken at 1 GHz. Effective permittivity is calculated as the inclusion crystals are rotated, and this behavior is compared with plots of cross-sectional area. The zirconia-like crystals having high permittivity contrast are considered since these were found to have the greatest deviation from established theory previously. However, the crystal is now rotated

around each of the coordinate axes ( $x$ ,  $y$ , and  $z$ ) to investigate the influence of crystal orientation on the determination of effective relative permittivity. These are particularly interesting effects as they form the basis of a sensing modality with the source of illumination moving rather than rotation of the crystal inclusions. Note that the manufacture of many compound objects results in aligned crystals.

### 3.6.1 Cube-shaped Rotated High Permittivity Inclusions

The analysis begins with a simple rotation scenario, a high permittivity cube crystal inclusion with a volume fraction of 0.10, see Figure 3.13. In Figure 3.13, the inner cube has a side length of 0.195 mm and the outer box has a side length of 0.420 mm. At 1 GHz a unit cell size of 0.420 mm corresponds to approximately  $0.0014\lambda$  ( $\lambda$  is the wavelength measured in mm) for propagation in free space. The effect of rotation on effective permittivity with the electric field polarized in the  $x$  direction is shown in Figure 3.14. Figure 3.14 indicates that when the inclusion rotates around the  $x$  axis (the direction of electric field polarization), there is negligible change in  $\Re(\epsilon_{\text{eff}})$  of the mixture. However,  $\Re(\epsilon_{\text{eff}})$  does vary with rotation of the crystal around the  $y$  and  $z$  axes. Many possible sources of this rotational dependency were found with the strongest correlation being with the projection of the immediate cross-sectional area of the crystals on the plane transverse to the direction of polarization. Thus a plot of cross-sectional area fraction is shown in Figure 3.15. The cross-sectional area fraction with respect to a given axis is the ratio of the cross-sectional area of the inclusions projected in the plane normal to the axis to the area of the projection of the inclusions plus surrounding material in that plane. This ratio is calculated for the first crystal layer, which is the layer that interacts most strongly with an illuminating field. This ratio is shown in Figure 3.15 with respect to the

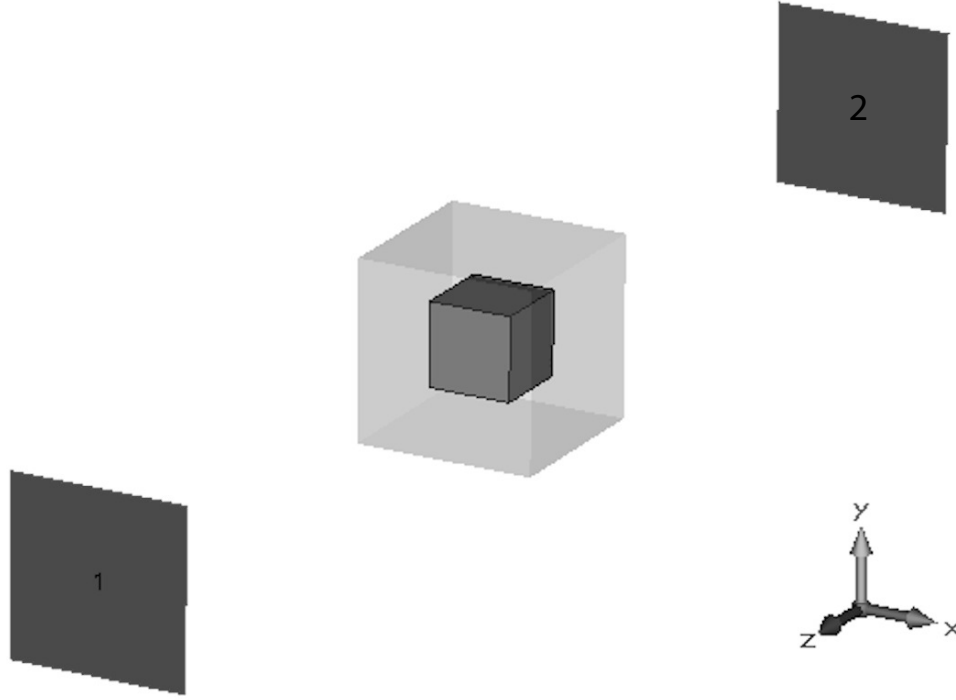


Figure 3.13: Cube-shaped high permittivity inclusion crystal at 10% volume fraction in the TEM simulation environment.

$x$  axis, here the electric field polarization.

By comparing Figure 3.14 with Figure 3.15, it is evident that overall the effective permittivity of the mixture with rotated cube-shaped inclusion follows the behavior of the cross-sectional area fraction graph when rotated about the corresponding axis. If the cross-sectional area fraction is constant (as is the case for the  $x$  axis rotation here), the effective permittivity is also approximately constant. However, from  $40^\circ$  to  $50^\circ$  rotation around the  $y$  and  $z$  axes, the cross-sectional area fraction continues to increase but the effective permittivity goes down. Outside this narrow range of angles there is a high correlation of the cross-sectional area and effective permittivity.

Next, another cube-shaped high permittivity inclusion is used but this time at 20% filling factor to see how the effective permittivity versus rotation angle is altered when

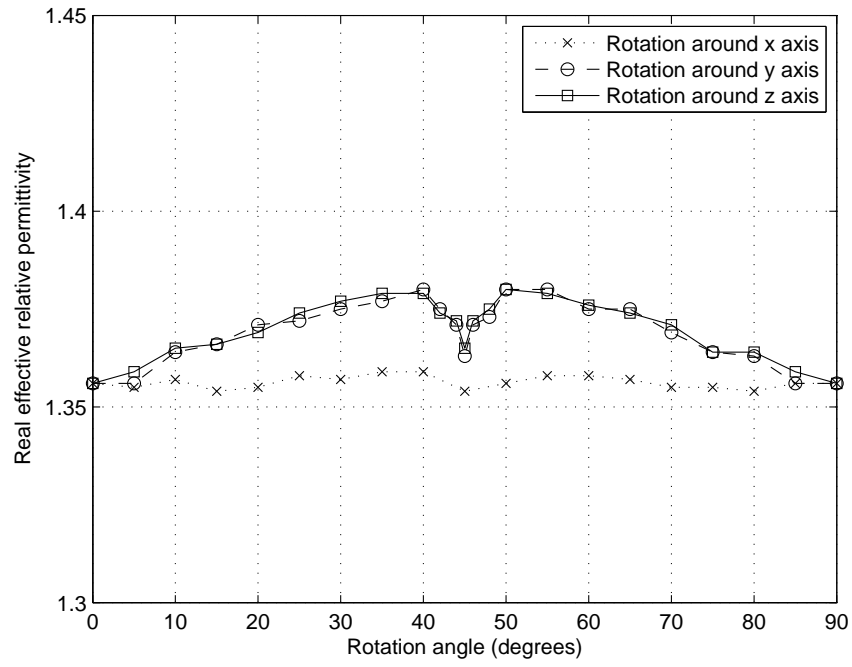


Figure 3.14: The real effective relative permittivity,  $\Re(\epsilon_{\text{eff}})$ , of a high permittivity cube-shaped inclusion at a filling factor of 0.10 versus rotation angle around the  $x$ ,  $y$ , and  $z$  axes. Here, the electric field is polarized in the  $x$  direction.

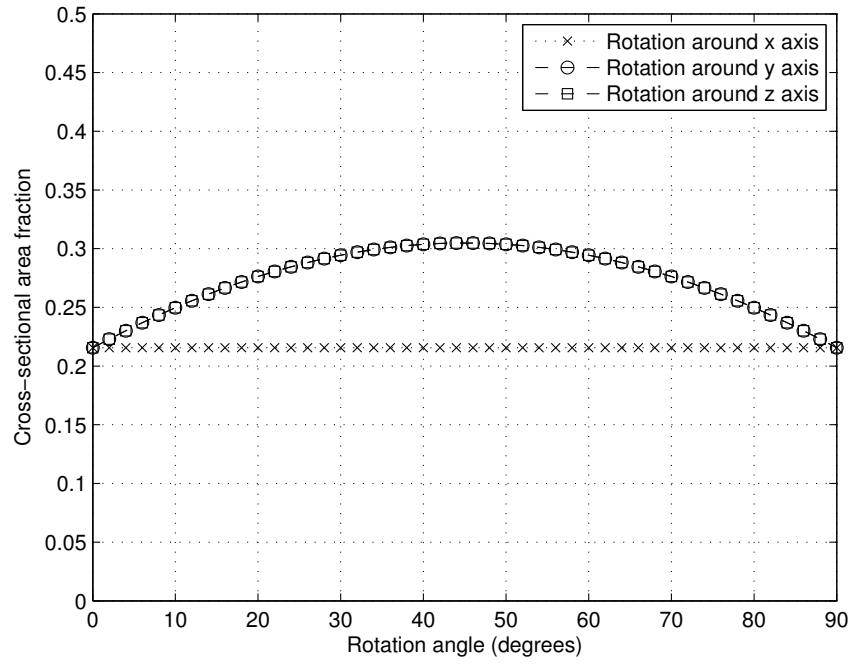


Figure 3.15: Cross-sectional area fraction from the perspective of the  $x$  axis for a 10% filling factor. For other filling factors the curves are directly scaled.



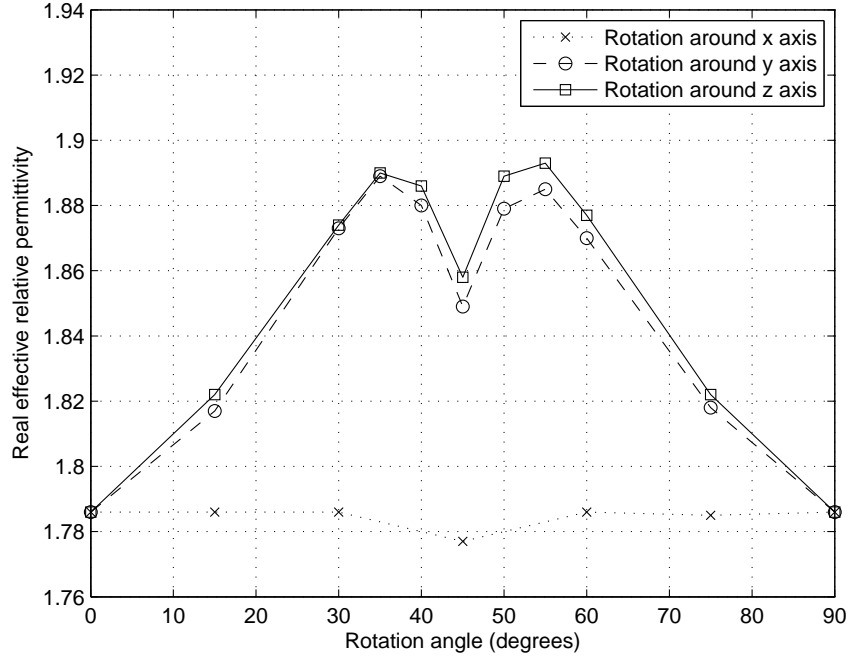


Figure 3.16: The real effective relative permittivity,  $\Re(\epsilon_{\text{eff}})$ , of a high permittivity cube-shaped inclusion at 20% volume fraction versus rotation angles around the  $x$ ,  $y$ , and  $z$  axes. The electric field is polarized in the  $x$  direction.

the filling factor is increased. The results for effective permittivity from these simulations are given in Figure 3.16. The same behavior seen with lower filling factor is observed but now exaggerated.

For the most part, effective permittivity follows the behavior of the cross-sectional area fraction. Now however, there is a wider region over which the cross-sectional area fraction increases but the effective permittivity goes down. In Figure 3.16 this dip is shown to be from  $35^\circ$  to  $55^\circ$  rotation compared to  $40^\circ$  to  $50^\circ$  rotation for the 10% volume fraction simulations in Figure 3.14. For both 10% and 20% volume fraction, as the crystal begins to rotate ( $y$  and  $z$  axis rotation here) the cross-sectional area fraction goes up. The volume fraction is constant but because the cross-sectional area fraction is

going up more of the crystal is seen by the electric field and the effective permittivity goes up. However, an inverse relationship develops between cross-sectional area fraction and effective permittivity centered around  $45^\circ$ . Since the inner crystal is rotating, at  $45^\circ$  rotation it is closest to the nearest crystal. The crystals getting close to each other causes another phenomenon to take over where an inverse relationship develops between cross-sectional area fraction and effective permittivity.

The range over which the dips in Figure 3.14 and Figure 3.16 occur can be understood by comparing the structures in these two situations. In the 20% volume fraction scenario in Figure 3.16, the inner crystal is taking up more space inside the outer box compared to the 10% volume fraction case in Figure 3.14. In Figure 3.16 the region of the dip has a larger  $20^\circ$  range for the 20% volume fraction scenario because (starting with  $0^\circ$  rotation as shown in Figure 3.13) it takes less rotation for the crystal to get close to the outer box. There is a smaller  $10^\circ$  range of the dip for the 10% volume fraction scenario in Figure 3.14, where because the crystal is so small within the outer box it takes close to  $45^\circ$  rotation for the crystals to get close enough to each other for the inverse relationship to develop.

In effect, for both the 10% and 20% volume fraction mixtures with cube-shaped inclusions all of the inclusions are rotating and at  $0^\circ$  and  $90^\circ$  the crystals are at maximum separation. At  $45^\circ$  the crystals are closest to each other, where fringe effects influence the effective permittivity.

### **3.6.2 Irregular Rotated High Permittivity Inclusions**

In this section, the same high permittivity material properties are used for the inclusion, but this time an irregular structure is used instead of the cubes from the previous sec-

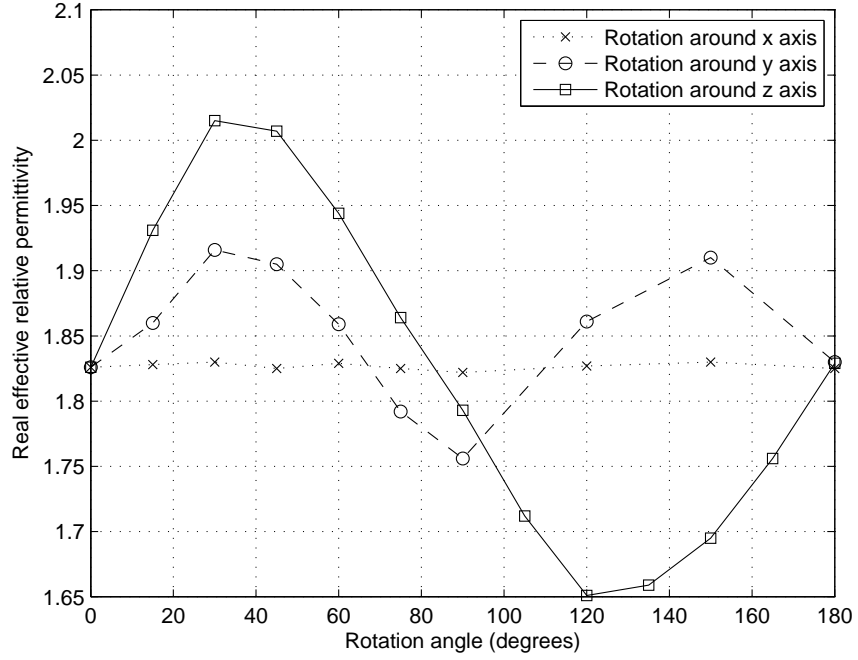


Figure 3.17: The real effective relative permittivity,  $\Re(\epsilon_{\text{eff}})$ , of a high permittivity irregular-shaped inclusion at 20% filling factor versus rotation angle around the  $x$ ,  $y$ , and  $z$  axes. The electric field is polarized in the  $x$  direction.

tion. From Sections 3.4 and 3.5, the greatest deviation from established mixing theories occurred with high permittivity irregular inclusions, and these structures are studied in more detail here. The shape of the inclusion is shown in Figure 3.1. This allows a more realistic and complicated structure to be rotated. For all of the following rotations the volume fraction is kept constant at 20%. First, the electric field is polarized in the  $x$  direction, and results of permittivity versus rotation angle are given in Figure 3.17.

In Figure 3.17, rotation around the same axis as electric field polarization shows virtually no deviation in effective permittivity with rotation angle. However, rotation around the other axes shows unique oscillating behaviors. In an attempt to understand the reasons for these oscillations in permittivity, Figure 3.18 shows cross-sectional area

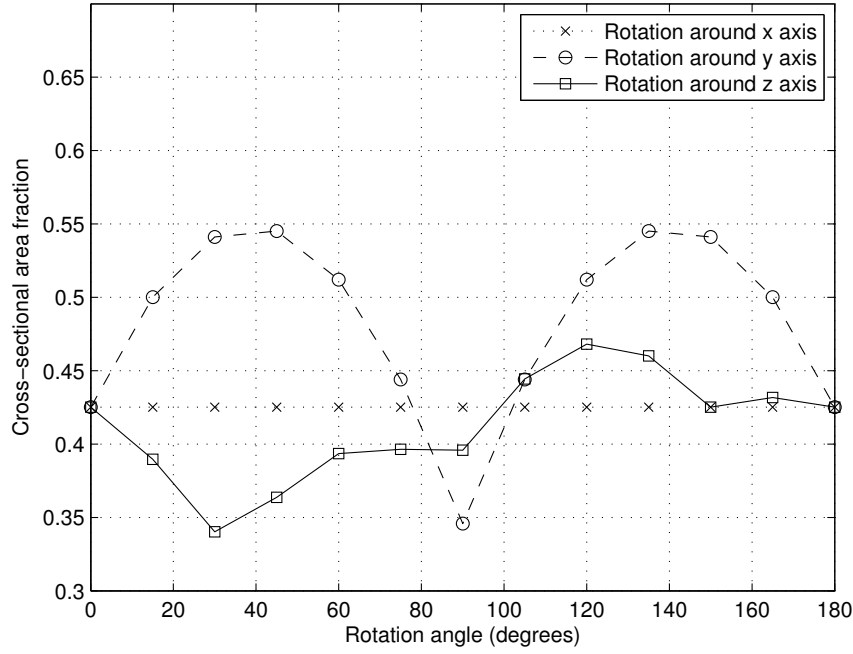


Figure 3.18: Cross-sectional area fraction of the rotated irregular crystal from the perspective of the  $x$  axis (electric field polarization axis) as the crystal is rotated around a given axis.

fraction looking along the  $x$  axis (the electric field polarization axis) as the irregular crystal is rotated. By comparing Figure 3.17 with Figure 3.18, the behavior of cross-sectional area fraction with rotation follows that of effective permittivity for rotation around the  $x$  (electric field polarization axis) and  $y$  axes. The cross sectional area with rotation around the  $z$  axis oscillates just as the effective permittivity does when rotated around the  $z$  axis, but with an inverse relationship. Still, correlation between cross-sectional area fraction and effective permittivity is evident.

Next, the electric field is polarized in the  $y$  direction and the crystal is rotated around each axis. Results of effective permittivity are given in Figure 3.19. Again, in Figure 3.19 there is constant permittivity when the irregular inclusion is rotated around the  $y$  axis

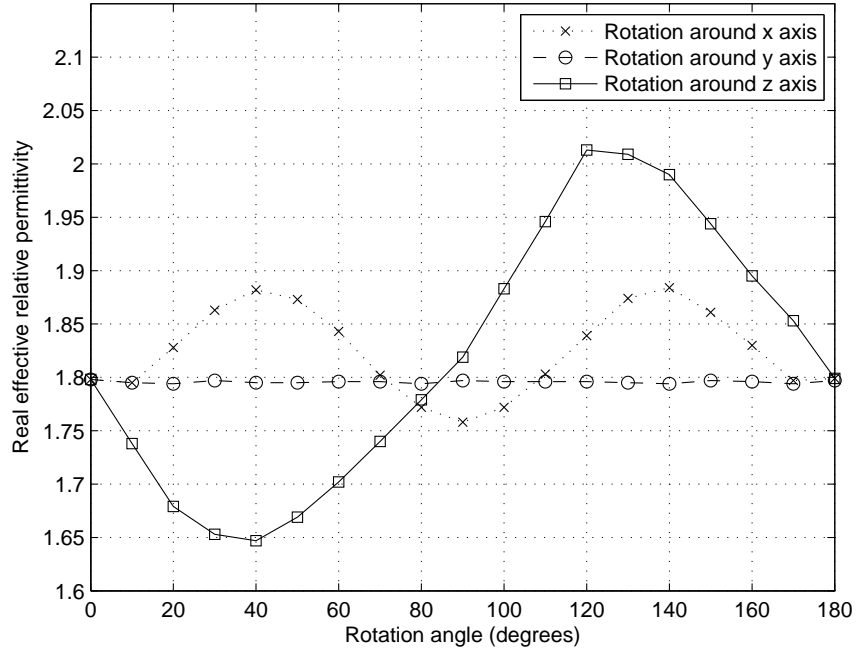


Figure 3.19: The real effective relative permittivity,  $\Re(\epsilon_{\text{eff}})$ , of a high permittivity irregular-shaped inclusion at 20% filling factor versus rotation angle around the  $x$ ,  $y$ , and  $z$  axes. The electric field is polarized in the  $y$  direction.

(electric field polarization axis), and oscillating behavior with rotation around the other axes. A plot of the cross-sectional area fraction is provided when looking from the perspective of the  $y$  axis in Figure 3.20. A comparison of Figure 3.19 with Figure 3.20 shows a direct correlation between cross-sectional area fraction with rotation and effective permittivity for rotation around the  $x$  and  $y$  (electric field polarization) axes. Rotation around the  $z$  axis causes cyclical variation in both figures, but with an inverse relationship.

Analyzing Figure 3.17 through Figure 3.20, it is evident that there are two situations where the effective permittivity variation does not show a direct relationship to the cross-sectional area fraction. These situations are rotation about the  $z$  axis for electric field polarized in the  $x$  direction (Figure 3.17 and Figure 3.18) and rotation about the  $z$  axis

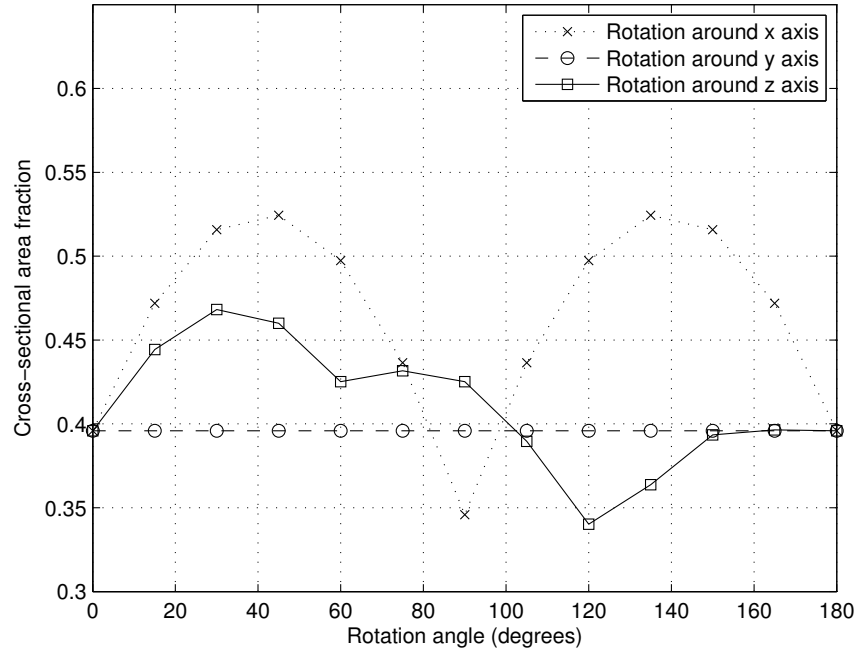


Figure 3.20: Cross-sectional area fraction of the rotated irregular crystal from the perspective of the  $y$  axis (electric field polarization axis) as the crystal is rotated around a given axis.

for electric field polarized in the  $y$  direction (Figure 3.19 and Figure 3.20). Analyzing Figure 3.1, it is seen that these two situations involve the same type of rotation. In Figure 3.1, looking down the  $x$  or  $y$  axes and rotating the crystal around the  $z$  axis causes the crystal to keep the same width (in the  $z$  direction) and rotate end over end. In this situation entire sides of the crystals are becoming close to each other. The degree of proximity is greater than in the other situations. For example, in rotation about the  $y$  axis for electric field polarized in the  $x$  direction (Figure 3.17), the edges rather than the faces of the crystals approach each other. So, just as in Figure 3.14 and Figure 3.16 where the cube crystals approaching each other resulted in an inverse relationship of the effective permittivity with the cross-sectional area fraction, the situations of rotating the crystal end over end in Figure 3.17 through Figure 3.20 cause enough of the crystals to be in close proximity for an inverse relationship to develop. The simulations have shown that close adjacency of neighboring inclusions results in an inverse relationship between cross-sectional area fraction and effective permittivity.

Finally, the electric field is polarized in the  $z$  direction and the crystal is rotated along each axis. The effective permittivity for this scenario is given in Figure 3.21. Just as shown in Figure 3.17 and Figure 3.19, when the inclusion is rotated around the same axis as the electric field polarization in Figure 3.21 ( $z$  axis) there is no change in effective permittivity. Rotation around the  $x$  and  $y$  axes shows the same oscillating behavior. For comparison purposes, Figure 3.22 shows cross-sectional area fraction looking down the  $z$  axis (electric field polarization axis) as the irregular crystal is rotated.

Comparison between Figure 3.21 and Figure 3.22 shows that the cross-sectional area fraction with rotation from the perspective of the  $z$  axis (electric field polarization axis) shows the same behavior as effective permittivity of the rotated inclusion for all axes. In Figure 3.21 and Figure 3.22, there is no inverse relationship with cross-sectional area

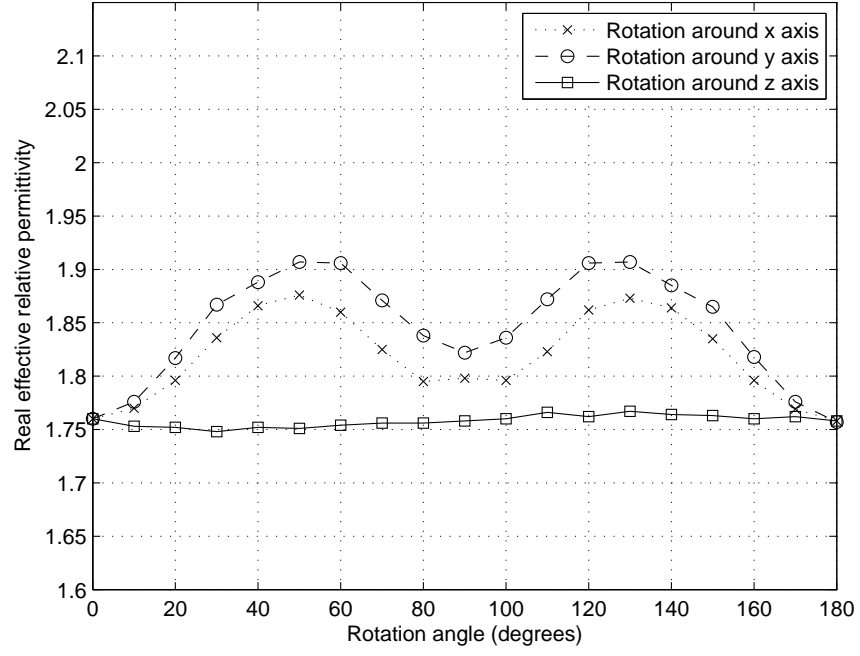


Figure 3.21: The real effective relative permittivity,  $\Re(\epsilon_{\text{eff}})$ , of a high permittivity irregular-shaped inclusion at 20% filling factor versus rotation angle around the  $x$ ,  $y$ , and  $z$  axes. The electric field is polarized in the  $z$  direction.



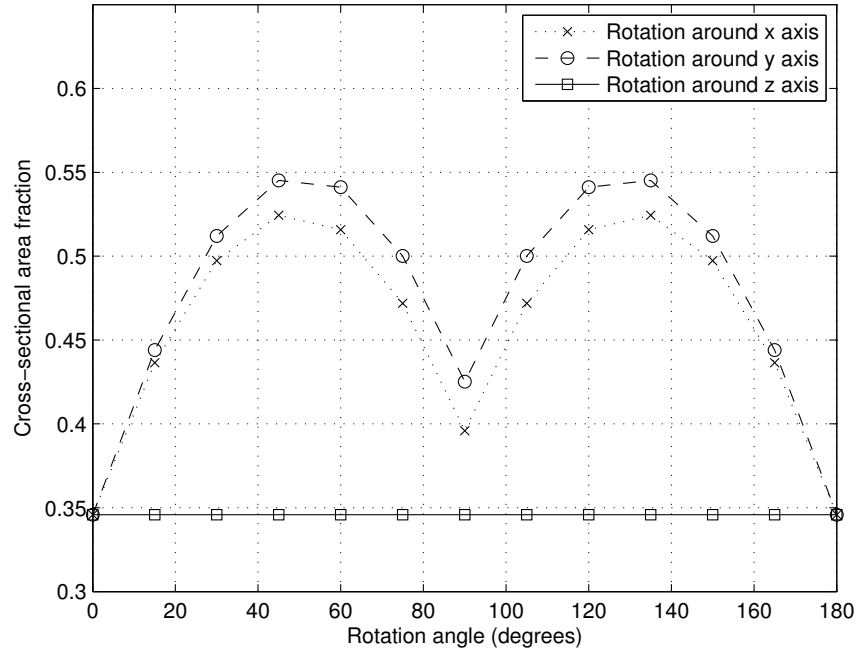


Figure 3.22: Cross-sectional area fraction of the rotated irregular crystal from the perspective of the  $z$  axis (electric field polarization axis) as the crystal is rotated around a given axis.

fraction because the situation of rotating end over end ( $z$  axis rotation) with sides of the crystals getting close to each other does not change the cross-sectional area fraction or the effective permittivity.

Overall, rotating the inclusion crystals provides strong evidence for a relationship between the cross-sectional area fraction of inclusions and effective permittivity of mixtures. For both regular and irregular crystals, the effective permittivity and cross-sectional area fraction share a direct relationship except in situations where a significant amount of the inner crystal reaches close to the outer box, or to adjacent crystals, where an inverse relationship develops.

Rotation of the inclusion crystals and changing the electric field polarization axis highlights the anisotropy of the composites studied. Effective permittivity is found to differ based on electric field polarization direction. The results in Figure 3.9 and Figure 3.10 average together the various permittivities obtained from varying the polarization direction to obtain a single effective permittivity. The sections describing rotation also highlight anisotropy even at a constant volume fraction. We change the electric field polarization axis and rotate the inclusion crystal, and the significant differences observed are highlighted in the figures.

### **3.6.3 Impact of Operating Frequency**

The results in the preceding sections present the effective permittivity at a low frequency (1 GHz) where the inclusions are small compared to a wavelength. To see the impact on effective permittivity when the operating frequency varies, Figure 3.23 shows effective permittivity for the high permittivity irregular inclusion at 20% volume fraction with electric field polarized in the  $z$  direction (results from all rotations given in Figure 3.21)

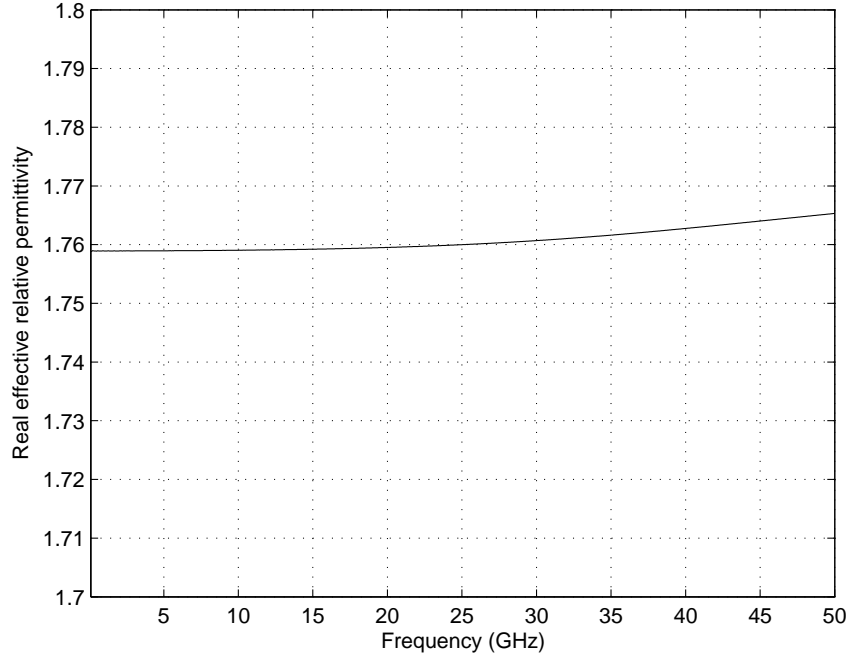


Figure 3.23: The real effective relative permittivity,  $\Re(\epsilon_{\text{eff}})$ , of the high permittivity irregular-shaped inclusion at 20% volume fraction (results for all rotation angles given in Figure 3.21) for  $0^\circ$  rotation as a function of frequency.

but specifically for  $0^\circ$  rotation. Here the unit cell has side length of 0.26 mm, corresponding to approximately  $0.00087\lambda$  at 1 GHz and  $0.043\lambda$  at 50 GHz ( $\lambda$  is the wavelength measured in mm) for propagation in free space.

With a crystal size of approximately 0.15 mm, in Figure 3.23 the effective permittivity is flat through 25 GHz before starting to increase by less than 0.5% up to 50 GHz, a negligible change from the static value. Similar results were obtained for other polarizations and rotation amounts that also show a flat response across frequency.

### 3.7 Summary

This chapter studied the effective permittivity and electric energy localization behavior of crystal-based compounds with high and low contrast between the electrical permittivity of inclusions and the matrix. The results addressed the appropriateness of the simulation boundary conditions, applicability of traditional mixing rules, and characteristics that can lead to new sensing modalities. In particular all investigations used a temporal pulse corresponding to a remote probing scenario.

For both mirrored and periodic boundaries, electrical energy localized to the greatest extent on the edges and corners of the inclusion crystal closest to another crystal in the direction of electric field polarization. The energy localization varied with time indicating the importance of not using steady-state analysis to determine peak energy density. In particular, it is only necessary to obtain high energy concentration at one point in space and time to activate an energetic material. The energy distribution and temporal response were virtually independent of the boundary conditions used in simulation. It is therefore reasonable to assume that the boundary conditions have negligible effect on the effective permittivity of mixtures extracted from EM simulations.

The effective permittivities were extracted for both forward and reverse propagation and for each electric field polarization ( $x$ ,  $y$ , and  $z$ ). Since the irregular structures are not symmetric with respect to all polarization directions, it is not surprising that directional dependency of the effective permittivity was observed. However, for the same electric field polarization the effective permittivity did not depend on forward or backward propagation direction.

The classical mixing rules for spherical inclusions, Maxwell Garnett and Bruggeman, were compared to the effective permittivities extracted from EM simulations. With low

permittivity contrast between inclusion and matrix material (here 2.03), there was little dependence on inclusion shape for effective permittivity up to a volume fraction of 0.45 (typically the highest volume fractions of energetic materials not of military grade). For high permittivity contrast (here 28), the effective permittivity derived was significantly different from the prediction of the classic mixing theories. For ordered cube inclusions on a grid, the behavior of the effective permittivity derived from EM simulations was similar to that of the Maxwell Garnett theory for all volume fractions (up to 0.45), while neither Maxwell Garnett nor Bruggeman were able to correctly predict the effective permittivity of mixtures with inclusions having irregular shapes for volume fractions above 0.05.

One of the purposes of the study was to explore new sensing modalities, that is physical behaviors that could be observed remotely with the focus here being the dependence of effective permittivity on observation direction. The effect of a moving probe was emulated by rotating the crystal in the compound. When the inclusions were rotated, there was a variation in effective permittivity of the mixture leading to anisotropy even at a constant volume fraction. Thus, the effective permittivity of a mixture varies as the angle of observation changes. As the crystal inclusions were rotated (corresponding to a variation in the angle of observation for a mixture fixed in position), the effective permittivity for a given electric field polarization axis was highly correlated to the fractional cross-sectional area of the first crystal layer from the perspective of the axis of polarization. It is this first crystal layer that most strongly interacts with an applied EM pulse. An inverse relationship between effective permittivity and cross-sectional area fraction was observed. Note that manufactured energetic materials will typically have aligned crystals. That is, there is a dependency of the observed effective permittivity on the polarization and on the angle of observation. This dependency is not accounted for in the classic Maxwell Garnett and Bruggeman mixing theories and deserves further investigation.

The next chapter continues the study of effective permittivity of composites and energy localization, but increases the complexity of the mixtures that are analyzed. Specifically, this includes mixtures with hundreds of disordered inclusions both of irregular and cube shapes.

## Chapter 4

# Electromagnetic Properties of Mixtures with Many Disordered Inclusions

### 4.1 Introduction

The previous chapter analyzed EM properties in relatively simple scenarios (single inclusions and ordered inclusions on a grid). To analyze more complex structures with greater disorder, this chapter studies the EM properties of two-component mixtures involving many disordered regularly and irregularly shaped crystals. The effective relative permittivities are calculated utilizing the time-domain Finite Integration Technique. The effective permittivity of disordered mixtures deviates from established mixing theories especially in cases of high permittivity contrast between inclusions and matrix material, and is strongly correlated to the cross-sectional area of the inclusion crystals. Electric energy density localizes at the edges and corners of inclusions in a manner independent of

inclusion shape and influenced by EM propagation direction and surrounding inclusions. For mixtures with both disordered irregular and more organized cube inclusions, energy localization increases as the EM signal travels through the mixture before decreasing due to attenuation of the propagating EM signal. With a large number of inclusion crystals (here in the hundreds) it is found that the impact on effective permittivity from differences in individual inclusion shapes is negligible.

Natural and manufactured composites comprise two or more components, and while the electrical properties of the individual components may be well known, the electrical properties of a composite are generally thought to be dependent on the shape, orientation, surface structure, and distribution of components. An understanding of the electrical properties of component mixtures, including energy localization, is important in nondestructive testing, predicting the response of rocket fuel and explosives to EM insult, remote sensing, and in industrial heating and curing.

The EM behavior of such a non-magnetic complex object is largely described by its effective permittivity. Studies of effective medium properties have used various simulation methods. The effective permittivity of a mixture has been calculated using finite difference time-domain EM simulation in two dimensions [36], [45] and three dimensions [38], [39], in two dimensions using frequency-domain finite element EM analysis [47], and in three dimensions using the frequency-domain finite difference [37], [40], [41] and finite element [42], [43], [44] methods. The random combination of variously shaped inclusions with a permittivity contrast to the embedding matrix can result in macroscopic anisotropy. The standard electrical characterization procedure is then to average the effective permittivity calculated in each of three orthogonal directions to obtain an overall effective permittivity of the mixture [42], [43], [44], [56].

Earlier studies considered a single type of inclusion in a matrix material with permit-



tivity contrasts between inclusion and matrix of up to 10 to 1 [38], [45]. These studies were limited to a few inclusions because of computational complexity, and found that the effective permittivity depended on the shape of the inclusion. The previous chapter studied the effective permittivities of mixtures modeled with a single irregular crystal shape using the FIT and found deviation from established mixing theories that was especially significant with high permittivity contrast between inclusion and matrix material. This chapter models mixtures with hundreds of irregularly and regularly shaped inclusions in a disordered arrangement. The effective permittivity results are compared to the predictions of classical mixing rules and to each other. It is shown here that with many inclusions (in the hundreds), even when there is relatively high permittivity contrast between inclusion and matrix material of up to 28 to 1, the impact of inclusion shape on effective permittivity is negligible. In addition, mixtures with many irregular and regular crystals are studied to provide insight into how the combination of individual crystals within a larger mixture impacts EM energy localization and the creation of hotspots. Again it is seen that inclusion shape has little effect on energy localization behavior.

This chapter provides a basis for understanding how pulsed microwave signals can be used to characterize materials and for understanding how pulsed microwave signals can create hotspots in materials either intentionally or inadvertently. For this reason, EM analysis is performed in the time domain.

## 4.2 Classical Mixing Rules

The classical Maxwell Garnett mixing theory gives the effective permittivity,  $\epsilon_{\text{eff}}$ , of a two-component three-dimensional mixture with spherical inclusions as [21]

$$\epsilon_{\text{eff}} = \epsilon_2 + 3q\epsilon_2 \frac{\epsilon_1 - \epsilon_2}{\epsilon_1 + 2\epsilon_2 - q(\epsilon_1 - \epsilon_2)}. \quad (4.1)$$

In Equation 4.1  $\epsilon_1$  is the inclusion permittivity,  $\epsilon_2$  is the matrix material permittivity, and  $q$  is the filling factor (i.e., the volume fraction of the inclusions). The quasistatic assumption inherent to the development of Equation 4.1 is that the inclusion size is much smaller than the EM wavelength so that the effective permittivity is independent of frequency. The Maxwell Garnett mixing theory also assumes spherical non-touching inclusions that are far apart [42], [56].

The classical Bruggeman mixing theory in three dimensions and for spherical inclusions is [22]

$$(1 - q) \frac{\epsilon_2 - \epsilon_{\text{eff}}}{\epsilon_2 + 2\epsilon_{\text{eff}}} + q \frac{\epsilon_1 - \epsilon_{\text{eff}}}{\epsilon_1 + 2\epsilon_{\text{eff}}} = 0. \quad (4.2)$$

In effect, the Bruggeman rule for the effective permittivity weights the contribution of the inclusions by  $q$  and that of the matrix material by  $(1 - q)$  [56], [57].

The Maxwell Garnett and Bruggeman mixing laws can be combined into one uniform equation [37], [44]:

$$\frac{\epsilon_{\text{eff}} - \epsilon_2}{\epsilon_{\text{eff}} + 2\epsilon_2 + \nu(\epsilon_{\text{eff}} - \epsilon_2)} = q \frac{\epsilon_1 - \epsilon_2}{\epsilon_1 + 2\epsilon_2 + \nu(\epsilon_{\text{eff}} - \epsilon_2)}. \quad (4.3)$$

where  $\nu$  is a parameter used to describe a given mixing equation. Maxwell Garnett can be obtained with  $\nu = 0$  and Bruggeman with  $\nu = 2$  [37], [44]. However, the classical mixing

rules are not directly applicable to mixtures with arbitrarily shaped inclusions [42], [56].

The maximum,  $\epsilon_{\text{eff,max}}$ , and minimum,  $\epsilon_{\text{eff,min}}$ , possible effective permittivities of a mixture are described by the Wiener bounds [36], [37], [44]:

$$\epsilon_{\text{eff,max}} = q\epsilon_1 + (1 - q)\epsilon_2 \quad (4.4)$$

$$\epsilon_{\text{eff,min}} = \frac{\epsilon_1\epsilon_2}{q\epsilon_2 + (1 - q)\epsilon_1}. \quad (4.5)$$

These maximum and minimum Wiener bounds for permittivity correspond to capacitors in a circuit connected in parallel or series respectively [36], [37]. These bounds are also applicable when the permittivities of the components are complex [58].

### 4.3 Method of Simulation

Calculated or measured scattering ( $S$ -) parameters can be employed to find the effective permittivity of a sample with a finite thickness  $d$  [49], [50], [51], [52], [56]. Here these  $S$ -parameters are derived from a time-domain EM analysis using a Gaussian excitation pulse. In particular, CST Microwave Studio [10], utilizing the time-domain FIT with hexahedral meshing, is used for EM simulations. To confirm the accuracy of the simulations, the number of mesh cells was increased until the effective permittivity converged to an asymptotic value. To achieve a change in effective permittivity of less than 1%, at least 5,000,000 mesh cells were required. Computation used an 80 core machine with 160 GB of RAM and clocking at 2.66 GHz.

The refractive index  $n$  of a sample of length  $d$  in the propagation direction can be

calculated from the  $S$ -parameters (for excitation at Port 1) as [51], [52], [56]:

$$n = \pm \left\{ \frac{1}{kd} \arccos \left[ \frac{1}{2S_{21}} (1 - S_{11}^2 + S_{21}^2) \right] + \frac{2\pi m}{kd} \right\}, \quad (4.6)$$

where the free space wavenumber  $k = \omega/c$ ,  $\omega$  is the angular frequency, and  $c$  is the speed of light. The integer  $m$  indicates that multiple solutions are possible. Also, the relative wave impedance  $z$  is defined as [51], [52], [56]:

$$z = \pm \sqrt{\frac{(1 + S_{11})^2 - S_{21}^2}{(1 - S_{11})^2 - S_{21}^2}}. \quad (4.7)$$

In Equation 4.6 and Equation 4.7 the  $S$ -parameters are normalized to the impedance of free space,  $\eta$ . When  $d$  and the wavelength  $\lambda$  are comparable, obtaining a unique result for  $n$  can be difficult. However in this chapter  $d$  is less than  $\lambda/4$  at the frequency analyzed, 1 GHz, so a unique result for  $n$  can be found and the default branch is used with  $m = 0$  and positive  $n$  in Equation 4.6. With a passive material  $\Re(z)$  is positive, so in Equation 4.7 the positive branch is taken. These solutions for  $n$  and  $z$  can be used to find the unambiguous effective permittivity for a nonmagnetic mixture as [51], [52], [56]:

$$\epsilon_{\text{eff}} = \frac{n}{z}. \quad (4.8)$$

From [51], the calculations in Equation 4.6 and Equation 4.7 utilize the transmission and reflection coefficients for the mode that is propagating, which, for the situation analyzed in this chapter, is TEM through 50 GHz.

Before the composites can be simulated in CST, their physical structure must first be defined. The next section describes an automated process for creating complex mixtures.

## 4.4 Automated Creation of Complex Composites

The manual creation of complex three-dimensional structures for use in engineering analysis is a major obstacle to analyzing physically realistic structures. A bias is invariably imposed when a mixture is manually composed and the structure rarely is representative of the process by which composites are fabricated. Properties such as packing density and anisotropies that seem to easily occur in nature are very difficult to obtain with manual arrangements. This section addresses the creation of complex three-dimensional mixtures, comprising crystals embedded in a matrix, for subsequent EM analysis. The physically realistic arrangement of the crystals is facilitated by the use of physics engine software, specifically the Bullet physics library, which renders the realistic effects in advanced computer games. A composite mixture of crystals is created by pouring a series of random crystals into a box with the crystals bouncing against each other and aligning just as they do in the real world. Higher packing densities are obtained than can be reasonably obtained with manual construction. The arrangement of the crystals obtained reflects the real world alignment of asymmetric crystals. A composite is created here and used with EM simulation software to investigate energy localization in materials.

Two of the biggest difficulties in the study of random materials are the inability of humans to make something truly random and the manual writing of an input language to describe the structures. However, significant research such as the detection and analysis of energetic materials [1]–[5] can be aided through the automated creation and simulation of complex crystalline mixtures. This section uses the Bullet physics library [11], traditionally used in gaming software, to create randomized non-overlapping irregular crystal shapes with various orientations and sizes that become part of a mixture with many crystals. This automated procedure can be run many times and can be used to create

complex 3D crystal mixtures. Then this structure is imported into an EM simulation tool to study how electric energy localizes in situations of many irregular crystals.

#### 4.4.1 Creating Multiple Irregular Crystal Structures

A two-step process is required to perform EM simulation for mixtures involving many irregular crystals. First, a structure must be created (a nontrivial process for mixtures with many irregularly shaped and scaled non-overlapping crystals) before it can be simulated.

A model of a composite structure is created with physical simulation software using the Bullet physics library. First, a set of bounding planes is constructed to form an outer box. Then, variants of different irregular crystal shapes are created at random positions above the box. An example of two of these differently shaped irregular crystals is given in Figure 4.1.

To fill each outer box, approximately 500 individually scaled and rotated irregular crystals are created. For these studies a total of seven different crystal shapes are made before they are scaled and rotated. Each crystal has a nominal size of roughly 0.15 mm on each side, and each dimension is scaled by a factor ranging from 0.1 to 1 with a Gaussian distribution, to represent crystals of varying sizes within a mixture. Even at a scaling factor of 1, the size of a crystal is much smaller than the EM wavelength.

The physics simulation library simulates the crystals falling into the box, rotating, pushing against each other and being moved by other crystals until they settle. The top of the box is closed with another bounding plane, deleting any crystals that extend outside of the box. At this point none of these irregular crystals are touching. This process of utilizing the falling crystals is repeated to obtain an array of unique structures. Each time the simulation is run a different mixture is created. Figure 4.2 and Figure 4.3 show

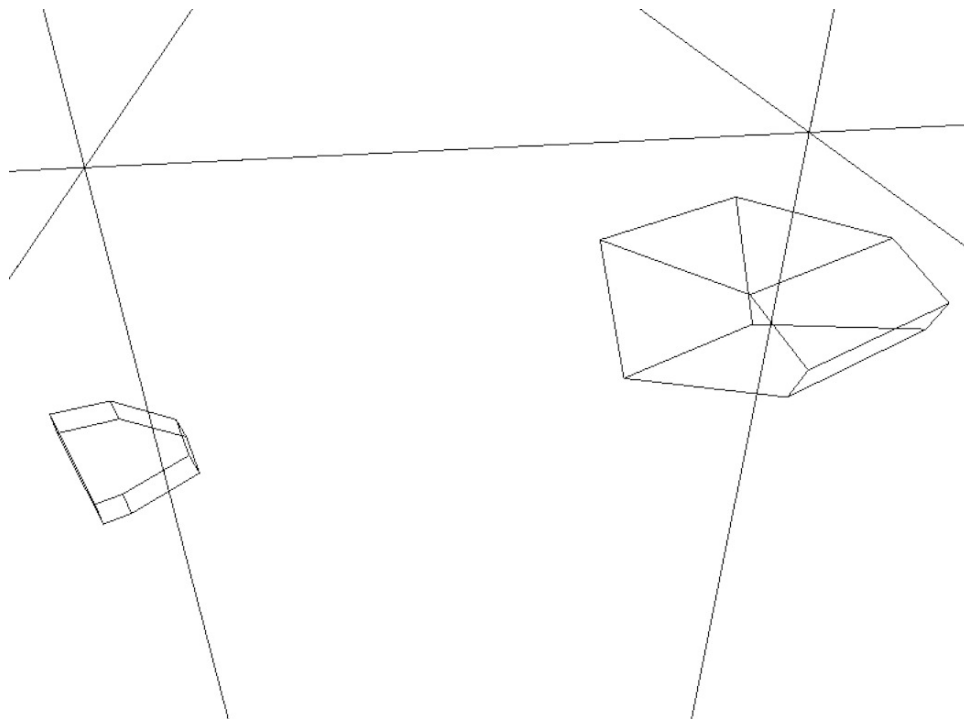


Figure 4.1: An example of two different irregularly shaped inclusion crystals, one with 8 sides (left) and one with 7 sides (right) as created using the Bullet physics library.

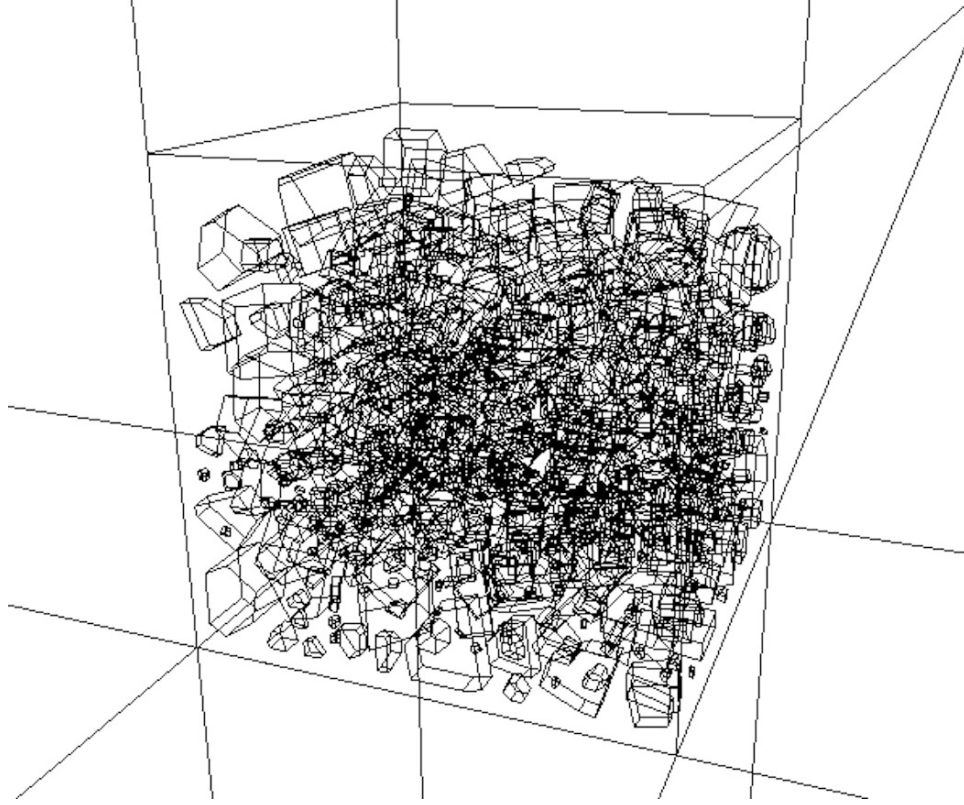


Figure 4.2: Unique structure created with 550 irregular crystals inside an outer box (with 19.5% of the outer box volume containing crystals) as created using the Bullet physics library.

two of these structures. The packing densities obtained by manually inserting crystals reached as high as 11%, while the packing densities from using the Bullet physics library reached 42%. This level is representative of the packing densities obtained with realistic structures [59].

After creating the irregular crystalline mixtures, they can then be imported into other programs such as CST Microwave Studio for EM analysis using over 5,000,000 mesh cells and an 80 core machine with 160 GB of RAM and operating at 2.66 GHz.

A structure with many irregular crystals is created at a certain volume fraction using the Bullet physics library with output of the physics library using Visual Basic for



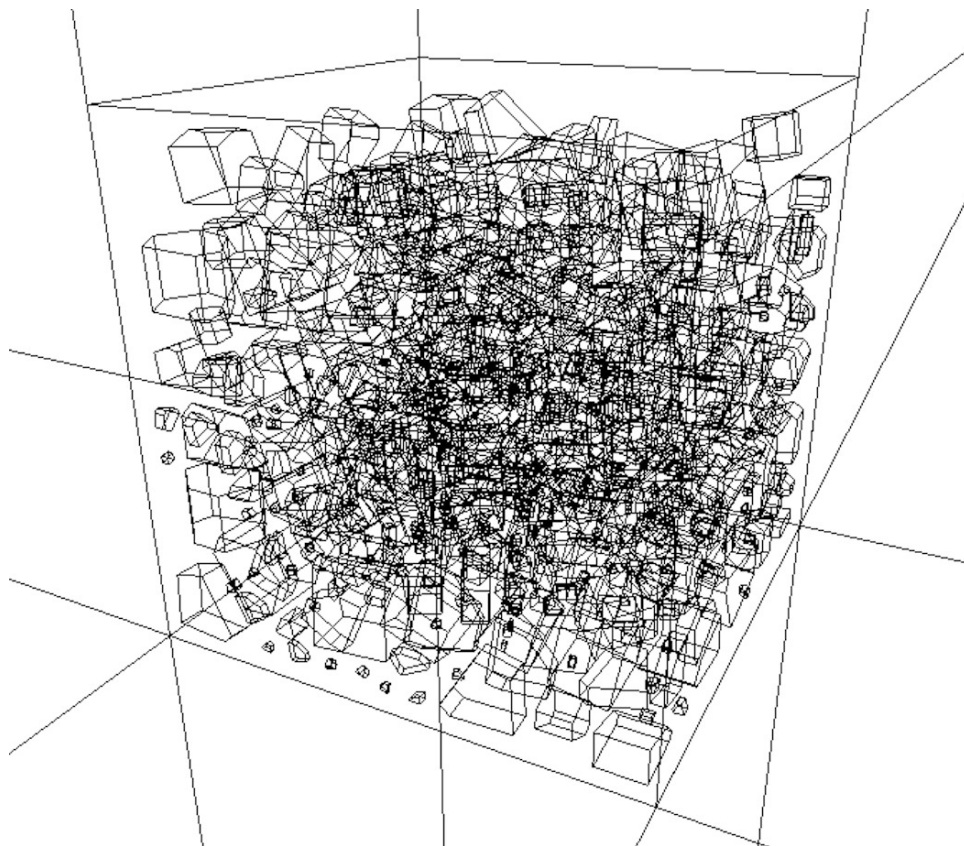


Figure 4.3: Unique structure created with 500 irregular crystals inside an outer box (with 21.4% of the outer box volume containing crystals) as created using the Bullet physics library.

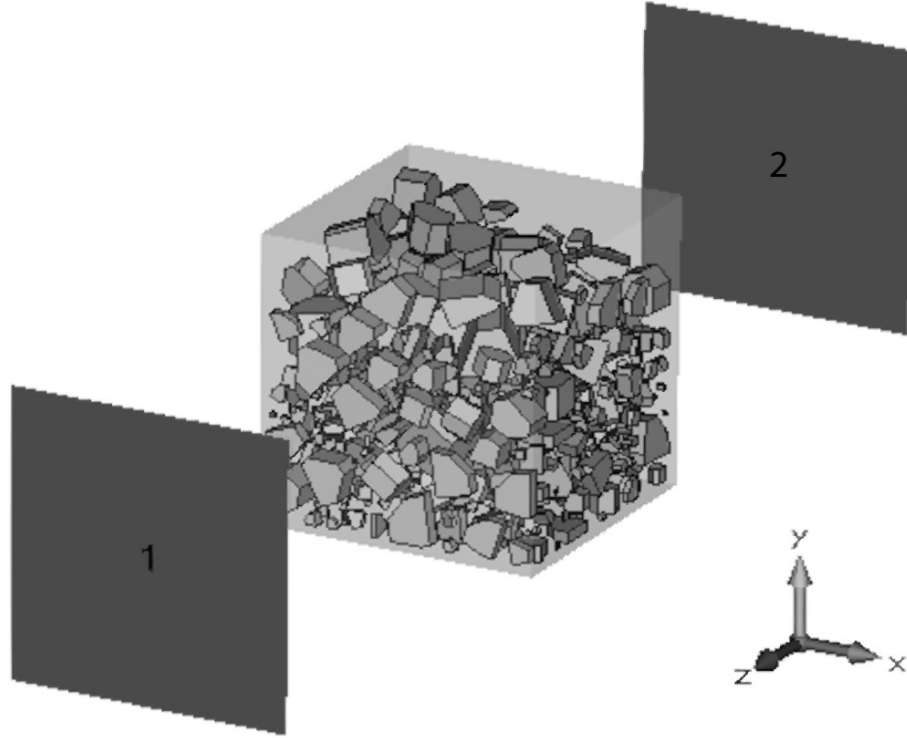


Figure 4.4: The same mixture shown in Figure 4.2 along with waveguide excitation ports after it has been imported into CST Microwave Studio for EM simulation.

Applications (VBA) code. The code is written against CSTs application programming interface (API) then imported into CST Microwave Studio for EM analysis. The structure in Figure 4.2 is shown in Figure 4.4 but now in the CST Microwave Studio environment along with waveguide excitation ports 1 and 2 used in simulation. Similarly, the complex mixture in Figure 4.3 as seen within CST Microwave Studio is given in Figure 4.5.

By using CST Microwave Studio, an EM pulse can be propagated through the composite incident at either ports 1 or 2 in Figure 4.4 and Figure 4.5. The time-domain solver within CST is used to propagate a Gaussian pulse (with frequency content of 0 to 50 GHz) through the mixtures in Figure 4.4 and Figure 4.5. Results of this simulation can

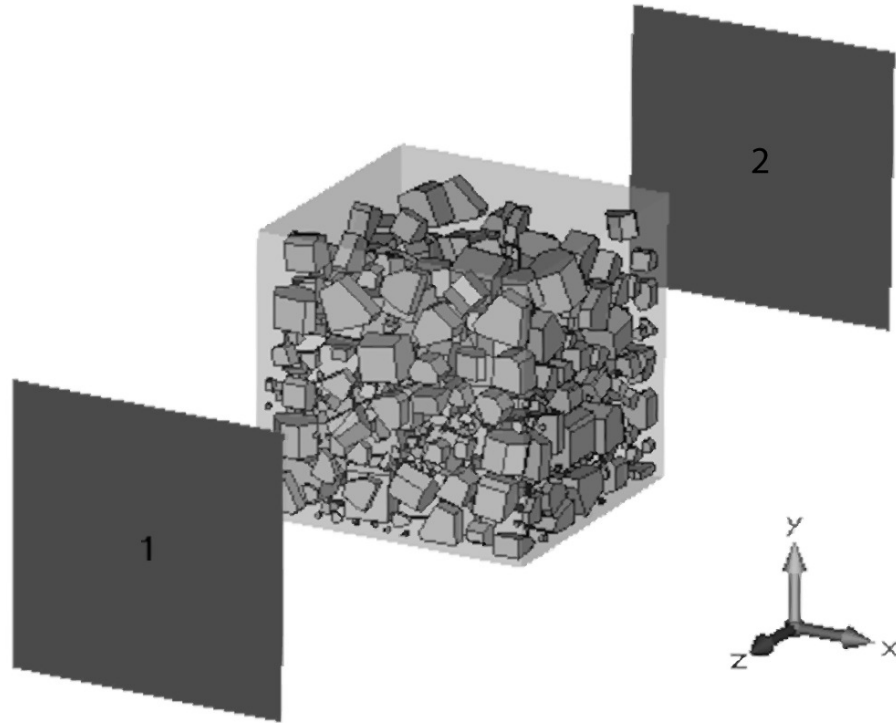


Figure 4.5: The same mixture from Figure 4.3 with waveguide excitation ports after it has been imported into CST Microwave Studio for EM simulation.

be used to study how EM energy behaves and localizes in time when traveling through these complex irregular mixtures.

#### 4.4.2 Localization of Electromagnetic Energy

In CST, the irregular crystals are given a relative permittivity of 28 surrounded by matrix material with a relative permittivity of 1, so that the permittivity contrast between the crystals and the surrounding material is high. Following EM simulation the near-maximum electric energy density obtained for the structure in Figure 4.4 is shown in Figure 4.6, and for the structure in Figure 4.5 in Figure 4.7. Both densities are at the specific time of 44 ps. In Figure 4.6, the electric field is polarized along the  $x$  axis and the EM wave propagates in the positive  $z$  direction (down). In Figure 4.7, the electric field is polarized along the  $x$  axis and propagation is in the negative  $z$  direction (up).

The combination of crystals in Figure 4.6 is different than the combination of crystals in Figure 4.7, since the process of creating, scaling, and combining the crystals is performed independently. So, EM energy travels through a different combination of crystals with each EM simulation run and both structures show high electric energy density. Localization occurring on the edges and corners of the crystals is present for both Figure 4.6 and Figure 4.7, as has been presented previously for crystals with a fractal shape [45].

As detailed in this section, an automated creation method of irregular crystal based composites using the Bullet physics library has been used to study EM propagation through complex mixtures. Electric energy was found to localize on several of these irregular crystals. While it would be an arduous task to create each crystal individually by hand, the procedure described allows many irregular crystals to combine in close proximity with each other. Complex structures can therefore be created in a reasonable

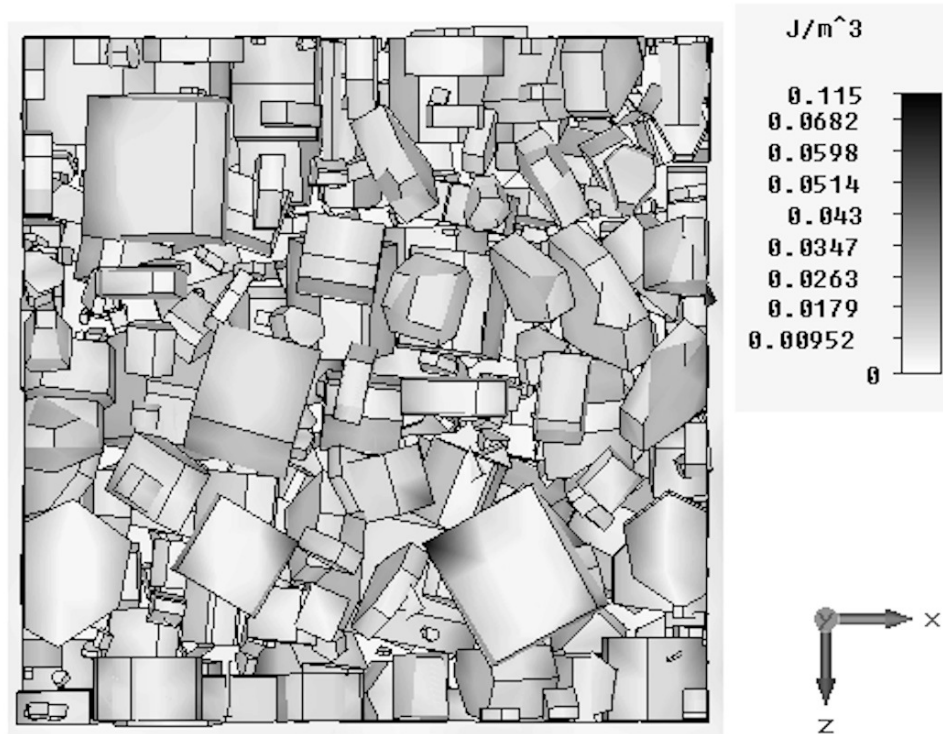


Figure 4.6: Mixture from Figure 4.4 showing high energy density on crystal corners and edges.

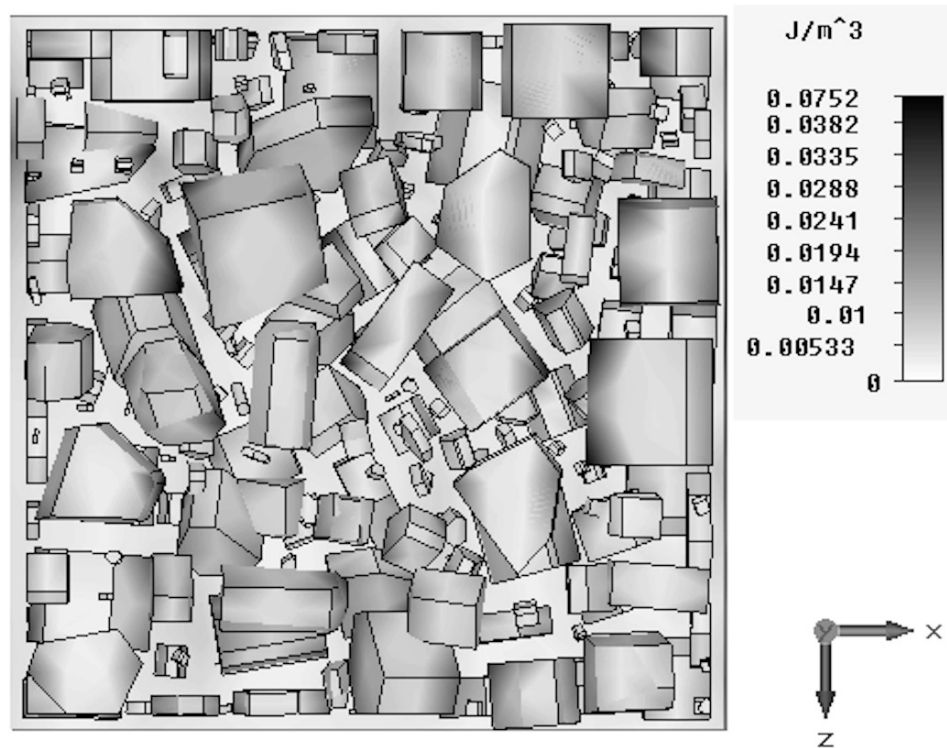


Figure 4.7: Mixture from Figure 4.5 showing high energy density on corners and edges for a different irregular mixture.

amount of time. Once the complex mixtures are formed, they can then be imported into other programs for further analysis.

## 4.5 Multiple Crystal Mixtures

Now that a process to establish complex combinations of irregular crystals has been established, mixtures involving many irregular crystals are created within CST before their EM properties are defined. In this section the effective permittivity of various two-component mixtures is derived. The mixtures have variously shaped crystal inclusions having first low and then high permittivity contrast with the embedding matrix. The mixtures involving many irregular and cube-shaped crystals created in the CST Microwave Studio environment were defined using an automatic procedure based on computer gaming software [60]. In particular, a computer game was created in which crystals (the inclusions) were poured into a box and the physics engine of the game [11] modeled the jostling and bouncing of the crystals as they packed under gravity.

### 4.5.1 Crystal Structures in CST Microwave Studio

The irregular crystals used as inclusions have a maximum size of 0.19 mm as used in [56]. A scaling factor in the range of 0.1 to 1 (and so the crystal sizes are much smaller than a wavelength at 50 GHz) was then used to randomly assign sizes to each crystal. The different scaling factors for each crystal create a structure with an array of crystal sizes but each crystal has the same shape. An example of a complex mixture with irregularly shaped crystal inclusions in the CST Microwave Studio environment is given in Figure 4.8. Additional mixtures were created still exhibiting a disordered arrangement of crystals, but this time with crystals shaped as cubes. An example of such a structure is shown

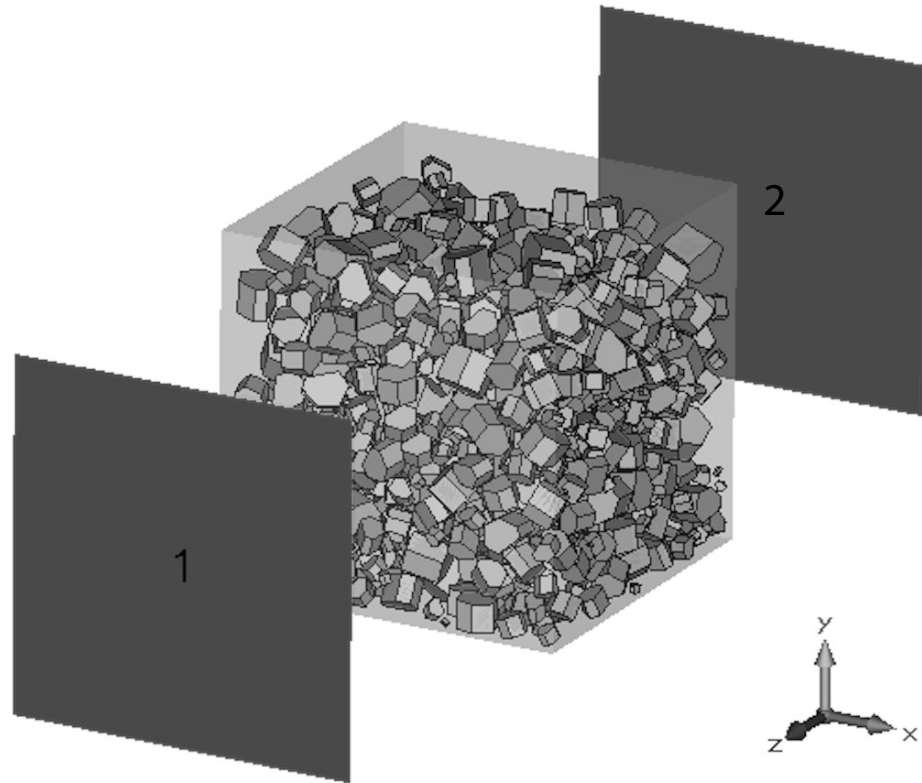


Figure 4.8: A total of 978 irregularly shaped inclusion crystals inside of a block (with side length of 1.37 mm) in a TEM simulation environment. The volume fraction of the inclusions is 27.5%.



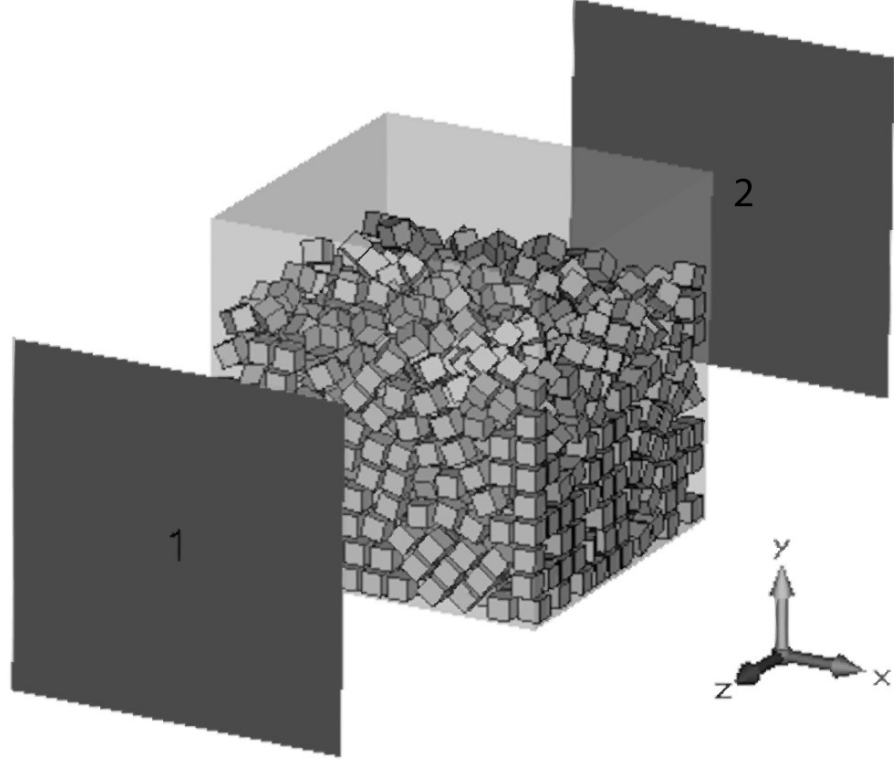


Figure 4.9: A total of 1,144 disordered cube inclusion crystals (each with side length of 0.085 mm) inside of a vacuum outer block (with side length of 1.37 mm). The volume fraction of inclusions is 27.5%.

in Figure 4.9. In both Figure 4.8 and Figure 4.9 none of the crystals are touching (a separation that can be controlled) and the crystals are surrounded by matrix material with a relative permittivity of 1.

EM propagation through the materials was modeled by placing the structures into a parallel plate transverse EM (TEM) environment [45], [56]. Waveguide excitation Ports 1 and 2 are defined on the propagation axis, the  $z$  axis in Figure 4.8 and Figure 4.9, and perfectly matched layer (PML) boundary conditions at the  $x$ - $y$  boundaries. This eliminated reflections from the boundary planes back into the TEM structure. With the crystal structure fixed, but with the boundary conditions changed appropriately,

propagation in the  $x$  and  $y$  directions were also analyzed. To obtain the  $S$ -parameters to be used in Equation 4.6 and Equation 4.7, measurements were de-embedded to the surface of the cubes in Figure 4.8 and Figure 4.9. Effective permittivity was then determined using Equation 4.8 and a Gaussian pulse excitation signal with frequency content up to 50 GHz, as in [56].

### 4.5.2 Low Permittivity Inclusions

First, irregularly and cube shaped inclusions of mica-like crystals having low relative permittivity were considered to establish a lower permittivity contrast scenario between matrix and inclusions. Specifically, mica has a relative permittivity of 5.4 and a  $\tan \delta$  of 0.0006 measured at 1 GHz [55]. Propagation was analyzed for each orthogonal propagation axis, representing  $E_x$ ,  $E_y$ , and  $E_z$  polarizations. These results were then averaged to obtain a single effective permittivity (as described in [40], [41], [44], [56]). Results of effective permittivity at 1 GHz are compared to the Maxwell Garnett and Bruggeman mixing theories and the Wiener bounds in Figure 4.10.

Figure 4.10 indicates that the simulated effective permittivities for the low permittivity contrast situation are close to the results predicted by Bruggeman up to a 40% volume fraction. (This volume fraction is approximately the limit of what can be obtained using irregularly shaped crystals of various sizes [60].) The simulated effective permittivities for the cube crystals and the irregularly shaped crystals at the same volume fraction differ by less than 0.5%. This indicates that, with low permittivity contrast, the effective permittivity of mixtures with many inclusions in a disordered arrangement has very little dependence on inclusion shape.

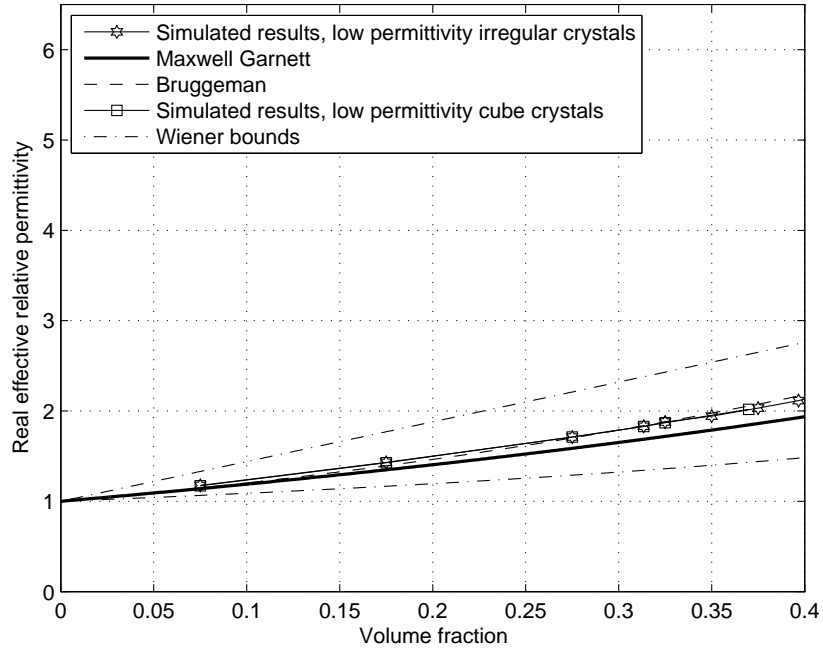


Figure 4.10: Plots of real effective relative permittivity,  $\Re(\epsilon_{\text{eff}})$ , versus various filling factors for low permittivity irregular and cube inclusion crystals along with various mixing theories.

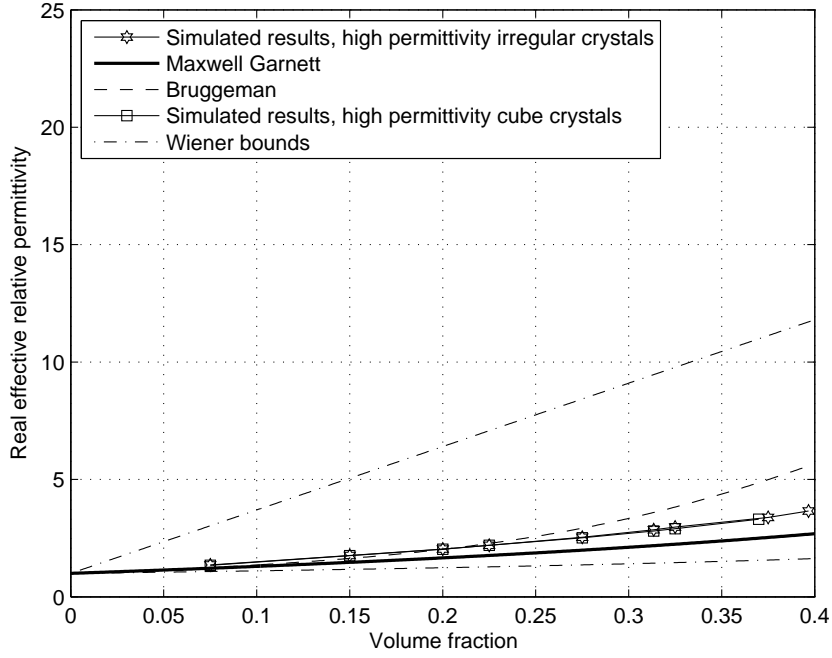


Figure 4.11: Plots of real effective relative permittivity,  $\Re(\epsilon_{\text{eff}})$ , as a function of filling factor for high permittivity irregular and cube inclusion crystals along with various mixing theories.

### 4.5.3 High Permittivity Inclusions

The above simulations were repeated with the same structures, but this time with inclusion crystals of a higher permittivity yielding a higher permittivity contrast with the matrix material. To represent zirconia-like inclusions the crystals now have a relative permittivity of 28 with a  $\tan \delta$  of 0.0009 taken at 1 GHz [55], [56]. Results of effective permittivity at 1 GHz for irregularly shaped and cube inclusions are given in Figure 4.11.

In Figure 4.11 the simulated results fall within the Wiener bounds as expected. The effective permittivities for the irregular inclusions and cube inclusions for this high contrast situation also fall between the results predicted by Maxwell Garnett and Bruggeman

and are close to each other. Numerically, of the eight simulated volume fractions for the mixtures with cube inclusions (as can be seen in Figure 4.11), six differ from the irregular inclusion results on average by 1% or less. The greatest percent difference is 2.5% (with an absolute difference in effective permittivity of approximately 0.07 occurring at 32.5% volume fraction). Figure 4.11 shows that even with a high permittivity contrast (here 28 to 1), the effective permittivity of composite mixtures with hundreds of disordered crystals still has very little dependence on inclusion shape. Earlier research [38], [40], [45] has shown significant differences in effective permittivity between inclusions of different shapes for single-inclusion mixtures. Also, there was no significant convergence in the effective permittivity results when up to eight of each type of inclusion were analyzed [38].

## 4.6 Overall Inclusion Structure and Permittivity

This section explores in greater detail how the overall arrangement of inclusions influences the individual extracted effective permittivity components (i.e.,  $\epsilon_{\text{eff},x}$ ,  $\epsilon_{\text{eff},y}$ , and  $\epsilon_{\text{eff},z}$  components in the  $x$ ,  $y$ , and  $z$  directions respectively) of a mixture.

### 4.6.1 High Permittivity Inclusions

The scenarios that lead to the maximum and minimum possible effective permittivity, as described by the Wiener bounds, are when the inclusion material has the shape of a plate [36]. For example, a structure having an effective permittivity corresponding to the upper Wiener bound is given in Figure 4.12.

In Figure 4.12, the side length of the outer box is 0.91 mm and the thickness of the plate in the  $z$  direction is 0.10 mm, giving a volume fraction of 11.0%. The Wiener bounds

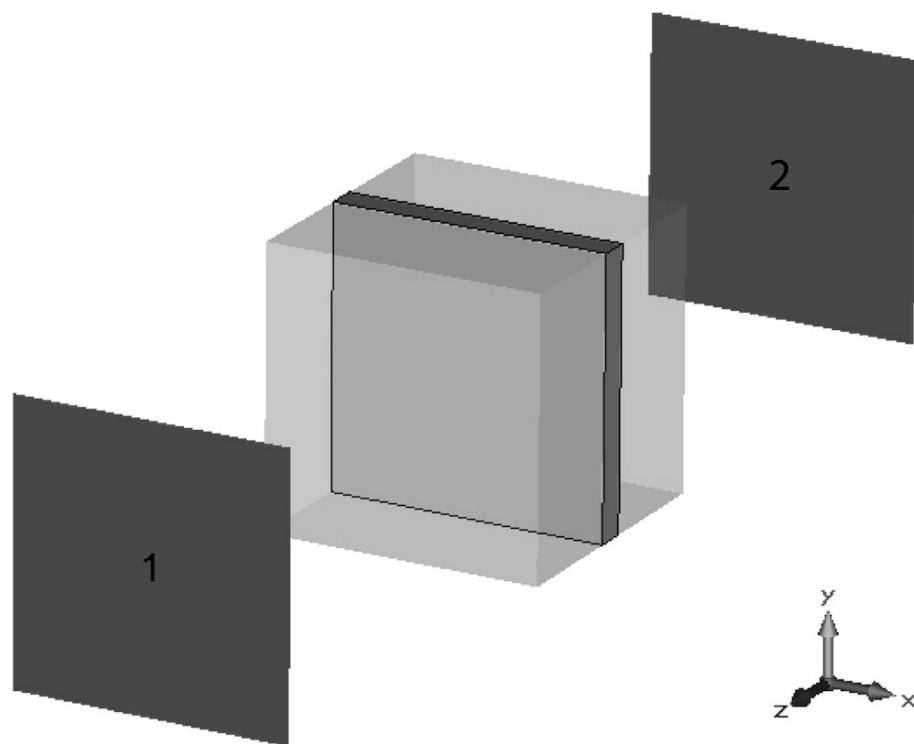


Figure 4.12: Structure showing a high permittivity inclusion arranged as a plate in vacuum with 11.0% volume fraction.

from Equation 4.4 and Equation 4.5 can be used to find the maximum and minimum effective permittivity possible. For the structure in Figure 4.12, these bounds are found to be 3.97 for the maximum  $\Re(\epsilon_{\text{eff}})$  and 1.12, changing the propagation direction, for the minimum  $\Re(\epsilon_{\text{eff}})$ .

These results will now be compared to the simulated effective permittivities. For the structure in Figure 4.12 the extracted effective permittivity depends on the axis of the electric field polarization. The structure in Figure 4.12 has the same electrical properties for  $x$ - and  $y$ -directed electric fields. For  $x$  and  $y$  polarization  $\Re(\epsilon_{\text{eff}})$  from simulation was found to be identical, i.e. 3.97. Notably, this corresponds to the maximum Wiener bound. For  $z$ -directed electric field,  $\Re(\epsilon_{\text{eff}})$  from simulation was found to be 1.13, nearly identical to the minimum Wiener bound.

So, as described in [36], these results confirm that the maximum effective permittivity at a given volume fraction occurs when the largest face of the inclusion plate is parallel to the electrical polarization of the TEM field. The minimum effective permittivity occurs when the largest face of the inclusion plate is perpendicular to the electrical polarization of the TEM field.

### 4.6.2 Relationship to Cross-Sectional Area

In an effort to relate the arrangement of the plate in Figure 4.12 to the maximum or minimum effective permittivity, the cross-sectional areas of the inclusion from Figure 4.12 are studied. Analyzing Figure 4.12, the maximum effective permittivity occurs when the inclusion has the minimum possible cross-sectional area normal to the direction of the electric field polarization. In this scenario, the narrow edge of the plate is ‘seen’ first by the electric field. Conversely, the minimum effective permittivity occurs when the inclusion

has the maximum possible cross-sectional area normal to the electric field polarization direction. Here, the wide face of the plate is presented to the incident electric field. So, this suggests that, for an inclusion shaped as a plate, there is an inverse relationship between the presented cross-sectional area of the inclusion and the effective permittivity of the mixture. This conclusion is consistent with [56] where a similar inverse relationship between effective permittivity and cross-sectional area was developed for a single arbitrarily shaped inclusion crystal.

To investigate the cross-sectional area relationship for structures containing many inclusions, a mixture containing irregular crystals with a 15% volume fraction, as shown in Figure 4.13, and a mixture containing cube crystals also with a 15% volume fraction, as shown in Figure 4.14, were considered. Cross-sectional area was calculated using rays cast along the appropriate axis using the Bullet physics library [11]. For example, to determine the cross-sectional area presented by crystals from the perspective of the  $x$  axis, the  $y$ - $z$  face of the outer box is divided into an  $N \times N$  grid (here  $N = 500$ ). For every point on the grid, a ray is cast perpendicularly to the  $y$ - $z$  face (in the  $x$  direction) from one side of the outer box to the other. If the ray hits a crystal, a hit is recorded. The cross-sectional area of the crystals,  $A_{\text{crystals}}$ , is then defined as:

$$A_{\text{crystals}} = MA_{\text{cell}}, \quad (4.9)$$

where  $M$  is the number of hits and  $A_{\text{cell}}$  is the area of one grid cell. The cross-sectional area fraction,  $A_w$ , ( $w=x, y$  or  $z$ ) is further defined for a given axis perspective (the  $x$  direction is used as an example here) as:

$$A_x = \frac{A_{\text{crystals}}}{A_{\text{total}}}, \quad (4.10)$$



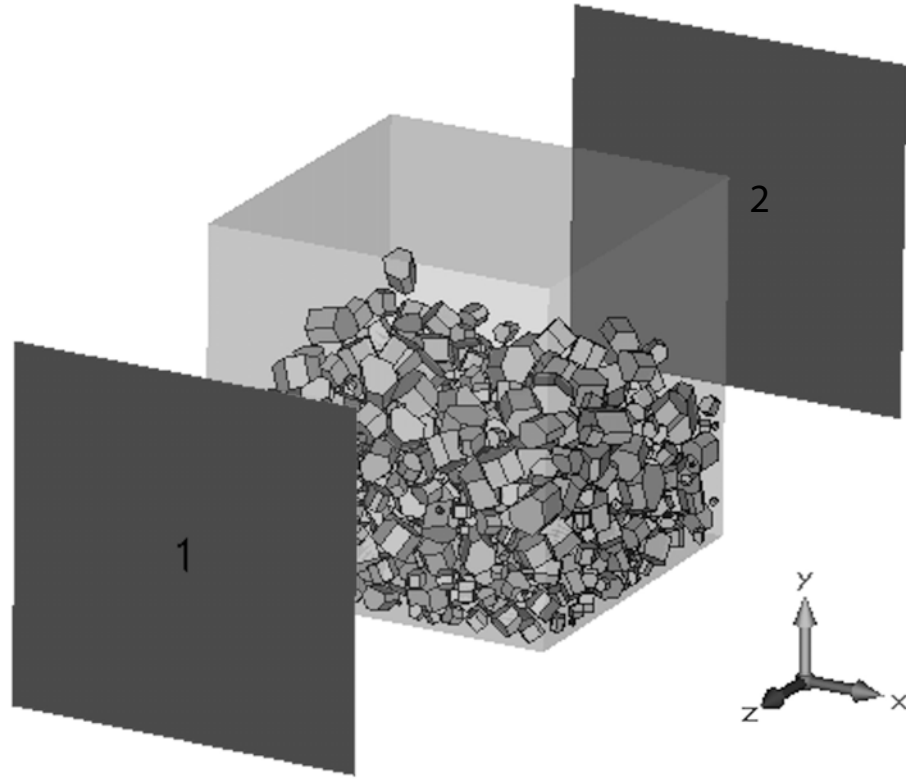


Figure 4.13: Structure showing 894 high permittivity irregular inclusions inside a vacuum outer block (with side length 1.46 mm). The volume fraction of inclusions is 15%.

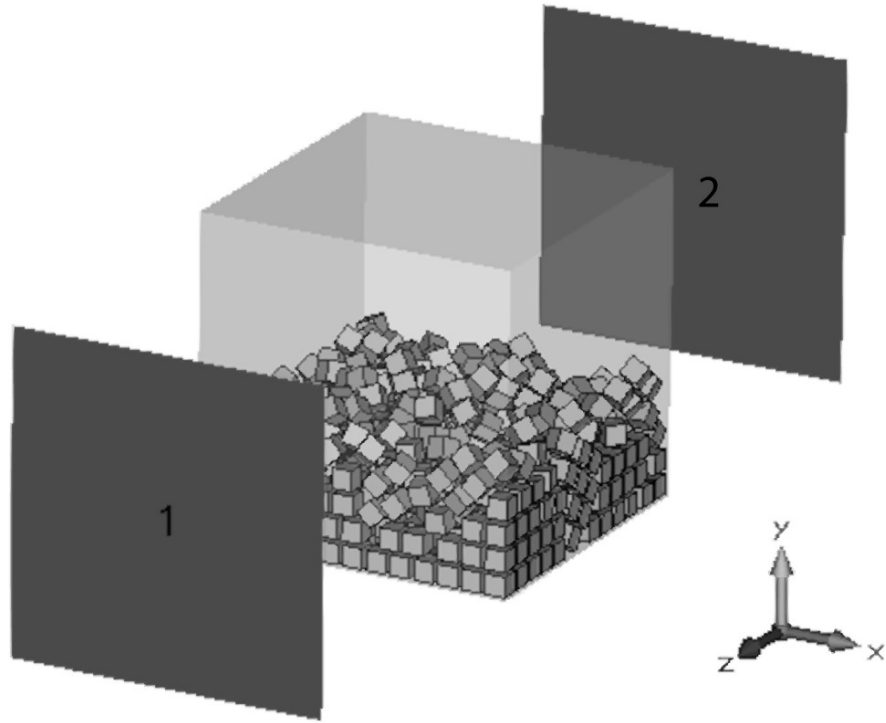


Figure 4.14: Structure showing 624 high permittivity cube inclusions (each with side length 0.085 mm) inside a vacuum outer block (with side length 1.37 mm). The volume fraction of inclusions is 15%.

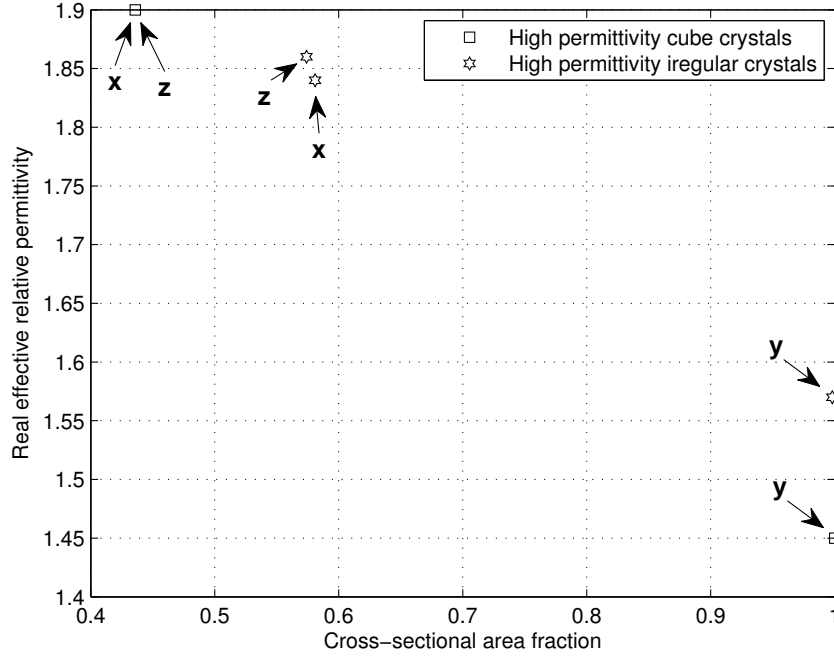


Figure 4.15: Real effective permittivity,  $\Re(\epsilon_{\text{eff}})$ , plotted as a function of cross-sectional area fraction,  $A_w$ . The volume fraction of inclusions is 15%. The letters near the data points indicate the electric field polarization axis for each type of crystal as well as the cross-sectional area fraction direction.

where  $A_{\text{total}}$  is the total area of the outer box. The cross-sectional area of crystals and cross-sectional area fraction are calculated in this manner for the  $x$ ,  $y$ , and  $z$  directions independently.

With high permittivity inclusions at 15% volume fraction, the effective permittivities and corresponding cross-sectional area fractions,  $A_w$ , for each axis are given in Figure 4.15. Comparing all cases presented in Figure 4.15, the highest cross-sectional area fraction value corresponds to the lowest effective permittivity component and vice versa, suggesting an inverse relationship.

The differences in magnitude of the effective permittivity among the polarizations as

presented in Figure 4.15 can be qualitatively related to the cross-sectional area fraction differences by analyzing the mixtures in Figure 4.13 and Figure 4.14. Based on the way the irregular structures are created using the Bullet physics library, the crystals fall from above (with respect to the  $y$  axis) and fall to the bottom of the outer box before settling. The crystals therefore become tightly packed on the bottom of the box as can be seen in Figure 4.13 and Figure 4.14.

This means that from the perspective of the  $y$  axis, the inclusion crystals have a high cross-sectional area fraction,  $A_y$ . From the perspective of the  $x$  and  $z$  axes, the cross-sectional areas of the inclusions are relatively small, and so  $A_x$  and  $A_z$  are smaller. This can also be seen in Figure 4.13 and Figure 4.14, where from the perspective of the  $x$  and  $z$  axes the upper part of the box is the background material (with relative permittivity of 1).

Relating this to the permittivity values, a high  $A_w$  from the perspective of the TEM electric field polarization axis,  $w$ , leads to a low effective permittivity (e.g. here  $A_y$  is high and the effective relative permittivity component in the  $y$  direction,  $\epsilon_{\text{eff},y}$ , is low) while the other polarizations have lower  $A_w$  and higher effective permittivity. This is the same inverse relationship demonstrated by the plate of Figure 4.12. Since the crystals do not form a complete plate in any direction, the maximum or minimum possible permittivity values as given by the Wiener bounds are not reached. However, based on the way the crystals are packed in the box in Figure 4.13 and Figure 4.14, they are quite dense and close to the sides of the box. In this situation it can be said that the inclusions exhibit plate-like behavior. This can be seen through the sharing of an inverse relationship between cross-sectional area fraction and effective permittivity for both the plate and the densely packed crystals. This correspondence is seen for all of the simulation results for low and high permittivity inclusions presented in Figure 4.10 and Figure 4.11 respectively.

Since all of the simulations covering the various volume fractions in Figure 4.10 and Figure 4.11 were created in the same manner (the crystals falling into the box along the  $y$  axis and then settling)  $A_w$  for all simulations was greatest looking along the  $y$  axis (i.e.  $w=y$ ), and  $E_y$  polarization always yielded the smallest effective permittivity component.

## 4.7 Energy Localization

The other important phenomenon that characterizes the electrical response to a pulsed microwave signal is energy localization, in particular the concentration of electric energy in a nonmagnetic composite. Composites respond to temporal energy localization by delaminating and changing chemical phase. Also, identifying energy localization can be used as a diagnostic tool. Many of these effects respond over a short time interval so that it is the transient time-domain EM response that is more important than the steady-state response provided by a frequency-domain EM analysis. Energy has been found to localize on the edges and corners of single inclusions [45], [56]. This section explores localization phenomena taken using time-domain monitors for mixtures containing many crystals close together, highlighting phenomena neglected by steady-state analyses.

### 4.7.1 High Permittivity Inclusions

First, electric energy density is plotted for a complex mixture with 32.5% volume fraction. An example showing near-maximum electric energy density in a high permittivity (with a real relative permittivity of 28) inclusion mixture for electric field polarized along the  $x$  axis and positive  $z$  propagation direction is given in Figure 4.16. The excitation signal is a Gaussian pulse with frequency content up to 50 GHz. The side length of the outer box in Figure 4.16 is 1.37 mm. The bottom right black circle shown in Figure 4.16 has a

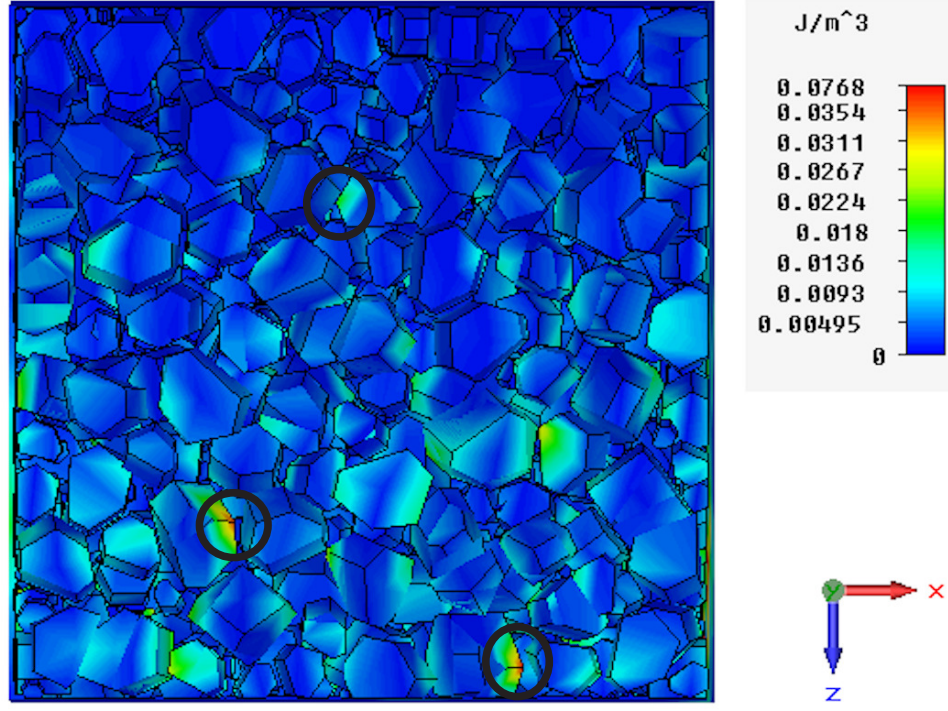


Figure 4.16: Near-maximum electric energy density showing localization at inclusion corners and edges, with highest localization in the bottom two circles. The electric field is polarized along the  $x$  axis and the propagation direction is positive  $z$  (down). The volume fraction is 32.5%.

diameter of approximately 0.12 mm. For reference, in vacuum the wavelength at 1 GHz is 300 mm and at 50 GHz is 6 mm. With  $\epsilon_r = 28$ , the wavelength at 1 GHz is 56.69 mm and at 50 GHz is 1.13 mm. From Figure 4.11, the effective permittivity for this composite was calculated as 2.97. With a relative permittivity of 2.97, the wavelength at 1 GHz is 174.08 mm and at 50 GHz is 3.48 mm. Comparing these sizes, the energy localization shown in Figure 4.16 occurs on the order of  $0.01\lambda$  or less, a fine resolution in terms of wavelength.

The near-maximum energy density is shown in Figure 4.16 at 48.1 ps. The energy localizes to the greatest extent on the edges and corners of the irregular inclusions shown

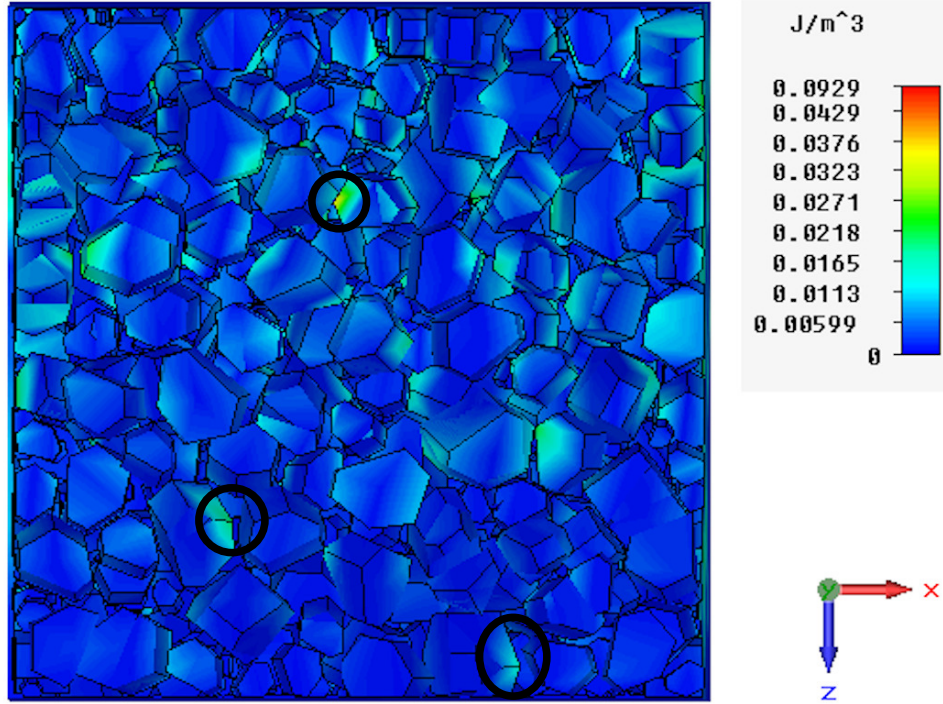


Figure 4.17: Electric energy density with the same conditions as in Figure 4.16, but with propagation in the reverse direction (up). The strong localization from Figure 4.16 is not seen in the bottom two circles. Instead, there is higher localization in the top circle.

inside the bottom two circles in Figure 4.16 after the signal has passed through many other inclusions. Propagation in the reverse direction, along the negative  $z$  axis (up), results in the near-maximum electric energy density scenario in Figure 4.17. This image is taken at the same time and plane as the structure shown in Figure 4.16. The only difference in simulation conditions between Figure 4.16 and Figure 4.17 is an opposite direction of propagation.

The crystal indicated by the upper circle in Figure 4.17 shows greater energy density compared to the same location in Figure 4.16. Conversely, the energy density on the crystals indicated by the bottom two circles is smaller. Comparing Figure 4.16 and Figure 4.17, the electric energy density localizes with different magnitudes depending on the

direction of propagation of the EM signal. At specific locations, indicated by the black circles in Figure 4.16 and Figure 4.17, the magnitude of the energy density at the edges and corners is higher when the signal has traveled through more scatterers.

As an additional test, the Gaussian pulse duration was extended, with the frequency content ranging from 0 to 25 GHz. The energy was seen to localize in the same locations with the same localization behavior as for the 0 to 50 GHz bandwidth excitation used in Figure 4.16 and Figure 4.17. Halving the frequency range allowed the Gaussian pulse duration to double from 71 ps to 142 ps. Comparing the peak localization magnitudes with Port 2 excitation, for the 0 to 50 GHz excitation the maximum monitored energy density was  $0.0768 \text{ J/m}^3$ , while for the longer 0 to 25 GHz excitation the maximum was  $0.0992 \text{ J/m}^3$ . Overall, this result suggests that a longer excitation time can result in a higher peak localization magnitude.

For the situations represented in Figure 4.16 and Figure 4.17, the peak input power is 1 W. This is input over the entire port face, which has a side length of 1.37 mm. Assuming this 1 W is input for the 0 to 50 GHz Gaussian pulse duration, 71 ps, means that the total input power is  $7.1 \times 10^{-11} \text{ J}$ . In order to find an energy density entering the structure, it is necessary to find the wavelength using the calculated effective permittivity of 2.97 so that the effective group velocity is  $1.74 \times 10^8 \text{ m/s}$ . Since the Gaussian pulse duration is 71 ps, the length of the pulse in the medium is 0.012 m. Multiplying this by the input port area gives an input volume of  $2.25 \times 10^{-8} \text{ m}^3$ . Then, the energy density entering is the input power divided by this volume, i.e.  $0.0032 \text{ J/m}^3$ . Comparing this value to the peak energy density of  $0.0768 \text{ J/m}^3$  in Figure 4.16, this means that here there is an energy density increase of 24 times represented by this energy localization.

The physical interpretation is that the energy localization maximum occurs when signals following multiple scattering paths coalesce at the same time and position. Such



a hotspot is unlikely to occur at the surface of a composite but within the material after multiple scattering events have occurred but before the signal has been significantly attenuated.

### 4.7.2 Electric Fields for Irregular Inclusions

To gain a better understanding of the localization behavior occurring in the circles in Figure 4.16 and Figure 4.17, simulation probes were inserted to measure the electric field magnitudes over the course of the simulation. The electric fields at the location indicated by the bottom right circles in Figure 4.16 and Figure 4.17 are given in Figure 4.18, at the bottom left circles are given in Figure 4.19, and at the top circles are given in Figure 4.20. In Figure 4.18 through Figure 4.20, the electric field localizes at specific crystal corners and edges to a greater amount when the EM signal has previously traveled through more scatterers. From Figure 4.18 and Figure 4.19, peak energy localization at the bottom crystals occurs after the signal has traveled from top to bottom. The energy density for this positive  $z$  propagation direction is shown in Figure 4.16 at the time indicated in Figure 4.18 and Figure 4.19, i.e. 48.1 ps. From Figure 4.20, peak localization at the top crystal occurs after the signal travels from bottom to top, with energy density for this negative  $z$  propagation direction at the time indicated in Figure 4.20, 48.1 ps, given in Figure 4.17. The electric field probes from Figure 4.18 through Figure 4.20 confirm the results of energy density from Figure 4.16 and Figure 4.17 that traveling through a greater number of inclusions increases localization magnitude at a specific location. Next, this behavior is studied for a simpler case of identical inclusions placed on an organized grid.

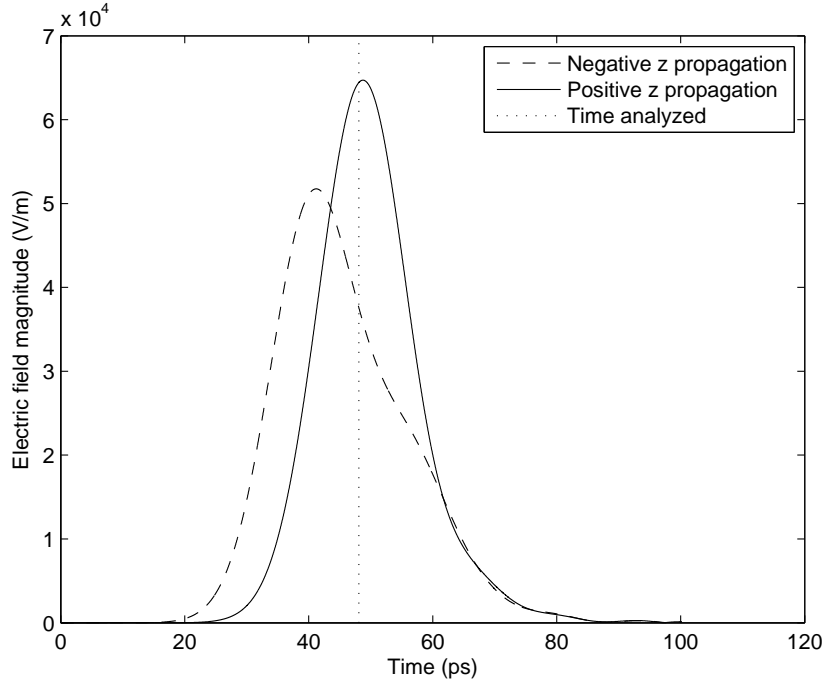


Figure 4.18: Comparison of the electric field at the crystal corner indicated by the bottom right circle in Figure 4.16 and Figure 4.17 with propagation direction. At 48.1 ps there is a significant difference in the electric field and electric energy density depending on propagation direction. Higher peak localization is seen with the positive propagation direction (down) when the EM signal has traveled through more of the irregular surrounding material.

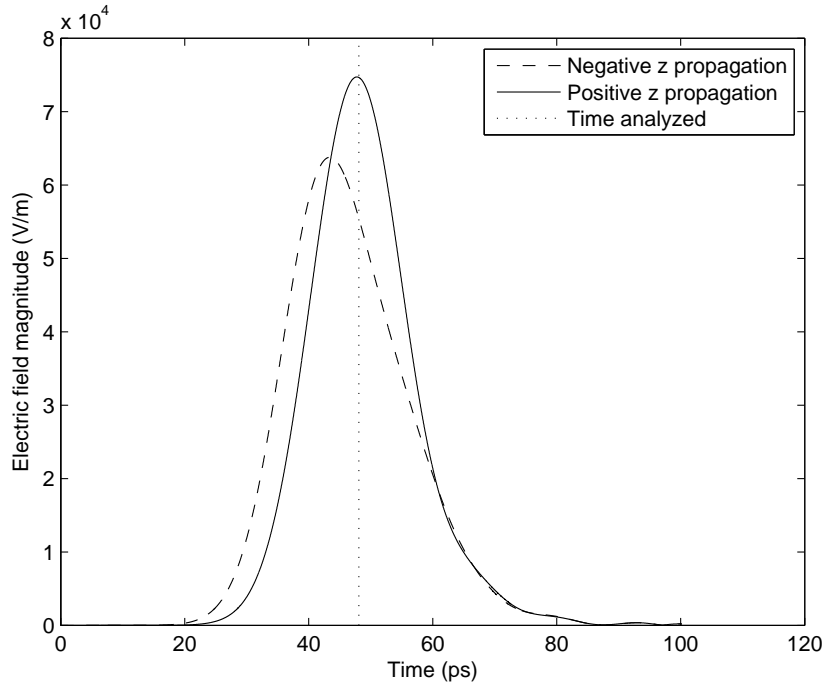


Figure 4.19: Comparison of the electric field at the crystal corner indicated by the bottom left circle in Figure 4.16 and Figure 4.17 with propagation direction. Higher peak localization is seen at 48.1 ps with the positive propagation direction (down) when the EM signal has traveled through more of the irregular surrounding material.

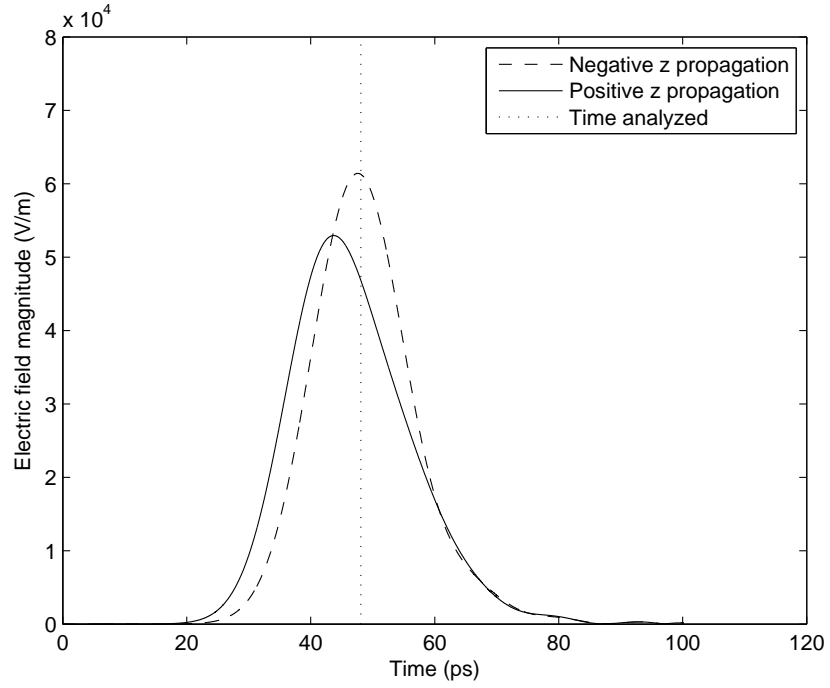


Figure 4.20: Comparison of electric field for the top circle in Figure 4.16 and Figure 4.17 with propagation direction. At 48.1 ps there is a significant difference in the electric field and electric energy density depending on propagation direction. Higher peak localization is seen with the negative propagation direction (up) when the EM signal has traveled through more of the irregular surrounding material.

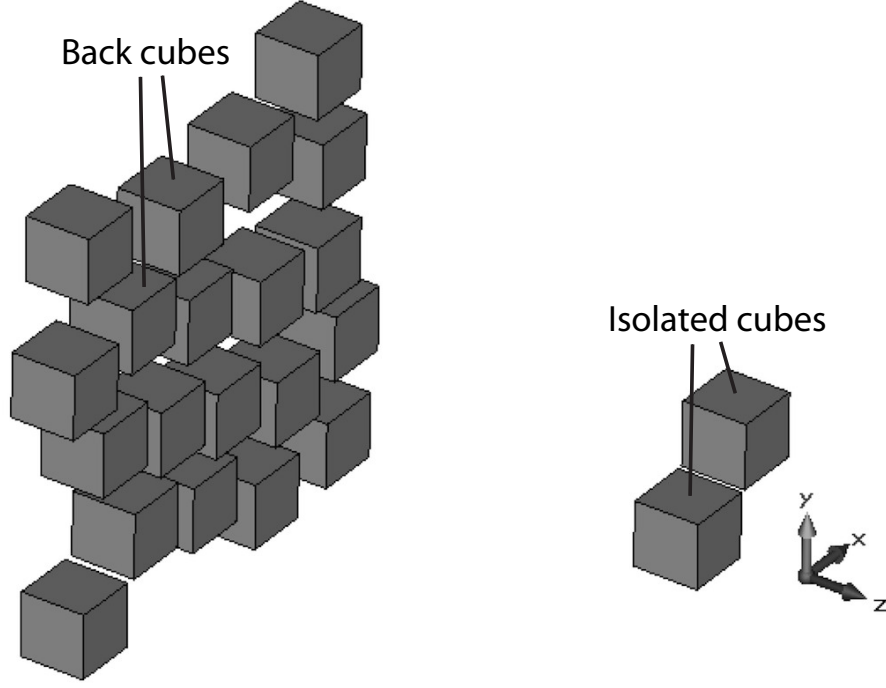


Figure 4.21: Cube-shaped inclusions arranged in two planes. On the right are the isolated cubes and on the left are the back cubes.

### 4.7.3 Behavior for Cube-shaped Inclusions

From Section 4.7.2, the electric field localization magnitude was seen to increase when the EM signal traveled through a greater number of scatterers. This section studies electric field localization for a less complicated mixture with high permittivity cube-shaped inclusions on a regular three-dimensional grid. The aim of this study is to determine if a simpler simulation environment yields similar energy localization results. First, two parallel layers of cubes in the  $x$ - $y$  plane are created as shown in Figure 4.21. Each cube has a side length of 0.1 mm. The left  $x$ - $y$  plane in Figure 4.21 has 20 cubes placed randomly within the plane, two of which are referred to as the back cubes. After the cubes have been placed in the plane, the back cubes (the two closest cubes in this plane) are then

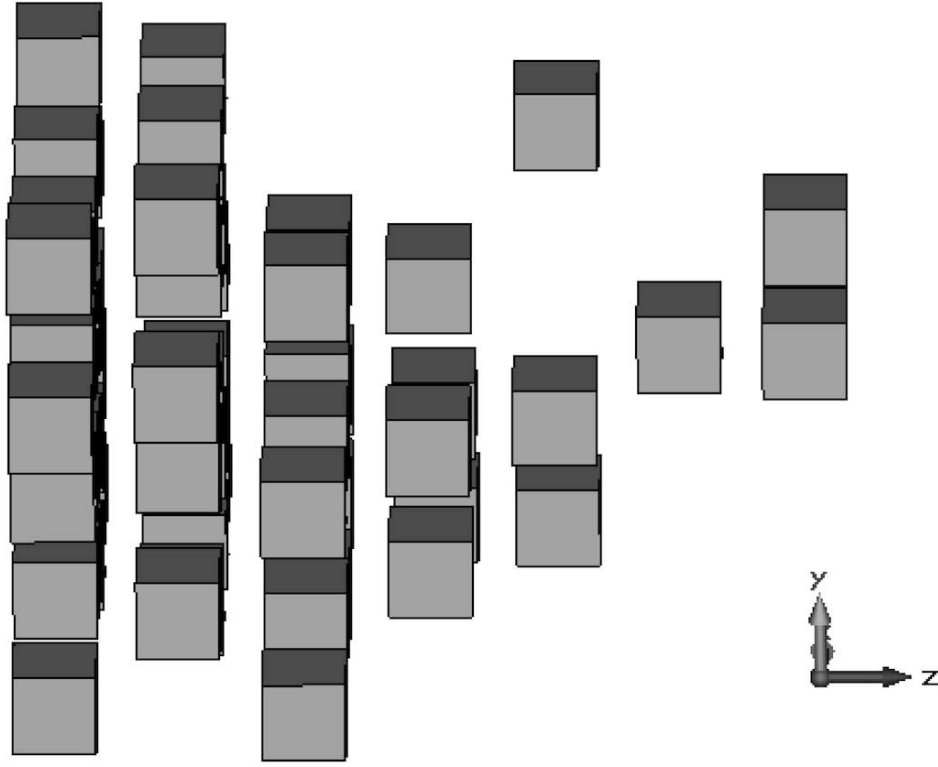


Figure 4.22: Layers of cube-shaped inclusions are added between the layers in Figure 4.21 with an increasing number of inclusions in each layer.

shifted in the positive  $z$  direction with the same  $x$  and  $y$  coordinates in order to maintain the same distance and orientation between the cubes but to isolate them in their own  $x$ - $y$  plane. This pair of cubes, to be referred to as the isolated cubes, are shown on the right side of Figure 4.21. The two cubes are isolated in order to study the influence of surrounding cubes within a plane on energy localization.

Next, additional cubes are placed in planes evenly spaced between those shown in Figure 4.21. The resulting structure is shown in Figure 4.22. The distance between cubes in two adjacent  $x$ - $y$  planes in Figure 4.22 is 0.05 mm and none of the cubes are touching. Behind the two isolated cubes on the right, going in the negative  $z$  direction (left), the

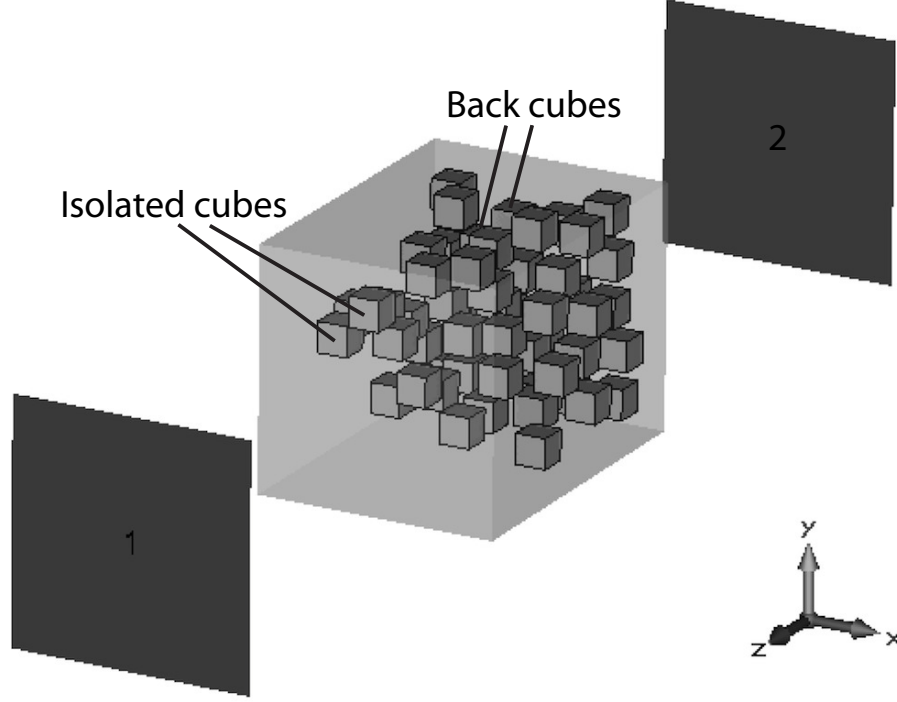


Figure 4.23: The structure in Figure 4.22 (surrounded by vacuum) along with waveguide ports for simulation.

next  $x$ - $y$  plane has 1 cube, then 3, 5, 10, and 15 before the left-most plane with 20 cubes is reached. Adding cubes in this manner gradually increases the number of inclusions between the layers shown in Figure 4.21. The goal is to confirm the hypothesis that EM propagation through more inclusions leads to an increase in the peak hotspot magnitude.

The total structure with all cubes along with the waveguide Ports 1 and 2 is given in Figure 4.23. In Figure 4.23, the isolated cubes from Figure 4.21 and Figure 4.22 are closest to Port 1 and the back cubes are closest to Port 2. The outer box in Figure 4.23 spans 0.8 mm in the  $x$  and  $y$  directions. The two ports are the same distance to the nearest high permittivity cube in either direction, specifically 1.55 mm. The electric field is polarized along the  $x$  axis and  $z$  is the propagation axis. The excitation signal is a 0

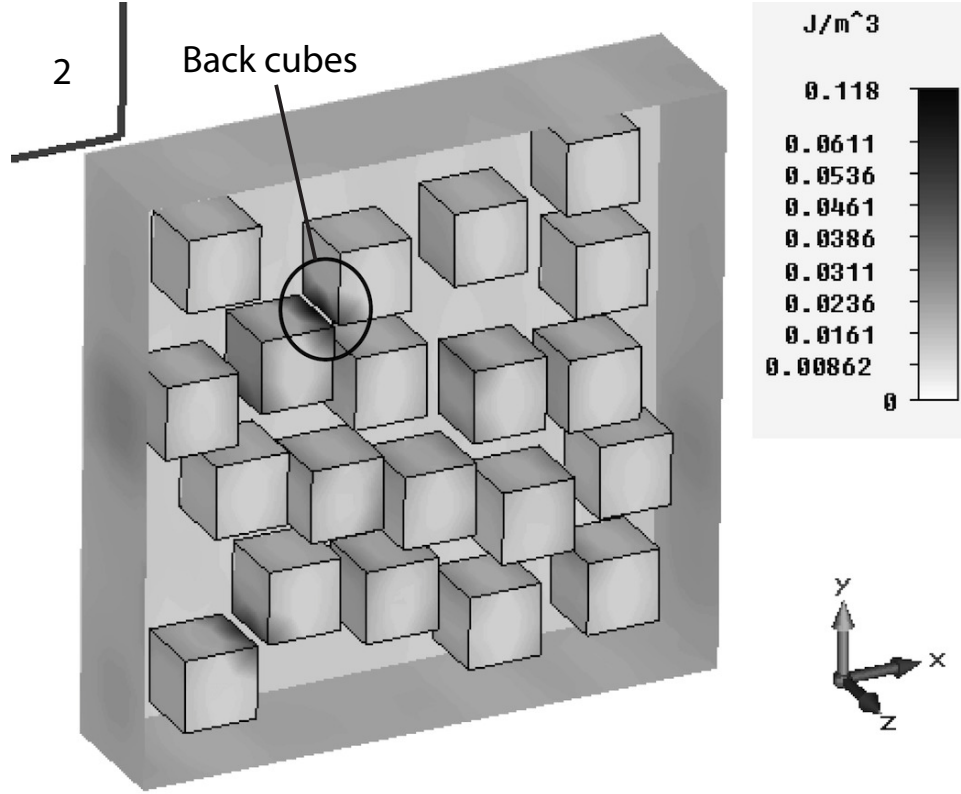


Figure 4.24: Near-peak electric energy density for the back layer of cubes at 44 ps (time of near-maximum energy density) with highest magnitude at the edges and corners of the back cubes as indicated by the black circle. This occurs for Port 1 excitation.

to 50 GHz Gaussian pulse. The near-peak energy density location in the structure from Figure 4.23 is shown in Figure 4.24.

In Figure 4.24, the highest energy density among all the cubes occurs at the edges and corners of the back cubes with Port 1 excitation. Again, localization magnitude is greater after the signal has traveled from Port 1 to Port 2 through a greater number of scatterers. The plane of cubes shown in Figure 4.24 is the back layer with the highest number of cubes (20) closest to Port 2. The back cubes indicated by the black circle in Figure 4.24 have edges and corners closest to each other within that plane, and no edges



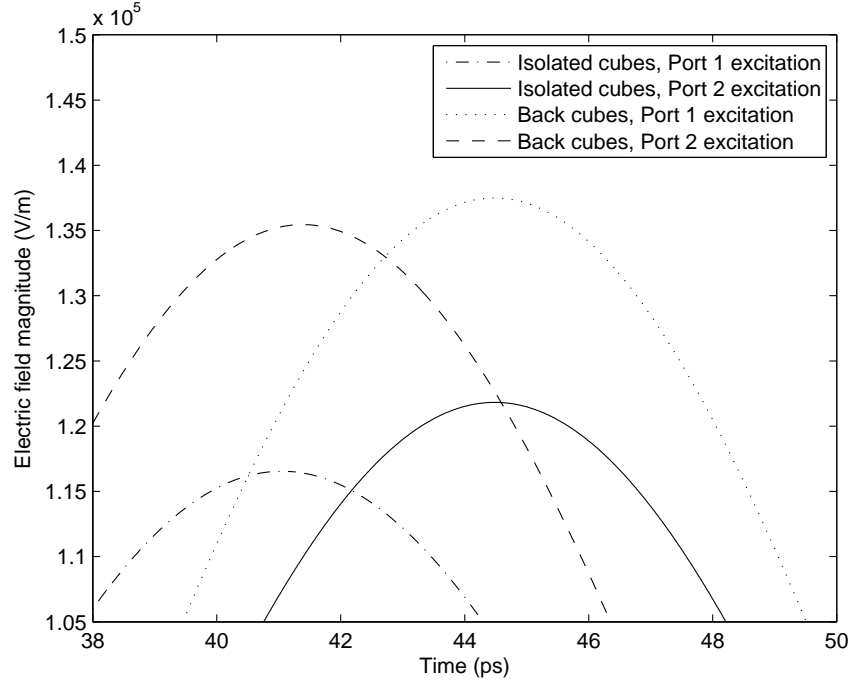


Figure 4.25: Electric field magnitudes for four different locations in the structure in Figure 4.23 as a function of time. Peak localization magnitude is reached for the back cubes with Port 1 excitation after the signal has traveled through other scatterers.

between other adjacent cubes are closer in the entire structure. Overall, adjacent cubes coming closer together also increases temporal energy localization.

Electric field probes can be used to gain an understanding of how the field magnitude changes over time. Probes are utilized to measure the electric field at the edge of one of the back cubes (encompassed by the circle in Figure 4.24) as well as the same relative location but on the isolated pair of cubes closest to Port 1 (those indicated in Figure 4.23). The results from these two probes, each probe measuring electric field with Port 1 and Port 2 excitation independently, are summarized in Figure 4.25. The isolated cubes and back cubes referenced in Figure 4.25 are analyzed because they represent the maximum EM localization within the mixture shown in Figure 4.23. In Figure 4.25, electric field

localization magnitudes are plotted as a function of time. As shown in Figure 4.21, there are two pairs of cubes with the same orientation to each other: the isolated cubes and the back cubes. One pair is surrounded by many other inclusions in the same plane (the back cubes shown in Figure 4.21, in the plane of cubes closest to Port 2 in Figure 4.23, and referenced in Figure 4.25) and the other pair is isolated in a plane by itself (the isolated cubes shown in Figure 4.21, in the plane of cubes closest to Port 1 in Figure 4.23, and referenced in Figure 4.25) to study the impact of surrounding inclusions. The two cubes within a pair are the same distance from each other and differ only in their  $z$  coordinates.

Analyzing Figure 4.25, for the back cubes closely surrounded by other high permittivity cubes, the peak electric field magnitude is higher for both propagation directions (i.e. for Port 1 and Port 2 excitation, representing propagation in the negative and positive  $z$  directions respectively) than for either propagation direction for the isolated cubes in the front. There are more scatterers in the back layer, so the localization magnitude is higher than in the front where in that layer there are few scatterers. In summary, a greater number of scatterers within a layer increases energy localization.

For the back cubes in Figure 4.25 (in the layer closest to Port 2 in Figure 4.23 and Figure 4.24), looking at the differences caused by changing the propagation direction, there is higher localization for Port 1 excitation than for Port 2 excitation. With excitation at Port 1, the signal goes through six layers of scatterers to get to the back layer (each layer can be seen independently in Figure 4.22). Port 2 excitation means that the back layer is the first layer experienced by the signal. Since the EM field has not undergone previous scattering events, the magnitude of localization is lower for this propagation direction. Using the same reasoning as for the back layer, for the isolated cubes in Figure 4.25 (closest to Port 1 in Figure 4.23), Port 2 excitation yields higher localization because the signal travels through more scatterers before reaching the isolated cubes.

Also from Figure 4.25, it is seen that the lowest overall localization magnitude occurs when the isolated cubes (i.e. few cubes in a layer) are the first scatterers encountered by the EM pulse. These are the isolated cubes closest to Port 1 in Figure 4.23 with Port 1 excitation. Conversely, the highest overall localization magnitude occurs for the back cubes closest to Port 2 in Figure 4.23 with Port 1 excitation (at the location encompassed by the circle in Figure 4.24). In this situation there are the most scatterers within the layer and the signal has traveled through the highest number of scatterers to reach this back point close to Port 2.

In [56], energy localization was found on the edges and corners of a single irregular inclusion crystal. This chapter studied energy density behavior for mixtures with many disordered irregular, as well as organized cube, inclusions. As the EM signal travels through more scatterers, the peak energy density has been shown to increase even if the inclusions are small compared to wavelength. These results suggest that a direct relationship exists between the disorder introduced by an increasing number of inclusions and localization magnitude.

## 4.8 Summary

The effective EM properties for mixtures involving many disordered crystals were studied. In particular, the crystal shape was found to have no appreciable impact on effective permittivity or energy localization behavior. The effective permittivity derived from simulations deviates from that calculated using conventional Maxwell Garnett and Bruggeman mixing theories. This departure is especially significant when there is a high permittivity contrast between the inclusions and the embedding matrix. This is so when the inclusions have irregular or regular shapes. For mixtures with hundreds of crystals,

the effect of individual inclusion shape and orientation on effective permittivity apparently averages out. As expected, inclusions in the form of a plate yield either maximum or minimum effective permittivity depending on the cross-section presented to the EM signal. In general a strong inverse relationship was found between the cross-sectional area presented by the inclusions and the effective permittivity of the mixture. While established mixing laws are functions of individual permittivity values and volume fraction, this chapter showed that cross-sectional area is also an important parameter to consider when determining the effective permittivity of mixtures of finite thickness.

Energy was seen to localize within mixtures containing many inclusions. The specific location of EM localization is on edges and corners of adjacent inclusions that are close to each other in the direction of electric field polarization. Temporal maximum energy density occurs only after appreciable scattering has occurred but before the EM signal has been attenuated.

# Chapter 5

## Summary and Future Work

### 5.1 Summary of Research

This dissertation presented an overview of effective permittivity and EM localization behavior for various types of composite mixtures. The complexity of these mixtures was increased throughout the dissertation. In Chapter 3, the examined composites included those with a single cube inclusion, a single irregular inclusion, and many ordered cube inclusions placed on a regular grid. In Chapter 4, the composites were much more complex, and included mixtures with hundreds of regularly- and irregularly-shaped inclusions. The research describing the characterization of composites within this dissertation can be useful for various applications. These include current research areas such as structure demolition and demining, as well as future areas such as the study of Carbon Fiber Reinforced Composites (CFRCs).

In Chapter 3, two-component composites were examined consisting of cube and irregularly-shaped inclusions. Time-domain EM modeling was used to calculate effective permittivities and to examine energy localization behavior for these composites. Both

high and low permittivity contrast situations were used and the components studied included the explosive material HMX.

With irregularly shaped inclusion crystals, effective permittivities were calculated for each of three orthogonal propagation directions ( $x$ ,  $y$ , and  $z$ ). The irregular structures were not symmetric with respect to all polarization directions, and so the effective permittivity showed directional dependency. However, for the same electric field polarization, effective permittivity was independent of forward or backward propagation direction. To calculate effective permittivity, the composites were placed within a TEM environment. This environment was created by setting one pair of opposite faces as electric walls, another as magnetic walls, and the last as open boundaries that eliminated reflections back into the TEM environment.

The first examined situation involved HMX inclusions, representing low permittivity contrast between inclusion and matrix material. In situations of low permittivity contrast, the shape of the inclusion had little impact on effective permittivity up to a volume fraction of 0.45. With this low permittivity contrast, the Maxwell Garnett and Bruggeman mixing theories could be used up to a volume fraction of 0.45 with 1% error. With high permittivity contrast, significant differences were found from the classical mixing rules, Maxwell Garnett and Bruggeman, for volume fractions above 0.05. So, for high filling factors the traditional mixing theories did not accurately predict the effective permittivity of irregularly shaped mixtures with high permittivity contrast between inclusion and surrounding material.

Mixtures with cube inclusions placed on an ordered grid were also examined in Chapter 3. This highly ordered scenario allowed the entire range of volume fractions to be simulated. The effective permittivities for these composites were found to be close to the results predicted by Maxwell Garnett for all volume fractions.

Energy localization behavior was examined with negligible differences found between mirrored and periodic boundary conditions. For both types of boundary conditions, electric energy localized on edges and corners of the irregular inclusion. The specific edges and corners were those closest to the adjacent crystal in the direction of electric field polarization.

Also in Chapter 3, the inclusion crystals were rotated and the orientation of the inclusions with high permittivity contrast impacted the effective permittivity of the composite. First, a cube inclusion at 10% volume fraction was rotated around the  $x$ ,  $y$ , and  $z$  axes independently. With the electric field polarized in the  $x$  direction, effective permittivity was determined for each rotation point. Then, a 20% volume fraction cube was rotated around each axis with the electric field also polarized in the  $x$  direction. Finally, in a more complex scenario, rotation was performed for an irregular inclusion at 20% volume fraction. The irregular inclusion was rotated around the  $x$ ,  $y$ , and  $z$  axes independently and the electric field was polarized in either the  $x$ ,  $y$ , or  $z$  direction. For all of the rotation scenarios, negligible changes in effective permittivity resulted when the inclusion was rotated about the same axis as the electric field polarization. However, variations in effective permittivity resulted from rotations about the other axes.

Plots were also provided showing changes in cross-sectional area fraction as each inclusion was rotated. The variation in the cross-sectional area fraction from the perspective of a given axis was highly correlated to changes in effective permittivity with the electric field polarized along the same axis. If the cross-sectional area fraction changed or remained constant, the effective permittivity also showed the same behavior. An inverse relationship between cross-sectional area fraction and effective permittivity developed when a significant portion of the inclusion crystal approached the outer box, or adjacent inclusions. Differences in effective permittivity from rotation of the inclusion crystal

correspond to a probe moving around a specific compound.

In Chapter 4, the complexity of the examined composites was increased compared to those studied in Chapter 3. EM properties of mixtures were explored further by examining structures with many irregular and cube inclusion crystals in a disordered arrangement. The crystals had both low and high permittivity contrast with the surrounding material. With low permittivity inclusions, the results of effective permittivity were close to the predictions of Bruggeman up to a volume fraction of 40%. For the same volume fraction, the effective permittivities for the irregular and cube inclusion crystal mixtures differed by less than 0.5%. So, with hundreds of disordered inclusion crystals and a relatively low permittivity contrast, the effective permittivity of mixtures had very little dependence on inclusion shape.

Next, the crystals were given a higher relative permittivity. In this situation the effective permittivity results were within the Wiener bounds (as expected) and were also between the results predicted by Maxwell Garnett and Bruggeman up to a volume fraction of 40%. With this high permittivity contrast, a majority of the results between irregular and cube inclusion crystals differed by 1% or less at the same volume fraction. Here, even with a high permittivity contrast (28 to 1) there was still very little dependence on inclusion shape for effective permittivity.

The relationship between overall inclusion structure and effective permittivity was also examined. Specifically, investigations were performed looking into how the arrangement of inclusions impacted the individual extracted effective permittivity components corresponding to each direction of electric field polarization. The Wiener bounds represent the maximum and minimum possible effective permittivity for a composite and result from an inclusion in the shape of a plate. The maximum and minimum possible effective permittivities correspond to capacitors connected in parallel or series respectively.



As a test, an inclusion in the shape of a plate at 11% volume fraction was examined in CST Microwave Studio. As expected, the extracted effective permittivities corresponded to the results predicted by the Wiener bounds.

The maximum effective permittivity at a given volume fraction resulted when the largest face of the inclusion plate was parallel to the electric field polarization of the TEM field. Conversely, the minimum effective permittivity resulted when the largest face of the inclusion plate was perpendicular to the direction of electric field polarization.

These results were then related to the cross-sectional areas of the inclusion shaped as a plate. The maximum possible effective permittivity resulted when the inclusion had the minimum possible cross-sectional area normal to the direction of the electric field polarization. Conversely, the minimum possible effective permittivity occurred when the inclusion had the maximum possible cross-sectional area normal to the direction of electric field polarization. Combining these results, there was an inverse relationship between cross-sectional area of the inclusion and effective permittivity of the mixture for an inclusion shaped as a plate.

This examination between cross-sectional area fraction and effective permittivity was then extended to include mixtures with hundreds of inclusions. These mixtures with hundreds of cube or irregularly-shaped inclusions had close groupings of inclusions on the bottom of the outer box, forming an overall structure similar to a plate. The effective permittivity was the smallest when the electric field was polarized along the axis from which the inclusion crystals had the highest cross-sectional area fraction. Conversely, the other axes had lower cross-sectional area fraction and higher effective permittivity. Thus, a strong inverse relationship was also found between cross-sectional area fraction and effective permittivity for many inclusions with this plate-like arrangement.

Chapter 4 also examined EM localization for two distinct arrangements of inclusions.

The first type of mixture had hundreds of irregularly-shaped inclusion crystals of various sizes. At a volume fraction of 32.5%, and with electric field polarized along the  $x$  direction, electric energy density was examined for forward and reverse propagation directions. The electric energy density localized with different peak magnitudes depending on the propagation direction of the EM signal. At specific inclusion edges and corners close to each other in the direction of electric field polarization, the magnitude of the energy density increased as the EM signal traveled through more inclusions.

The second type of composite had dozens of cube inclusion crystals of the same size, where the inclusions were separated into parallel planes and varying numbers of inclusions were placed randomly in each plane. An increasing number of inclusions were placed between the outer layers to gradually increase the number of inclusions in each layer. The highest energy density resulted on the edges of adjacent cubes close together after the EM signal traveled through the highest number of inclusions.

In addition to the energy density results, simulation probes enabled the electric fields to be measured throughout the simulation at various points. For the irregular crystal mixture, the electric field localized at crystal corners and edges to a greater amount when the EM signal previously traveled through more scatterers. For the cube crystal mixture, electric fields were measured for the isolated cubes and the back cubes surrounded by many other inclusions (for opposite propagation directions, resulting in four different electric field probe results). The lowest electric field localization magnitude among these four cases occurred for the isolated cubes when these cubes were the first encountered by the EM pulse. The highest localization magnitude occurred for the back cubes where there were the most scatterers within that layer and the signal had traveled through the highest number of scatterers to reach that back point. Overall, higher peak electric field localization magnitude was reached after the EM pulse traveled through a greater

number of inclusions for both irregularly-shaped inclusions in a disordered arrangement and more organized cube crystals.

An important conclusion here is that the study of EM localization does not require geometrically complex structures, such as those created with the irregular inclusion mixtures in Chapter 4. Simpler arrangements of regularly shaped inclusions exhibit similar EM hotspot behavior, but with a significant decrease in mixture complexity.

## 5.2 Future Work

This dissertation examined various types of composite mixtures containing crystals of differing shapes and sizes. One area that can be expanded upon in future research is an increase in the irregularity of the crystals that are examined. For example, the deviation in crystal shapes from one crystal to the next could be increased.

Complex mixtures with many irregular crystals were created with volume fractions up to 42%. Future research could attempt to increase the maximum volume fractions simulated, possibly through new procedures for creating crystalline mixtures.

The research in this dissertation showed similar EM localization behavior for complex combinations of irregular crystals and more organized cube inclusions, with hotspots occurring on inclusion edges and corners. With the knowledge that studies of hotspots can be performed with relatively simple arrangements of inclusions, moving forward further simplifications could be made.

One idea is to take the concept of using EM simulation software to examine combinations of crystals within a surrounding material, as explored in this dissertation, and make an abstraction to a study of transmission lines. A lossless transmission line has series inductance,  $L$ , represented by an inductor, and shunt capacitance,  $C$ , represented by

a capacitor. LC tanks could be utilized to represent inclusion crystals. Inclusion corners could be represented by LCs with characteristic impedance representative of a crystal, and LCs connected together with this impedance could represent a complete crystal. These ‘crystals’ could be connected to each other by LCs with the characteristic impedance of vacuum, representing the binder material around the crystals. Randomness could be introduced here by changing the length of the transmission lines.

The transmission lines study can be expected to result in faster computation enabling such things as optimum EM waveform design. Gaussian input pulses were used in this dissertation in order to study a range of frequencies. The behavior of EM localization in composites can be further understood by examining different types of input waveforms, such as sinusoidal or rectangular inputs, and focusing on specific frequencies to search for an optimal waveform or frequency leading to high localization. The study of energetic materials in particular would be greatly aided with research showing increased hotspot magnitude due to a certain type of excitation signal.

## REFERENCES

- [1] F. C. De Lucia, R. S. Harmon, K. L. McNesby, R. J. Winkel, and A. W. Miziolek, “Laser-induced breakdown spectroscopy analysis of energetic materials,” *Appl. Opt.*, vol. 42, no. 30, pp. 6148–6152, Oct. 2003.
- [2] J. C. Carter, S. M. Angel, M. Lawrence-Snyder, J. Scaffidi, R. E. Whipple, and J. G. Reynolds, “Standoff detection of high explosive materials at 50 meters in ambient light conditions using a small Raman instrument,” *Appl. Spectrosc.*, vol. 59, no. 6, pp. 769–775, 2005.
- [3] D. S. Moore, “Recent advances in trace explosives detection instrumentation,” *Sens. Imag.: Int. J.*, vol. 8, no. 1, pp. 9–38, 2007.
- [4] A. Pettersson, I. Johansson, S. Wallin, M. Nordberg, and H. Östmark, “Near real-time standoff detection of explosives in a realistic outdoor environment at 55 m distance,” *Propellants Explos. Pyrotech.*, vol. 34, no. 4, pp. 297–306, Aug. 2009.
- [5] A. K. Misra, S. K. Sharma, T. E. Acosta, J. N. Porter, P. G. Lucey, and D. E. Bates, “Portable standoff Raman system for fast detection of homemade explosives through glass, plastic and water,” *Proc. of SPIE*, vol. 8358, pp. 835811-1–835811-10, 2012.
- [6] J. Pike, (2013). *Explosives* [Online]. Available: <http://www.globalsecurity.org/military/systems/munitions/explosives.htm>
- [7] J. Pike, (2013). *Explosives - Nitramines* [Online]. Available: <http://www.globalsecurity.org/military/systems/munitions/explosives-nitramines.htm>
- [8] G. Zorpette, “Countering IEDs”, *IEEE Spectrum*, vol. 45, no. 9, pp. 26–35, Sept. 2008.
- [9] P. Chen, F. Huang, and Y. Ding, “Microstructure, deformation and failure of polymer bonded explosives,” *J. Materials Science*, vol. 42, no. 13, pp. 5272–5280, Jan. 2007.
- [10] CST Microwave Studio. [Online]. Available: <http://www.cst.com/Content/Products/MWS/Overview.aspx>
- [11] E. Coumans, (2013). *Bullet physics library* [Online]. Available: <http://bulletphysics.org/wordpress/>
- [12] “Electric field,” *Wikipedia: The Free Encyclopedia*, May 2013.

- [13] “Dielectric,” *Wikipedia: The Free Encyclopedia*, May 2013.
- [14] “Relative permittivity,” *Wikipedia: The Free Encyclopedia*, May 2013.
- [15] “Permittivity,” *Wikipedia: The Free Encyclopedia*, June 2013.
- [16] “Loss tangent,” *Wikipedia: The Free Encyclopedia*, June 2013.
- [17] C. Brosseau, “Modelling and simulation of dielectric heterostructures: a physical survey from an historical perspective,” *Journal of Physics D: Applied Physics*, vol. 39, no. 7, pp. 1277–1294, 2006.
- [18] J. C. Maxwell, *A Treatise on Electricity and Magnetism*. Oxford: Clarendon, 1881.
- [19] J. H. Gladstone and T. P. Dale, “Researches on the refraction, dispersion, and sensitiveness of liquids,” *Philosophical Transactions of the Royal Society of London*, vol. 153, pp. 317–343, 1863.
- [20] A. Priou, Ed., *Progress in Electromagnetic Research: Dielectric Properties of Heterogeneous Materials*. New York, NY: Elsevier, 1992.
- [21] J. C. Maxwell Garnett, “Colours in metal glasses and in metallic films,” *Phil. Trans. R. Soc. Lond. A*, vol. 203, no. 359–371, pp. 385–420, 1904.
- [22] D. A. G. Bruggeman, “The calculation of various physical constants of heterogeneous substances. I. The dielectric constants and conductivities of mixtures composed of isotropic substances,” *Ann. Phys.*, vol. 24, no. 132, pp. 636–679, 1935.
- [23] O. Wiener, “Die theorie des mischkörpers für das feld der stationären strömung,” *Abh. Sächs. Ges. Akad. Wiss., Math.-Phys. Kl.*, vol. 32, no. 6, pp. 509–604, 1912.
- [24] R. Tao, Z. Chen, and P. Sheng, “First-principles Fourier approach for the calculation of the effective dielectric constant of periodic composites,” *Physical Review B*, vol. 41, no. 4, pp. 2417–2420, 1990.
- [25] C. Zhang, B. Yang, X. Wu, T. Lu, Y. Zheng, and W. Su, “Calculation of the effective dielectric function of composites with periodic geometry,” *Physica B*, vol. 293, no. 1–2, pp. 16–32, 2000.
- [26] O. Pekonen, K. K. Kärkkäinen, A. H. Sihvola, and K. I. Nikoskinen, “Numerical testing of dielectric mixing rules by FDTD method,” *Journal of Electromagnetic Waves and Applications*, vol. 13, no. 1, pp. 67–87, 1999.
- [27] A. Taflov and M. E. Brodwin, “Numerical solution of steady-state electromagnetic scattering problems using the time-dependent Maxwell’s equations,” *IEEE Transactions on Microwave Theory and Techniques*, vol. 23, no. 8, pp. 623–630, 1975.

- [28] K. L. Shlager and J. B. Schneider, "A selective survey of the Finite-Difference Time-Domain literature," *IEEE Antennas and Propagation Magazine*, vol. 37, no. 4, pp. 39–56, 1995.
- [29] G. Mur and A. de Hoop, "A finite-element method for computing three-dimensional electromagnetic fields in inhomogeneous media," *IEEE Transactions on Magnetics*, vol. 21, no. 6, pp. 2188–2191, 1985.
- [30] V. Myroshnychenko and C. Brosseau, "Finite-element method for calculation of the effective permittivity of random inhomogeneous media," *Physical Review E*, vol. 71, no. 1, pp. 016701-1–016701-16, 2005.
- [31] E. Tuncer, S. M. Gubański, and B. Nettelblad, "Dielectric relaxation in dielectric mixtures: Application of the finite element method and its comparison with dielectric mixture formulas," *J. Applied Physics*, vol. 89, no. 12, pp. 8092–8100, 2001.
- [32] C. Barnes and J. B. Pendry, "Multiple scattering of waves in random media: A transfer matrix approach," *Proceedings of the Royal Society of London. Series A: Mathematical and Physical Sciences*, vol. 435, no. 1893, pp. 185–196, 1991.
- [33] A. Beroual, C. Brosseau, and A. Boudida, "Permittivity of lossy heterostructures: Effect of shape anisotropy," *Journal of Physics D: Applied Physics*, vol. 33, no. 16, pp. 1969–1974, 2000.
- [34] C. Brosseau, A. Beroual, and A. Boudida, "How do shape anisotropy and spatial orientation of the constituents affect the permittivity of dielectric heterostructures?," *J. Applied Physics*, vol. 88, no. 12, pp. 7278–7288, 2000.
- [35] P. K. Ghosh and M. E. Azimi, "Numerical calculation of effective permittivity of lossless dielectric mixtures using boundary integral method," *IEEE Transactions on Dielectrics and Electrical Insulation*, vol. 1, no. 6, pp. 975–981, 1994.
- [36] K. K. Kärkkäinen, A. H. Sihvola, and K. I. Nikoskinen, "Effective permittivity of mixtures: Numerical validation by the FDTD method," *IEEE Trans. Geoscience Remote Sensing*, vol. 38, no. 3, pp. 1303–1308, May 2000.
- [37] K. K. Kärkkäinen, A. H. Sihvola, and K. I. Nikoskinen, "Analysis of a three-dimensional dielectric mixture with finite difference method," *IEEE Trans. Geoscience Remote Sensing*, vol. 39, no. 5, pp. 1013–1018, May 2001.
- [38] D. Wu, J. Chen, and C. Liu, "Numerical evaluation of effective dielectric properties of three-dimensional composite materials with arbitrary inclusions using a finite-difference time-domain method," *J. Applied Physics*, vol. 102, pp. 024107-1–024107-8, July 2007.

- [39] D. Wu, R. Qiang, J. Chen, C. Liu, M. Koledintseva, J. Drewniak, and B. Archambeault, "Numerical modeling of periodic composite media for electromagnetic shielding application," *2007 IEEE Int. Symp. on Electromagnetic Compatibility (EMC 2007)*, July 9–13, 2007, pp. 1–5.
- [40] M. Luo, C. Liu, and H. P. Pan, "Numerical simulation on dielectric enhancement of periodic composite media using a 3D finite difference method," *European Phys. J. Applied Physics*, vol. 52, pp. 20501-p1–20501-p8, Sept. 2010.
- [41] H. Wu, D. Wu, J. Chen, and R. Liu, "Evaluation of electrical properties for complex mixtures with a low-frequency periodic technique," *2008 IEEE MTT-S Int. Microwave Symp. Digest*, June 15–20, 2008, pp. 1349–1352.
- [42] Y. Cheng, X. Chen, K. Wu, S. Wu, Y. Chen, and Y. Meng, "Modeling and simulation for effective permittivity of two-phase disordered composites," *J. Applied Physics*, vol. 103, pp. 034111-1–034111-8, Feb. 2008.
- [43] X. Chen, Y. Cheng, K. Wu, and S. Wu, "Interfacial polarization and its influence on effective complex permittivity of mixtures," *2008 Int. Symp. on Electrical Insulating Materials (ISEIM 2008)*, Sept. 7–11, 2008, pp. 238–241.
- [44] L. Jylhä and A. H. Sihvola, "Numerical modeling of disordered mixture using pseudorandom simulations," *IEEE Trans. Geoscience Remote Sensing*, vol. 43, no. 1, pp. 59–64, Jan. 2005.
- [45] A. Mejdoubi and C. Brosseau, "Finite-difference time-domain simulation of heterostructures with inclusion of arbitrarily complex geometry," *J. Applied Physics*, vol. 99, pp. 063502-1–063502-14, March 2006.
- [46] A. Mejdoubi and C. Brosseau, "Duality and similarity properties of the effective permittivity of two-dimensional heterogeneous medium with inclusion of fractal geometry," *Physical Review E*, vol. 73, no. 3, pp. 031405-1–031405-8, March 2006.
- [47] A. Mejdoubi and C. Brosseau, "Dielectric response of perforated two-dimensional lossy heterostructures: A finite-element approach," *J. Applied Physics*, vol. 100, pp. 094103-1–094103-14, Nov. 2006.
- [48] G. J. Mazzaro, M. B. Steer, K. G. Gard, and A. L. Walker, "Response of RF networks to transient waveforms: Interference in frequency-hopped communications," *IEEE Trans. Microw. Theory Tech.*, vol. 56, no. 12, pp. 2808–2814, Dec. 2008.
- [49] A. M. Nicolson and G. F. Ross, "Measurement of the intrinsic properties of materials by time-domain techniques," *IEEE Trans. Instrum. Meas.*, vol. IM-19, no. 4, pp. 377–382, Nov. 1970.



- [50] W. B. Weir, "Automatic measurement of complex dielectric constant and permeability at microwave frequencies," *Proc. IEEE*, vol. 62, no. 1, pp. 33–36, Jan. 1974.
- [51] D. R. Smith, S. Schultz, P. Markoš, and C. M. Soukoulis, "Determination of effective permittivity and permeability of metamaterials from reflection and transmission coefficients," *Phys. Rev. B.*, vol. 65, no. 19, pp. 195104-1–195104-5, Apr. 2002.
- [52] N. C. Dyck, R. C. Denomme, and P. M. Nieva, "Effective medium properties of arbitrary nanoparticle shapes in a localized surface plasmon resonance sensing layer," *J. Phys. Chem. C*, vol. 115, no. 31, pp. 15225–15233, June 2011.
- [53] B. B. Glover and W. L. Perry, "Observation of localized charge transport in isolated microscopic mats of single-wall carbon nanotubes," *J. Applied Physics*, vol. 101, pp. 064309-1–064309-4, March 2007.
- [54] W. L. Perry, J. A. Gunderson, B. B. Glover, and D. M. Dattelbaum, "Electromagnetically induced localized ignition in secondary high explosives: Experiments and numerical verification," *J. Applied Physics*, vol. 110, pp. 034902-1–034902-8, 2011.
- [55] M. B. Steer, *Microwave and RF Design: A Systems Approach*. Raleigh, NC: SciTech Publishing, Inc., 2010, pp. 842–843.
- [56] A. J. Pickles and M. B. Steer, "Effective permittivity of 3-D periodic composites with regular and irregular inclusions," *IEEE Access*, vol. 1, pp. 523–536, 2013.
- [57] A. H. Sihvola, *Electromagnetic Mixing Formulas and Applications*. London, United Kingdom: The Institution of Electrical Engineers, 1999, ch. 9, pp. 161–163.
- [58] W. Cai and V. Shalaev, *Optical Metamaterials: Fundamentals and Applications*. New York, NY: Springer, 2010, ch. 4, pp. 60–64.
- [59] C. Yu, C. Loureiro, J. J. Cheng, L. G. Jones, Y. Y. Wang, Y. P. Chia, and E. Faillace, (2013). *Total Porosity* [Online]. Available: <http://web.ead.anl.gov/resrad/datacoll/porosity.htm>
- [60] A. J. Pickles, I. M. Kilgore, and M. B. Steer, "Automated creation of complex three-dimensional composite mixtures for use in electromagnetic simulation," *IEEE Access*, vol. 1, pp. 248–251, 2013.

## APPENDIX

# Appendix A

## MATLAB Code

### A.1 Code to Calculate Effective Permittivity

This section contains an example of the MATLAB code used to import the simulated *S*-parameters from CST Microwave Studio and then calculate effective permittivity. This code is used for the data in Figure 3.9.

```
clear all;

load HMXTwentyEyR1.txt
load HMXTwentyEyT1.txt

S11_y_20 = HMXTwentyEyR1;
S21_y_20 = HMXTwentyEyT1;
r_y_20 = zeros(1001,1);
t_y_20 = zeros(1001,1);
n_y_20 = zeros(1001,1);
z_y_20 = zeros(1001,1);
```

```

for i = 1:1001
    r_y_20(i) = S11_y_20(i,2).*exp(1j*S11_y_20(i,3)*(pi/180));
end

for i = 1:1001
    t_y_20(i) = S21_y_20(i,2).*exp(1j*S21_y_20(i,3)*(pi/180));
end

for i = 1:1001
    f_y_20(i) = S21_y_20(i,1);
end

load HMXTwentyEyR2Fixed.txt
load HMXTwentyEyT2Fixed.txt

S11_y2_20 = HMXTwentyEyR2Fixed;
S21_y2_20 = HMXTwentyEyT2Fixed;
r_y2_20 = zeros(1001,1);
t_y2_20 = zeros(1001,1);
n_y2_20 = zeros(1001,1);
z_y2_20 = zeros(1001,1);

for i = 1:1001
    r_y2_20(i) = S11_y2_20(i,2).*exp(1j*S11_y2_20(i,3)*(pi/180));

```

```

end

for i = 1:1001
    t_y2_20(i) = S21_y2_20(i,2).*exp(1j*S21_y2_20(i,3)*(pi/180));
end

for i = 1:1001
    f_y2_20(i) = S21_y2_20(i,1);
end

load HMXTwentyExR1Fixed.txt
load HMXTwentyExt1Fixed.txt

S11_x_20 = HMXTwentyExR1Fixed;
S21_x_20 = HMXTwentyExt1Fixed;
r_x_20 = zeros(1001,1);
t_x_20 = zeros(1001,1);
n_x_20 = zeros(1001,1);
z_x_20 = zeros(1001,1);

for i = 1:1001
    r_x_20(i) = S11_x_20(i,2).*exp(1j*S11_x_20(i,3)*(pi/180));
end

for i = 1:1001

```

```

        t_x_20(i) = S21_x_20(i,2).*exp(1j*S21_x_20(i,3)*(pi/180));
    end

    for i = 1:1001
        f_x_20(i) = S21_x_20(i,1);
    end

    load HMXTwentyExR2Fixed.txt
    load HMXTwentyExT2Fixed.txt

    S11_x2_20 = HMXTwentyExR2Fixed;
    S21_x2_20 = HMXTwentyExT2Fixed;
    r_x2_20 = zeros(1001,1);
    t_x2_20 = zeros(1001,1);
    n_x2_20 = zeros(1001,1);
    z_x2_20 = zeros(1001,1);

    for i = 1:1001
        r_x2_20(i) = S11_x2_20(i,2).*exp(1j*S11_x2_20(i,3)*(pi/180));
    end

    for i = 1:1001
        t_x2_20(i) = S21_x2_20(i,2).*exp(1j*S21_x2_20(i,3)*(pi/180));
    end
end

```

```

for i = 1:1001
    f_x2_20(i) = S21_x2_20(i,1);
end

load HMXTwentyEzR1Fixed.txt
load HMXTwentyEzT1Fixed.txt

S11_z_20 = HMXTwentyEzR1Fixed;
S21_z_20 = HMXTwentyEzT1Fixed;
r_z_20 = zeros(1001,1);
t_z_20 = zeros(1001,1);
n_z_20 = zeros(1001,1);
z_z_20 = zeros(1001,1);

for i = 1:1001
    r_z_20(i) = S11_z_20(i,2).*exp(1j*S11_z_20(i,3)*(pi/180));
end

for i = 1:1001
    t_z_20(i) = S21_z_20(i,2).*exp(1j*S21_z_20(i,3)*(pi/180));
end

for i = 1:1001
    f_z_20(i) = S21_z_20(i,1);

```

```

end

load HMXTwentyEzR2Fixed.txt
load HMXTwentyEzT2Fixed.txt

S11_z2_20 = HMXTwentyEzR2Fixed;
S21_z2_20 = HMXTwentyEzT2Fixed;
r_z2_20 = zeros(1001,1);
t_z2_20 = zeros(1001,1);
n_z2_20 = zeros(1001,1);
z_z2_20 = zeros(1001,1);

for i = 1:1001
    r_z2_20(i) = S11_z2_20(i,2).*exp(1j*S11_z2_20(i,3)*(pi/180));
end

for i = 1:1001
    t_z2_20(i) = S21_z2_20(i,2).*exp(1j*S21_z2_20(i,3)*(pi/180));
end

for i = 1:1001
    f_z2_20(i) = S21_z2_20(i,1);
end

c=299.8;

```



```

d_Ex_20 = 0.260;
d_Ey_20 = 0.260;
d_Ez_20 = 0.260;

for i = 1:1001
    n_y_20(i) = (acos((1/(2*t_y_20(i)))*(1-((r_y_20(i)).^2 -
        (t_y_20(i)).^2)))+(2*pi*(0)))/((2*pi*f_y_20(i)*d_Ey_20)./c);
    z_y_20(i) = sqrt(((1+(r_y_20(i))).^2 -
        (t_y_20(i)).^2)./(1-(r_y_20(i)).^2 - (t_y_20(i)).^2));
end

for i = 1:1001
    n_y2_20(i) = (acos((1/(2*t_y2_20(i)))*(1-((r_y2_20(i)).^2 -
        (t_y2_20(i)).^2)))+(2*pi*(0)))/((2*pi*f_y2_20(i)*d_Ey_20)./c);
    z_y2_20(i) = sqrt(((1+(r_y2_20(i))).^2 -
        (t_y2_20(i)).^2)./(1-(r_y2_20(i)).^2 - (t_y2_20(i)).^2));
end

for i = 1:1001
    n_x_20(i) = (acos((1/(2*t_x_20(i)))*(1-((r_x_20(i)).^2 -
        (t_x_20(i)).^2)))+(2*pi*(0)))/((2*pi*f_x_20(i)*d_Ex_20)./c);
    z_x_20(i) = sqrt(((1+(r_x_20(i))).^2 -
        (t_x_20(i)).^2)./(1-(r_x_20(i)).^2 - (t_x_20(i)).^2));
end

```

```

for i = 1:1001
    n_x2_20(i) = (acos((1/(2*t_x2_20(i)))*(1-((r_x2_20(i)).^2 -
        (t_x2_20(i)).^2)))+(2*pi*(0)))/((2*pi*f_x2_20(i)*d_Ex_20)./c);
    z_x2_20(i) = sqrt(((1+(r_x2_20(i))).^2 -
        (t_x2_20(i)).^2)/((1-(r_x2_20(i))).^2 - (t_x2_20(i)).^2));
end

for i = 1:1001
    n_z_20(i) = (acos((1/(2*t_z_20(i)))*(1-((r_z_20(i)).^2 -
        (t_z_20(i)).^2)))+(2*pi*(0)))/((2*pi*f_z_20(i)*d_Ez_20)./c);
    z_z_20(i) = sqrt(((1+(r_z_20(i))).^2 -
        (t_z_20(i)).^2)/((1-(r_z_20(i))).^2 - (t_z_20(i)).^2));
end

for i = 1:1001
    n_z2_20(i) = (acos((1/(2*t_z2_20(i)))*(1-((r_z2_20(i)).^2 -
        (t_z2_20(i)).^2)))+(2*pi*(0)))/((2*pi*f_z2_20(i)*d_Ez_20)./c);
    z_z2_20(i) = sqrt(((1+(r_z2_20(i))).^2 -
        (t_z2_20(i)).^2)/((1-(r_z2_20(i))).^2 - (t_z2_20(i)).^2));
end

%Plot effective permittivity using only positive propagation directions
plot(f_z_20,(1/3)*(real(n_y_20./z_y_20)+real(n_x2_20./z_x2_20)
+real(n_z_20./z_z_20)),'b');

```

```

axis([0.1 50 0 3]);
xlabel('f (GHz)');
ylabel('Effective relative permittivity');
title('Real effective relative part of epsilon, Filling factor = 20%,
No rotation, Positive Excited Directions');
grid on

%Plot real part of effective permittivity using all 6 (positive and
negative) propagation directions
figure(2)
plot(f_z_20,(1/6)*(real(n_y_20./z_y_20)+real(n_y2_20./z_y2_20)+
real(n_x_20./z_x_20)+real(n_x2_20./z_x2_20)+real(n_z_20./z_z_20)
+real(n_z2_20./z_z2_20)),'b');
axis([0.1 50 0 3]);
grid on
xlabel('f (GHz)');
ylabel('Real effective Relative Permittivity');
title('Real effective relative part of epsilon, Filling Factor = 20%,
No rotation, 6 Excited Directions');

```

## A.2 Code to Plot Effective Permittivity and Mixing Theories

This example MATLAB code is used to plot the results of effective permittivity versus the Maxwell Garnett and Bruggeman mixing theories as seen in Figure 3.10.

```
clear all;

f =0:0.001:0.6;
e1 = 28-1j*0.0252;
e2 = 1-1j*0;
e_eff =(e2 +(3.*f.*e2.*(e1-e2))./(e1+2.*e2-f.*(e1-e2)));

plot(f,real(e_eff),'-k');
xlabel('Volume fraction')
ylabel('Real effective relative permittivity')
grid on
hold on

a = 2;
b = (e1-3.*e1.*f-2.*e2+3.*e2.*f)
c = (-e2.*e1);
e_eff2 = (-b + sqrt(b.^2 - 4.*a.*c))./(2.*a);
plot(f,real(e_eff2),'--k')
hold on

x_zirconia_pos = [0.1 0.2 0.25 0.3 0.35 0.4 0.45];
```

```

y_zirconia_pos = [1.355 1.801 2.06 2.377 2.731 3.193 3.807];
x_zirconia_all_six = [0.1 0.2 0.25 0.3 0.35 0.4 0.45];
y_zirconia_all_six = [1.356 1.801 2.059 2.379 2.73 3.193 3.805];

plot(x_zirconia_pos,y_zirconia_pos,'sk');
axis([0 0.47 0 12]);
hold on
plot(x_zirconia_all_six,y_zirconia_all_six,'+k');
legend('Maxwell Garnett','Bruggeman','Finite Integration Technique (FIT),
positive propagation directions','Finite Integration Technique (FIT),
six propagation directions');

```